Ground-Based Remote Sensing of Land Surfaces – The Influence of Periodic Patterns and Relief on Thermal Microwave Emission

Inauguraldissertation
der Philosophisch-naturwissenschaftlichen Fakultät
der Universität Bern

vorgelegt von

Ingo Völksch

von Jena, Deutschland

Leiter der Arbeit:

Prof. Dr. Christian Mätzler

Institut für Angewandte Physik

Outline

In this thesis, we investigate the microwave emission at 1.4 GHz of bare soil surfaces in the presence of dielectric anisotropy and (periodic) relief patterns by means of experimental and model studies. The main part of the thesis consists of two published articles and one very detailed research report, which is, in a condensed form, intended for publication in the near future. The thesis is structured as follows:

In Chapter I, we give the context and the motivation of this thesis. First, we show the importance of monitoring the spatio-temporal evolution of soil moisture on the large scale, and explain why remote sensing using passive microwave radiometry is one of the most promising measuring techniques thereof. Then, a brief review of the processing chain involved in the retrieval of soil moisture from microwave radiometer measurements is given. Thus, we demonstrate the need for an improved understanding of the emission behavior of land surfaces with distinct relief patterns and locally varying emission properties for reliable soil-moisture retrievals over such areas. Finally, we present the ETH L-BAnd RAdiometer (ELBARA) used in this study. A brief description of the instrument design is given, followed by an overview of previous passive microwave experiments carried out with ELBARA.

In Chapter II, we present an experiment to investigate the influence of pronounced dielectric anisotropy on thermal emission at 1.4 GHz using an artificial setup consisting of a wire grid placed above the ground. Experimentally-derived reflectivities of the corresponding footprint are discussed for different grid orientations and wire spacings, and a physical reflectivity model is used to analyze the experimental results.

In Chapter III, the focus is on thermal L-band signatures of soils with periodic relief patterns (furrows) with dimensions close to the observation wavelength. We experimentally investigate the impact of such furrows on soil reflectivity for different furrow orientations under dry-soil and moist-soil conditions. Furthermore, a physical reflectivity model for dielectric periodic surfaces is presented, and used to explain the topography-related features of the signatures measured.

In Chapter IV, we use a time series of brightness-temperature measurements of a renaturated soil surface, to investigate the impact of naturally-formed erosion gullies on L-band emission. Additionally, an emission model, taking into account both the surface relief and the locally varying permittivity of the soil, is developed, and applied to simulate corresponding brightness-temperature time series. We present a detailed analysis of the measurements and the

simulation results focusing on the relief effects on L-band emission, on the one hand, and on the brightness-temperature changes observed during typical weather conditions, on the other. By comparing the brightness temperatures measured and simulated, we furthermore try to distinguish the relief effects from effects, which are caused by different hydrological properties of areas inside and outside the erosion gullies.

Chapter V concludes this thesis.

Contents

Chapter I

Introduction

1 Background and Motivation

The global water cycle is one of the fundamental life-sustaining processes on our planet, and a better understanding of this highly complex system and particularly of the potential consequences of climate change on Earth's water cycle is one of the highest priorities in Earth Science and environmental policy issues today. One of the key variables in this continuous exchange of water between the oceans, the atmosphere and the land (Fig. 1) is soil moisture. Near-surface soil moisture strongly controls the partitioning of precipitation into surface run-off, evapotranspiration, and infiltration, while soil moisture in the vadose zone governs the rate of water uptake by vegetation as well as its water-storage capacity. Thus, soil moisture determines the humidity of the atmosphere as well as the fertility of the land, and furthermore influences groundwater dis- and recharge. Therefore, monitoring the spatial distribution and the dynamics of soil moisture is essential for a better understanding of the water cycle on Earth and its relationship to climate change. The spatio-temporal evolution of soil-moisture fields is furthermore an important input for numerical weather and climate models, and should be accounted for in hydrology and vegetation monitoring [1], [2].
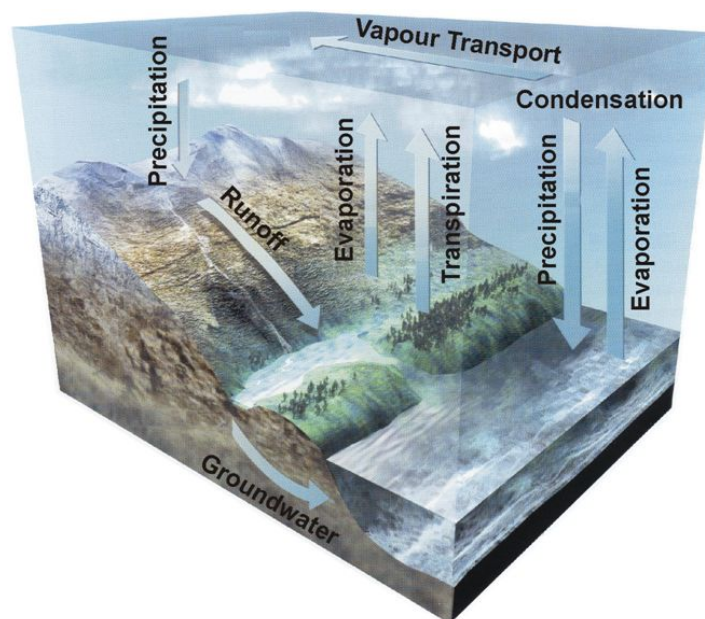
Fig. 1. The global water cycle (picture taken from [3]).

However, it is quite difficult to measure soil moisture regularly on large areal scales. Today, soil sampling, time-domain reflectometry (TDR), as well as neutron and capacitance probes are commonly used for *in situ* measurements of the water content of a soil. These methods are often tedious and time-consuming, and additionally disturb the soil structure, thus not allowing for repeated measurements at the same point [4]. Furthermore, such point measurements are usually restricted to and representative for only small observation areas, and are hard to interpolate to regional or even global scales, which are relevant for climate prediction models.

Remote sensing techniques using either passive microwave radiometry or active radar systems offer a possible solution to these problems [5]–[8]. They are non-invasive, repeatable, and deliver large scale information, if operated from airplanes or satellites. Today, the use of L-band microwave radiometer systems sensitive at 1.4 GHz (observation wavelength $\lambda \approx 21$ cm) is one of the most promising approaches for remotely monitoring near-surface soil moisture on the large scale. Passive microwave radiometry at L band has the advantage of being unaffected by cloud cover and solar radiation allowing for all-weather continuous (day and night) measurements. The sensitive 1400–1427 MHz frequency band of most L-band radiometers is protected, which means that distortions due to anthropogenic radio frequency interferences (RFI) are minimized. Furthermore, the emission depth in soils is relatively large, and the vegetation canopy is semitransparent at 1.4 GHz. However, the spatial resolution of soil-moisture data retrieved from L-band measurements is rather coarse (e.g., ≈45 km for satellite measurements at an altitude of 760 km [9]), which is a direct consequence of diffraction occurring at the aperture of the receiving antenna. Other techniques, such as passive microwave measurements at higher frequencies or active microwave remote sensing (radar), provide better spatial resolution, but suffer strong deficiencies due to their vulnerability to cloud cover, their higher sensitivity to surface roughness and vegetation cover, and the lower emission/penetration depth [6], [10]. Therefore, they have inferior sensitivity to soil moisture compared to passive measurements at 1.4 GHz [1].

Understanding the need for reliable global soil moisture (and sea surface salinity) data at adequate spatial and temporal resolution to improve meteorological and climate predictions, and recognizing that space-borne L-band radiometry is the most promising measuring technique, the European Space Agency (ESA) selected the Soil Moisture and Ocean Salinity (SMOS) mission as its second Earth Explorer Opportunity mission. The SMOS satellite was successfully launched in November 2009, carrying onboard the Microwave Imaging Radiometer using Aperture Synthesis MIRAS operating in the protected 1400–1427 MHz band [11]. SMOS provides global coverage of brightness temperatures with an average spatial resolution of ≈45 km and a revisit time of less than three days, from which near-surface soil moisture and sea-surface salinity are subsequently retrieved [9]. Also the National Aeronautics and Space Administration (NASA) plans a satellite mission to globally measure soil moisture, and to furthermore distinguish frozen from thawed land surfaces based on L-band measurements. NASA's Soil Moisture Active Passive (SMAP) mission will use a measurement approach integrating an L-band radar and an L-band radiometer as a single observation

system, combining the relative strengths of active and passive remote sensing for enhanced soil moisture mapping. SMAP is scheduled for launch in the 2014–2015 time frame [12].

Passive microwave radiometry at 1.4 GHz is an indirect method to measure the water content wc of a soil using the complex permittivity (also called dielectric constant) $\varepsilon = \varepsilon' + i\varepsilon''$ as a proxy for wc. The determination of the soil permittivity ε is thereby based on the measurement of electromagnetic radiation, which is emitted by the observed soil surface in the narrow frequency band between 1400 and 1427 MHz. At these frequencies, the intensity of the observed radiation (thermal emission) is proportional to the thermodynamic temperature T and the emissivity E of the observed surface (Rayleigh-Jeans approximation of Planck's Law). This product is usually referred to as the brightness temperature T_B [13], which is the radiance that is actually observed by a microwave radiometer.

To derive the soil permittivity ε from the T_B measured, first an appropriate radiative-transfer model taking into account the different emission, reflection, absorption, and scattering processes at the soil surface and in the vegetation canopy has to be applied, which eventually yields the soil's emissivity E or reflectivity R, respectively. Generally, the brightness temperature observed by a radiometer is given by

$$T_B = \Gamma_{atm} \left(T_{B,surf} + R \cdot T_{sky} \right) + T_{atm} \tag{1}$$

where Γ_{atm} is the atmospheric transmission from the ground to the radiometer, $T_{B,surf}$ is the emission from the surface with reflectivity R, T_{sky} is the sky brightness, and T_{atm} is the upwelling atmospheric radiance. At 1.4 GHz, Γ_{atm} is typically very close to 100%, and T_{atm} is very small and can generally be neglected [13]. Thus, (1) reduces to

$$T_B = T_{B,surf} + R \cdot T_{sky} \tag{2}$$

describing T_B as the sum of the surface emission $T_{B,surf}$ and the reflected sky brightness $R \cdot T_{sky}$, with $T_{B,surf}$ as the main contributor to T_B. In the simple case of a homogenous, bare soil surface, $T_{B,surf}$ can be expressed as the product of its emissivity E and the soil's effective physical temperature T_{eff}. Assuming local thermodynamic equilibrium and applying Kirchhoff's Law, the emissivity can be expressed as $E = 1 - R$. This yields

$$T_B = (1 - R)T_{eff} + R \cdot T_{sky}. \tag{3}$$

The sky brightness $T_{sky} \approx 5$ to 6 K at L band is well known (e.g., [14] and [15]), and T_{eff} can be derived, e.g. from thermal infrared or *in situ* temperature measurements. Thus, the simple radiative-transfer model (3) can be used to calculate the reflectivity R of a homogeneous bare, soil surface. However, when the observed surface is covered by vegetation, (3) is usually no longer sufficient as also absorption, emission, and scattering by the vegetation canopy have to be considered in the formulation of the radiative-transfer model.

The reflectivity R of a soil is directly related to its permittivity ε. That means, ε can be derived from R by applying an appropriate reflectivity model. In the simplest case of a bare, homogenous, and smooth soil surface, R is a function of the observation angle, the polarization of the observed radiation, and the soil permittivity, and can be expressed with the Fresnel equations [16]. Under natural conditions, the prerequisites, which allow using the Fresnel relations, are hardly ever met, however. That means, in most cases more sophisticated reflectivity models taking into account, e.g. soil roughness and topography or dielectric anisotropy have to be applied to derive ε.

The complex permittivity $\varepsilon = \varepsilon' + i\varepsilon''$ of a soil is a material property, which is a measure for the soil's response to an applied electromagnetic field. The permittivities of the gaseous (air) and the solid (matrix) soil phase are $\varepsilon_a = 1$ and $\varepsilon_s \approx 3\text{-}5$, respectively, whereas the permittivity of water is $\varepsilon_w \approx 80$ at frequencies around 1.4 GHz. Due to this large contrast of ε_a, ε_s and ε_w, the effective permittivity ε of a moist soil is very sensitive to changes in the soil-water content wc, thus making ε an excellent proxy-quantity to determine wc. To convert ε into wc, dielectric mixing models are applied. To date, several different approaches are used ranging from purely empirical relations, such as [17], to physical models accounting also for soil texture, temperature, salinity, and fraction of bound and free water, such as [18].

The elaborations above show the complex processing chain involved in deriving soil moisture from brightness-temperature measurements, and illustrate that the quality of the soil-moisture retrievals depends largely on the performance of the radiative-transfer and reflectivity models applied to the signatures measured. With this in mind, many methodological studies have been carried out in the past over various types of terrestrial surfaces, investigating and demonstrating the influence of, e.g. different types of vegetation (e.g., [19]–[21]) or soil roughness (e.g., [22] and [23]) on the microwave emission of land surfaces. However, also pronounced dielectric anisotropy or (periodic) topographic features of a soil surface can affect the thermal microwave signatures. Examples of such surfaces are land areas with sparse or no vegetation undergoing erosion processes, which can produce gullies preferentially aligned with the slope. Also agricultural fields can feature periodic structures, in particular furrows originating from, e.g. plowing, sowing, or furrow irrigation.

Contributing toward the conceptual understanding of the L-band emission of such surfaces is the main motivation of this thesis. In particular, the influence of (periodic) topography on the emission of bare soils was investigated using a combined experimental and modeling approach. To this end, three tower-based passive microwave experiments were performed on different surfaces, displaying periodic dielectric and topographic patterns and ranging from highly synthetic toward natural. Dual-polarized brightness temperatures at 1.4 GHz of these surfaces were measured, and subsequently corresponding reflectivities were derived and analyzed. Appropriate reflectivity models able to account for the impact of dielectric anisotropy and (periodic) soil topography on L-band emission were implemented and to some extent developed. Experimental and model results were then compared with each other, to interpret and

explain the signatures measured. All measurements were carried out with the ETH L-band radiometer ELBARA, which is further described below.

2   The ETH L-Band Radiometer and its History

The **E**TH **L-BA**nd **RA**diometer for soil moisture research (ELBARA) was constructed in 2001 at the Institute of Applied Physics (IAP), University of Bern in collaboration with the Institute of Terrestrial Ecology, Swiss Federal Institute of Technology (ETH) Zürich [24] (Fig. 2). It is a Dicke-type radiometer equipped with a highly directive dual-mode Picket-horn antenna, measuring brightness temperatures T_{B}^{p} at horizontal ($p = \mathrm{H}$) and vertical ($p = \mathrm{V}$) polarization in the protected frequency range 1400–1427 MHz. Within the last ten years, ELBARA has been deployed for a multitude of passive microwave experiments at several field sites in three different European countries. In the course of these experiments, several modifications to the original instrument design were made. One of the major improvements thereby was the refitting of ELBARA with an automated elevation stage and a revolving platform, making it possible to automatically change the view direction of the antenna in elevation as well as in azimuth[1]. In some of the experiments outlined below, ELBARA was furthermore operated in combination with the X-band MOno RAdiometer MORA that was also constructed at IAP. MORA operates at 11.4 GHZ, which lies within the more common 6–100 GHz frequency range exclusively used for satellite-based microwave radiometry prior to the launch of SMOS.

Fig. 2. ELBARA and its designers (from left to right: Christian Mätzler, Jörg Leuenberger, Daniel Weber, Hannes Flühler, and Arthur Kölliker) at the presentation of ELBARA after its completion in April 2002.

---

[1] The design and technical characteristics of ELBARA will not be further discussed here. They are extensively described in [24], and are again summarized in the works cited below and in Chapters II to IV of this thesis.

ELBARA was first used in the PhD project of Katrin Schneeberger [25] at a field site in Eschikon (Switzerland), where it was set up on a small tower overlooking a bare soil surface in April 2002. This work aimed at retrieving soil-hydraulic properties from the dynamics of the water content in the top soil, which was determined, amongst others, by means of microwave radiometry. Although ELBARA was not specifically designed to be used for long-term deployment under rough field conditions, the instrument proved to be very stable, allowing for all-weather continuous (day and night) measurements of the T_B^p of a natural soil surface at high temporal resolution. However, when the soil-water content wc was retrieved from the T_B^p measured, significant discrepancies were observed compared to *in situ* measured wc, which was mainly attributed to the small-scale roughness of the surface [26]. Since none of the surface-reflectivity models existing at that time were capable to explain the observed discrepancies, a new roughness model was developed, which led to a considerable improvement of the results [27], and was one of the major outcomes of the PhD project. This newly-developed air-to-soil transition model is based on impedance matching occurring across the air-to-soil interface, and includes dielectric mixing effects due to small-scale surface structures of the soil [28].

From December 2002 to March 2003, a cold season experiment was conducted with ELBARA, demonstrating the sensitivity of L-band emission to soil frost, on the one hand, and showing the potential of estimating soil-frost penetration velocity from radiometrically measured L-band radiation, on the other [29]. Subsequently, ELBARA was moved to Wageningen (The Netherlands), where it was supplemented with an automatic rotation system and put on top of a 5 m scaffolding tower. With this setup, T_B^p of three different vegetated sites (bare soil, short grass, and growing grass) were measured quasi-simultaneously from April till September 2003, to investigate the effects of vegetation on microwave emission. Comparing radiometrically retrieved wc with *in situ* measurements illustrated the capability of ELBARA to accurately measure wc of the bare soil, but also showed that it is much more difficult to extract wc out of the microwave signal for vegetated sites. However, it was demonstrated that the effect of vegetation on microwave emission leads to other potential applications, such as monitoring the vegetation biomass and detecting canopy storage or the wetting of the vegetation caused by dew [20]. ELBARA was then transported back to Switzerland, and a first instrument maintenance was carried out at IAP in the spring of 2004. Besides, ELBARA was additionally equipped with an automated elevation stage, making it now possible to change the view direction of the antenna in elevation as well as in azimuth. To test the performance of the elevation tracker, ELBARA was once again installed at Eschikon in the summer of 2004. This testing phase was utilized for a measurement campaign on growing clover grass investigating the influence of vegetation on microwave emission in terms of its optical depth. This revealed a linear relation between vegetation water-mass equivalent and polarization-averaged optical depth. Furthermore, it was shown that the vegetation optical depth is polarization-dependent and highly affected by the canopy internal structure, thus demonstrating the need to use anisotropic dielectric mixing models, to represent the canopy within wc retrieval algorithms [30].

Fig. 3. ELBARA looking at the forest canopy from below (left), and the installation of ELBARA on the 100-m-high platform of the meteorological tower (right).

From October 2004 until May 2005, ELBARA was installed at a forested field site of the Forschungszentrum Jülich (Germany), where it was deployed within the framework of the PhD project of Massimo Guglielmetti to investigate the L-band radiation properties of a deciduous forest canopy [31] (Fig. 3). In a first experiment, the radiometer was installed in upward direction below the tree canopy measuring the downwelling T_{B}^p during the defoliation period of the forest [32]. For a second experiment, ELBARA was mounted on the 100-m-high platform of a meteorological tower located within the forest stand, and T_{B}^p was measured from above [21]. Simultaneously, thermal infrared temperature of the vegetation and air and soil temperatures were recorded. Based on these data, the transmissivity of the forest canopy at different foliation states was estimated. Transmissivities derived from the upward and the downward measurements were comparable and revealed the semi-transparency of the forest canopy at L-band frequencies. Due to the small difference of the transmissivities at the foliated and the defoliated state and the small polarization dependency of the transmissivity, it was concluded that the randomly distributed branches produce the main fraction of absorption for L-band radiation propagating through the forest canopy, whereas leaves and trunks contribute little to the overall canopy absorption. An irrigation experiment was carried out at the end of the measurement campaign in Jülich to explore the effect of soil moisture, which revealed a significant impact of the leaf litter covering the forest floor on ground emission.

This finding led to a follow-up experiment investigating the influence of a typical leaf-litter layer on L-band emission, which was again carried out at the field site in Eschikon after a thorough revision of the instrument at IAP in the summer of 2006. In this investigation, it was shown that the typical amount of dead leaves on the floor of a deciduous forest is almost transparent at L-band frequencies when dry, but acts as an important and not negligible radia-

tion source at moist states. A physically based radiative-transfer model was developed, which could reproduce the observations satisfactorily [33].

From the summer of 2006 until the end of 2009, ELBARA was then deployed in three more passive microwave experiments, which are presented in Chapters II to IV of this thesis. After the completion of these experiments, the life of ELBARA finally came to an end. It had now done its duty and was finally dismantled in the spring of 2010. However, based on the proven architecture of the ELBARA prototype, several similar L-band radiometers have been built within the last 10 years by IAP and Gamma Remote Sensing AG, Gümligen (Switzerland). They are currently deployed for further research on the remote sensing of soil moisture by means of passive microwave radiometry at the Forschungszentrum Jülich, and for calibration and validation activities associated with ESA's SMOS mission at three different locations in Europe [34].

3   Structure of this Thesis

This thesis describes the results of the third PhD project by now, which is based on passive microwave experiments carried out with ELBARA. It can be seen as the logical continuation of the methodological studies presented above. However, this work does not focus on the influence of small-scale surface roughness and vegetation on the microwave emission at 1.4 GHz, but deals with the influence of dielectric anisotropy and (periodic) soil topography instead.

The first two experiments performed within the framework of this project were carried out at the Swiss Federal Institute for Forest, Snow and Landscape Research (WSL) in Birmensdorf (Switzerland). ELBARA was mounted on a scaffolding tower and directed toward a paved area with the antenna aperture approximately 4 m above the ground and the observation angle $\theta = 50°$ relative to the vertical direction. In the first experiment performed in spring 2007 and described in Chapter II, a 4 m × 4 m wire grid strung with parallel conducting wires was placed in the footprint of ELBARA. Reflectivities were derived from dual-polarized brightness temperature measurements at different grid orientations and wire spacings. With this setup we investigated the impact of pronounced dielectric anisotropy on thermal brightness at 1.4 GHz.

The second experiment, which is described in Chapter III, aimed at investigating the effect of periodic soil topography (e.g., irrigation or plowing furrows in agricultural fields) on L-band signatures. For this purpose, we replaced the wire grid with a 3 m × 4 m soil box filled with sandy soil. Periodic furrows with dimensions close to the observation wavelength of 21 cm were then imprinted into the soil surface, and dual-polarized brightness temperatures were measured for different furrow orientations and soil-water contents in January 2008. Corresponding experimentally-derived reflectivities were analyzed and a physical reflectivity model for periodic dielectric surfaces was used to explain the topography-related aspects of the signatures measured.

To further investigate topography effects on L-band emission, we carried out a third experiment in Northeastern Germany (Chapter IV). In the summer of 2008, ELBARA was installed in the research catchment "Hühnerwasser", which is a recently renaturated former lignite-mining area close to the city of Cottbus. ELBARA was mounted on a scaffolding tower with the antenna aperture approximately 10 m above the ground and the observation angle $\theta = 55°$ relative to the vertical direction. From September 2008 until the end of 2009, dual-polarized brightness temperatures of two adjacent footprints at different development stages were measured quasi-simultaneously. The first footprint was crossed by several distinct erosion gullies, whereas the surface of the second footprint was still plane. A complex facet model based on geometric optics was developed, to also simulate brightness temperatures of the two scenes. The simulated and measured brightness temperatures were analyzed and compared with each other, as well as between the two areas, to investigate the impact of relief on L-band emission and to analyze how these relief effects vary with time as a result of changing ambient conditions.

The thesis concludes with a comprehensive summary, which is given in Chapter V.

References

[1] Y. H. Kerr, P. Waldteufel, J.-P. Wigneron, J.-M. Martinuzzi, J. Font, and M. Berger, "Soil moisture retrieval from space: The Soil Moisture and Ocean Salinity (SMOS) mission," *IEEE Trans. Geosci. Remote Sens.*, vol. 39, no. 8, pp. 1729-1735, 2001.

[2] ESA. (1 Jan. 2011). SMOS Mission. [Online]. Available: http://multimedia.esa.int/Videos/2009/07/SMOS-Mission2

[3] M. R. Drinkwater, Y. H. Kerr, J. Font, and M. Berger, "The Soil Moisture and Ocean Salinity mission. Exploring the water cycle of the 'blue planet'," *ESA Bull.*, vol. 137, 2009.

[4] F. Jonard, L. Weihermüller, K. Z. Jadoon, M. Schwank, H. Vereecken, and S. Lambot, "Mapping field-scale soil moisture with L-band radiometer and ground-penetrating radar over bare soil," *IEEE Trans. Geosci. Remote Sens.*, in press.

[5] F. T. Ulaby, R. K. Moore, and A. K. Fung, *MICROWAVE REMOTE SENSING: Active and Passive*, vol. III. Reading, Massachusetts: Addison-Wesley Publishing Company, 1981.

[6] T. J. Jackson, J. Schmugge, and E. T. Engman, "Remote sensing applications to hydrology: Soil moisture," *Hydrol. Sci. J.*, vol. 41, no. 4, pp. 517-530, 1996.

[7] J. A. Huisman, S. S. Hubbard, J. D. Redman, and A. P. Annan, "Measuring soil water content with ground penetrating radar: A review," *Vadose Zone J.*, vol. 2, no. 4, pp. 476-491, 2003.

[8] W. Wagner, G. Bloschl, P. Pampaloni, J. C. Calvet, B. Bizzarri, J. P. Wigneron, and Y. Kerr, "Operational readiness of microwave remote sensing of soil moisture for hydrologic applications," *Nord. Hydrol.*, vol. 38, no. 1, pp. 1-20, 2007.

[9] Y. H. Kerr, P. Waldteufel, J. P. Wigneron, S. Delwart, F. Cabot, J. Boutin, M. J. Escorihuela, J. Font, N. Reul, C. Gruhier, S. E. Juglea, M. R. Drinkwater, A. Hahne, M. Martin-Neira, and S. Mecklenburg, "The SMOS mission: New tool for monitoring key elements of the global water cycle," *Proc. IEEE*, vol. 98, no. 5, pp. 666-687, 2010.

[10] N. E. C. Verhoest, H. Lievens, W. Wagner, J. Alvarez-Mozos, M. S. Moran, and F. Mattia, "On the soil roughness parameterization problem in soil moisture retrieval of

bare surfaces from synthetic aperture radar," *Sensors*, vol. 8, no. 7, pp. 4213-4248, 2008.

[11] M. Martin-Neira and J. M. Goutoule, "MIRAS—A two-dimensional aperture-synthesis radiometer for soil-moisture and ocean-salinity observations," *ESA Bull.*, vol. 92, pp. 95-104, 1997.

[12] D. Entekhabi, E. G. Njoku, P. E. O'Neill, K. H. Kellogg, W. T. Crow, W. N. Edelstein, J. K. Entin, S. D. Goodman, T. J. Jackson, J. Johnson, J. Kimball, J. R. Piepmeier, R. D. Koster, N. Martin, K. C. McDonald, M. Moghaddam, S. Moran, R. Reichle, J. C. Shi, M. W. Spencer, S. W. Thurman, L. Tsang, and J. Van Zyl, "The Soil Moisture Active Passive (SMAP) mission," *Proc. IEEE*, vol. 98, no. 5, pp. 704-716, 2010.

[13] T. Schmugge and T. J. Jackson, "Mapping surface soil moisture with microwave radiometers," *Meteorol. Atmos. Phys.*, vol. 54, no. 1-4, pp. 213-223, 1994.

[14] T. Pellarin, J.-P. Wigneron, J.-C. Calvet, M. Berger, H. Douville, P. Ferrazzoli, Y. H. Kerr, E. Lopez-Baeza, J. Pulliainen, L. P. Simmonds, and P. Waldteufel, "Two-year global simulation of L-band brightness temperatures over land," *IEEE Trans. Geosci. Remote Sens.*, vol. 41, no. 9, pp. 2135-2139, 2003.

[15] J.-Y. Delahaye, P. Gole, and P. Waldteufel, "Calibration error of L-band sky-looking ground-based radiometers," *Radio Sci.*, vol. 37, no. 1, 2002.

[16] F. T. Ulaby, R. K. Moore, and A. K. Fung, *MICROWAVE REMOTE SENSING: Active and Passive*, vol. I. Reading, Massachusetts: Addison-Wesley Publishing Company, 1981.

[17] G. C. Topp, J. L. Davis, and A. P. Annan, "Electromagnetic determination of soil water content: Measurements in coaxial transmission lines," *Water Resour. Res.*, vol. 16, no. 3, pp. 574-582, 1980.

[18] V. L. Mironov, L. G. Kosolapova, and S. V. Fomin, "Physically and mineralogically based spectroscopic dielectric model for moist soils," *IEEE Trans. Geosci. Remote Sens.*, vol. 47, no. 7, pp. 2059-2070, 2009.

[19] J.-P. Wigneron, Y. H. Kerr, P. Waldteufel, K. Saleh, M.-J. Escorihuela, P. Richaume, P. Ferrazzoli, P. d. Rosnay, R. Gurney, J.-C. Calvet, J. P. Grant, M. Guglielmetti, B. Hornbuckle, C. Mätzler, T. Pellarin, and M. Schwank, "L-band microwave emission of the biosphere (L-MEB) model: Description and calibration against experimental data sets over crop fields," *Remote Sens. Environ.*, vol. 107, no. 4, pp. 639-655, 2007.

[20] R. A. M. de Jeu, T. Holmes, and M. Owe, "Deriving land surface parameters from 3 different vegetated sites with the ELBARA 1.4-GHz passive microwave radiometer," *Proc. of SPIE*, vol. 5232, pp.434-443, 2004.

[21] M. Guglielmetti, M. Schwank, C. Mätzler, C. Oberdörster, J. Vanderborght, and H. Flühler, "FOSMEX: Forest soil moisture experiments with microwave radiometry," *IEEE Trans. Geosci. Remote Sens.*, vol. 46, no. 3, pp. 727-735, 2008.

[22] B. J. Choudhury, T. J. Schmugge, A. Chang, and R. W. Newton, "Effect of surface roughness on the microwave emission from soil," *J. Geophys. Res.*, vol. 84, no. C9, pp. 5699-5706, 1979.

[23] M. Schwank, I. Völksch, J.-P. Wigneron, Y. H. Kerr, A. Mialon, P. d. Rosnay, and C. Mätzler, "Comparison of two bare-soil reflectivity models and validation with L-band radiometer measurements," *IEEE Trans. Geosci. Remote Sens.*, vol. 48, no. 1, pp. 325-337, 2010.

[24] C. Mätzler, D. Weber, M. Wüthrich, K. Schneeberger, C. Stamm, and H. Flühler, "ELBARA, the ETH L-band radiometer for soil moisture research," *Proc. IEEE IGARSS*, Toulouse, France, 2003, pp. 3058-3060.

[25] K. Schneeberger, "Remote Soil Measurements–Estimation of Hydraulic Properties of Structured Soils Based on Microwave Radiometry," Ph.D. dissertation, ETH Zürich,

Zürich, Switzerland, 2003. [Online]. Available:
http://e-collection.ethbib.ethz.ch/eserv/eth:26873/eth-26873-02.pdf

[26] K. Schneeberger, C. Stamm, C. Mätzler, and H. Flühler, "Ground-based dual-frequency radiometry of bare soil at high temporal resolution," *IEEE Trans. Geosci. Remote Sens.*, vol. 42, no. 3, pp. 588-595, 2004.

[27] K. Schneeberger, M. Schwank, C. Stamm, P. d. Rosnay, C. Mätzler, and H. Flühler, "Topsoil structure influencing soil water retrieval by microwave radiometry," *Vadose Zone J.*, vol. 3, no. 4, pp. 1169-1179, 2004.

[28] M. Schwank and C. Mätzler, "Chapter 4.7: Air-to-soil transition model," in *Thermal Microwave Radiation–Applications for Remote Sensing*, C. Mätzler, Ed. London, U.K.: IET, 2006, pp. 287-301.

[29] M. Schwank, M. Stähli, H. Wydler, L. Jörg, C. Mätzler, and H. Flühler, "Microwave L-band emission of freezing soil," *IEEE Trans. Geosci. Remote Sens.*, vol. 42, no. 6, pp. 1252-1261, 2004.

[30] M. Schwank and C. Mätzler, "L-Band radiometer measurements of soil water under growing clover grass," *IEEE Trans. Geosci. Remote Sens.*, vol. 43, no. 10, pp. 2225-2237, 2005.

[31] M. Guglielmetti, "Remote Sensing of Temporally Varying Forest Soil Properties Using Microwave Radiometry," Ph.D. dissertation, ETH Zürich, Zürich, Switzerland, 2007.

[32] M. Guglielmetti, M. Schwank, C. Mätzler, C. Oberdörster, J. Vanderborght, and H. Flühler, "Measured microwave radiative transfer properties of a deciduous forest canopy," *Remote Sens. Environ.*, vol. 109, no. 4, pp. 523-532, 2007.

[33] M. Schwank, M. Guglielmetti, C. Mätzler, and H. Flühler, "Testing a new model for the L-band radiation of moist leaf litter," *IEEE Trans. Geosci. Remote Sens.*, vol. 46, no. 7, pp. 1982-1994, 2008.

[34] M. Schwank, A. Wiesmann, C. Werner, C. Mätzler, D. Weber, A. Murk, I. Völksch, and U. Wegmüller, "ELBARA II, an L-band radiometer system for soil moisture research," *Sensors*, vol. 10, no. 1, pp. 584-612, 2010.

Chapter II

L-Band Reflectivity of a Wire Grid Above a Dielectric Surface[*]

with Mike Schwank and Christian Mätzler

Abstract—**We investigated the influence of a wire grid above a paved ground on thermal brightness at 1.4 GHz. Reflectivities were derived from dual-polarized brightness temperature measurements for different grid orientations and wire spacings between 2.5 cm and 20 cm. For spacings larger than a quarter of a wavelength (≈5 cm) the grid had no impact on observed reflectivities. A physical model was used to analyze the experimental results.**

Index Terms—**Microwave radiometry, wire grids.**

1   Introduction

MICROWAVE radiometry at L band is a proven method to monitor soil moisture, which is used in the European Space Agency's Soil Moisture and Ocean Salinity (SMOS) mission [1]. Soil moisture is derived from brightness temperatures measured by the L-band radiometer on board the satellite. The reliability of the data products depends largely on the radiative-transfer models used in the retrieval, and requires calibration and validation. Therefore, several ground-based radiometer campaigns have been carried out in the past [2], and are also conducted now after the launch of the SMOS satellite. Three L-band radiometers were built and set up in Germany, Finland, and Spain for this reason [3].

L-band emission from bodies with strong dielectric anisotropy can impede soil moisture retrieval. This has been investigated for bare soils with periodic patterns [4], anisotropic vegetation [5], [6], and crop fields [7], [8]. At the SMOS core validation site in Valencia (Spain) many parallel wires are present due to the agricultural practice applied (vineyards). It is an open question if this affects L-band signatures, as the wires basically resemble a wire grid. Wire grids reflect waves, whose electric field is parallel to the wires, and transmit waves, whose electric field is perpendicular to the wires, when the wire spacing g is much smaller than the wavelength λ. When g approaches λ, the grid becomes increasingly transparent for

both field directions. This behavior has been extensively studied at millimeter and submillimeter wavelengths and is applied by the use of wire grids, e.g. as polarizers in optical applications (e.g., [9]).

The present study investigates to what extent wires used in agricultural practice can affect reflectivities at L band. To this end, brightness temperatures of a scene with a wire grid placed above a paved ground were measured for different grid orientations and wire spacings. Reflectivities, derived from the measurements, were analyzed and compared with model results. The model accounts for the multiple reflections from the grid and from the ground, and uses a multiple-beam interference approach to compute the overall reflectivity.

2   Experiment

2.1 Setup

The measurements were performed with the L-band radiometer ELBARA at the Swiss Federal Research Institute WSL in spring 2007. ELBARA was mounted on a tower with the incidence angle $\theta = 50°$ and the antenna aperture ≈ 4 m above the ground (Fig. 1). This setup was chosen to keep the footprint area small, and to ensure that self-radiation of ELBARA reflected back toward the antenna was negligible. An area of 5 m $\times$ 8 m in the radiometer footprint was leveled and paved with concrete slabs to get a horizontal and even surface. It was ascertained experimentally that radiation emitted by the surrounding grassland did not affect the signatures measured. The wire grid was a 4 m $\times$ 4 m wooden frame, strung with parallel conducting litz wires (RADOX125), 2.3 mm in diameter. The grid was placed at height $h = 32$ cm above the paving and centered just above the intersection point of the antenna axis with the ground. Its orientation is described with φ, representing the angle between the plane of incidence and the direction of the wires (Fig. 1).

2.2 Instrumentation

The Dicke-type radiometer ELBARA [10] is equipped with a dual-mode Picket horn antenna with 23.5 dB gain and a -3 dB full beam width of 12°. Brightness temperatures T_{B}^{p} are measured at horizontal ($p = $ H) and vertical ($p = $ V) polarization in the frequency range 1400$-$1427 MHz, corresponding to a vacuum wavelength of $\lambda \approx 21$ cm. Internal hot (338 K) and cold sources (278 K) are used for internal calibration. The absolute accuracy of ELBARA is around ± 1 K for the 12 s integration time considered, and its sensitivity is < 0.1 K. Sky brightness T_{sky} was measured regularly. By comparing T_{sky} measured with theoretical sky radiance [11], the measured T_{B}^{p}'s were corrected for instrumental noise.

Additionally, ground temperatures were measured *in situ* at 5 cm and at 17 cm depth. They were used to estimate the effective ground temperature T_{eff}, which predominantly determines T_{B}^{p} (see Section 3.1).
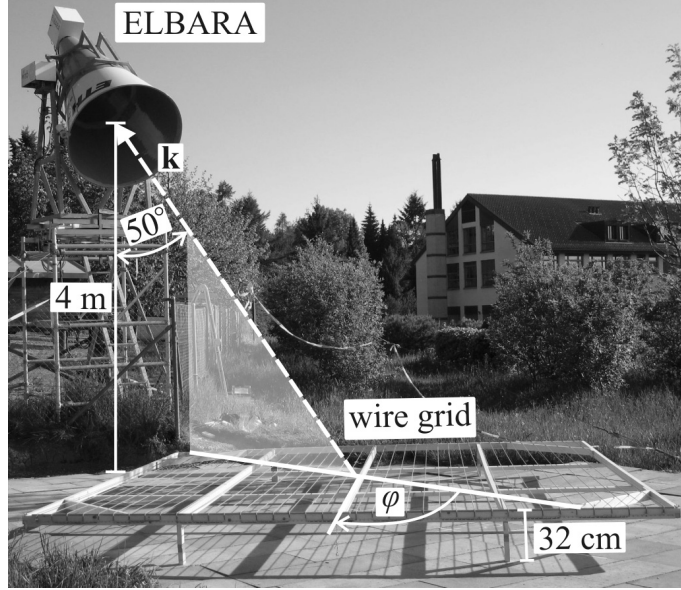
Fig. 1. Setup of the wire grid experiments. The dashed arrow is the direction of the propagation vector **k** of the radiance measured; the shaded area illustrates the plane of incidence.

2.3 Measurements

Measurements were carried out on warm, dry, and sunny days ($T_{\text{air}} = (27.1 \pm 3.5)$ °C), so that ground temperatures ($T_{\text{eff}} = (25.0 \pm 2.5)$ °C) and moisture were as similar as possible on different days. Brightness temperatures T_{B}^p of the *grid–ground system* described in Section 2.1 were measured for wire spacings $g = 20, 10, 5,$ and 2.5 cm, each at ten different grid orientations φ between 0° (wires parallel to the plane of incidence) and 90° (wires perpendicular to the plane of incidence). The grid orientation φ was changed by manually rotating the grid about its center in steps of 10°.

3 Models

3.1 Radiative-Transfer Model

Brightness temperatures T_{B}^p of the grid–ground system were modeled as the linear combination of the radiances emitted from the area covered by the wire grid and from the surrounding paved area, which contribute with the fractional amounts μ^p and $(1 - \mu^p)$, respectively. The corresponding reflectivities are the reflectivity of the grid above the ground (*grid–ground reflectivity*) R^p and the reflectivity R_0^p of the paved ground

$$T_{\text{B}}^p = \mu^p \left[(1 - R^p)T_{\text{eff}} + R^p T_{\text{sky}} \right] + (1 - \mu^p)\left[(1 - R_0^p)T_{\text{eff}} + R_0^p T_{\text{sky}} \right]. \tag{1}$$

The effective ground temperature T_{eff} was assumed as the mean of the ground temperatures measured in 5 cm and in 17 cm depth. The resulting error of R^p due to this approximation is

negligible (< 0.02 for an error of 5 K in T_{eff}), when using (1) to derive R^p from T_{B}^p. The weighting μ^p was derived from the measurements of the following: 1) just the paved area ($T_{\text{B,0}}^p$), and 2) the wire grid, covered with a reflector (aluminum mesh with mesh size ≈ 2 mm) with $R^p = 1$ ($T_{\text{B,mesh}}^p$). Using $T_{\text{B,0}}^p$ with $\mu^p = 0$ in (1) yields R_0^p. Inserting measured $T_{\text{B,mesh}}^p$ and $R^p = 1$, together with the previously determined R_0^p, into (1) yields

$$\mu^p = \frac{T_{\text{B,0}}^p - T_{\text{B,mesh}}^p}{T_{\text{B,0}}^p - T_{\text{sky}}} . \tag{2}$$

As the measured μ^p's were very similar at both polarizations, the mean $\mu = 0.87$ was used in (1). The reflectivity of the paved ground was determined to be $R_0^{\text{H}} = 0.34$ and $R_0^{\text{V}} = 0.12$.

3.2 Grid–Ground Reflectivity Model

To model the grid–ground reflectivity, the field propagation directions are reversed, i.e. ELBARA is considered as a transmitter of radiance directed onto the grid–ground system (Fig. 2). From the corresponding incident electric field $\mathbf{E}$, the field $\mathbf{E}_{\text{ref}}$ reflected in forward direction is computed. Thereafter, the reflectivity is derived as the ratio between the energies carried by $\mathbf{E}_{\text{ref}}$ and $\mathbf{E}$. Determining $\mathbf{E}_{\text{ref}}$ requires the following steps: 1) the fields reflected and transmitted by the grid and the fields reflected by the ground are computed, and 2) the fields are superposed, yielding $\mathbf{E}_{\text{ref}}$ reflected by the grid–ground system.

3.2.1 Reflection and Transmission by the Wire Grid

To describe reflection and transmission by the grid, the electric field $\mathbf{E}$ of an incident wave is decomposed into two orthogonal components ($E^{\text{H}}, E^{\text{V}}$) along the direction of horizontal (i.e., perpendicular to the plane of incidence) and vertical (i.e., parallel to the plane of incidence) polarization. The polarization of the fields of the waves reflected and transmitted by the grid are rotated with respect to $\mathbf{E} = (E^{\text{H}}, E^{\text{V}})$ as a result of the anisotropic reflection characteristics of wire grids. This is described with the following matrix notation:

$$\mathbf{r}_{\text{grid}} = \begin{pmatrix} r_{\text{grid}}^{\text{HH}} & r_{\text{grid}}^{\text{VH}} \\ r_{\text{grid}}^{\text{HV}} & r_{\text{grid}}^{\text{VV}} \end{pmatrix} \quad \mathbf{t}_{\text{grid}} = \begin{pmatrix} t_{\text{grid}}^{\text{HH}} & t_{\text{grid}}^{\text{VH}} \\ t_{\text{grid}}^{\text{HV}} & t_{\text{grid}}^{\text{VV}} \end{pmatrix} \tag{3}$$

which allows writing the reflected and transmitted fields as $\mathbf{r}_{\text{grid}}\mathbf{E}$ and $\mathbf{t}_{\text{grid}}\mathbf{E}$, respectively. The matrix elements $r_{\text{grid}}^{pp'}$ and $t_{\text{grid}}^{pp'}$ in (3) are the field reflection and transmission coefficients associated with the polarization p of the incident field and the polarization p' of the field after interaction with the grid. Considering, for example, a horizontally polarized field $\mathbf{E} = (E^{\text{H}}, 0)$ incident on the grid results in the reflected field $\mathbf{r}_{\text{grid}}\mathbf{E} = \left(r_{\text{grid}}^{\text{HH}} E^{\text{H}}, r_{\text{grid}}^{\text{HV}} E^{\text{H}} \right)$ and the transmitted field $\mathbf{t}_{\text{grid}}\mathbf{E} = \left(t_{\text{grid}}^{\text{HH}} E^{\text{H}}, t_{\text{grid}}^{\text{HV}} E^{\text{H}} \right)$, with both comprising a co- (i.e., horizontally) and a cross- (i.e., vertically) polarized field component.

The values to be used in (3) were calculated with [12, eqs. (4.50)–(4.53)]. In [12], the complex reflection and transmission coefficients $r_{\text{grid}}^{pp'}$ and $t_{\text{grid}}^{pp'}$ are derived by solving Max-
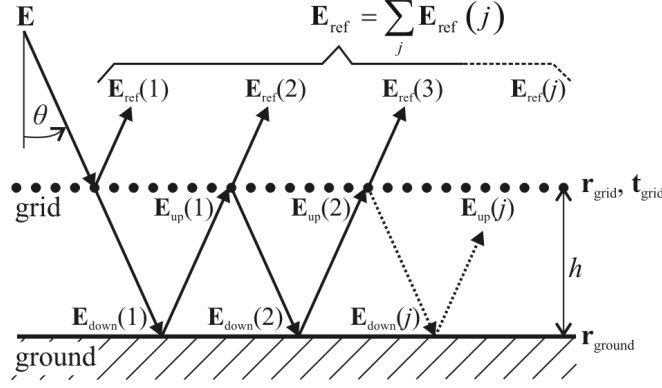
Fig 2. Sketch of the grid–ground system with the incident field $\mathbf{E}$, the fields $\mathbf{E}_{\text{down}}(j)$ and $\mathbf{E}_{\text{up}}(j)$ propagating between the grid and the ground, and the fields $\mathbf{E}_{\text{ref}}(j)$ $(j = 1, ..., n)$ propagating in the upward direction above the grid.

well's equations on a grid for arbitrary angles of incidence and grid orientations. Further parameters needed in the model are the wavelength of the incident radiation, the wire radius and spacing, and the wire impedance.

3.2.2 Reflection by the Ground

Analysis of ground reflectivities R_0^p, available from the $T_{\text{B},0}^p$- measurements of the paved area (Section 3.1) revealed that reflection by the ground is almost Fresnelian with the Brewster angle $\theta_{\text{B}} \approx 70°$. Reflection of a field $\mathbf{E} = (E^{\text{H}}, E^{\text{V}})$ incident on the isotropic ground can likewise be described in matrix notation as $\mathbf{r}_{\text{ground}}\mathbf{E}$, using

$$\mathbf{r}_{\text{ground}} = \begin{pmatrix} -r_{\text{ground}}^{\text{H}} & 0 \\ 0 & r_{\text{ground}}^{\text{V}} \end{pmatrix}. \tag{4}$$

The absolute values of the field reflection coefficients were estimated as $\left| r_{\text{ground}}^p \right| = \sqrt{R_0^p}$. Reflection at H-polarization is accompanied by a phase shift of π; at V-polarization, no phase shift occurs, as the incidence angle is significantly smaller than θ_{B}.

3.2.3 Multiple-Beam Interference Approach

The total field $\mathbf{E}_{\text{ref}}$ reflected by the grid–ground system is modeled as the coherent superposition of n partially reflected fields $\mathbf{E}_{\text{ref}}(j)$ (Fig. 2)

$$\mathbf{E}_{\text{ref}} = \sum_{j=1}^{n} \mathbf{E}_{\text{ref}}(j). \tag{5}$$

The fields $\mathbf{E}_{\text{ref}}(j)$ itself are computed iteratively. Thereby, reflection and transmission by the grid and reflection by the ground are computed by applying the matrices (3) to fields incident on the grid and (4) to fields incident on the ground. The primary reflected field $\mathbf{E}_{\text{ref}}(1) = \mathbf{r}_{\text{grid}}\mathbf{E}$ is deduced directly from the incident field $\mathbf{E} = (E^{\text{H}}, E^{\text{V}})$. The remainder

$\mathbf{E}_{\text{down}}(1) = \mathbf{t}_{\text{grid}}\mathbf{E}$ propagates downward below the grid. Part of it is then reflected by the ground with $\mathbf{r}_{\text{ground}}$ and propagates toward the grid. With the complex factor $Q^2 = \exp(-\mathrm{i} \cdot 4\pi h \cos\theta / \lambda)$ representing the phase shift caused by one round trip through the grid–ground system, this yields:

$$\mathbf{E}_{\text{up}}(1) = Q^2 \mathbf{r}_{\text{ground}} \mathbf{t}_{\text{grid}} \mathbf{E}\,. \tag{6}$$

On the grid, $\mathbf{E}_{\text{up}}(1)$ is partially reflected downward with $\mathbf{r}_{\text{grid}}$, yielding $\mathbf{E}_{\text{down}}(2)$, and partially transmitted with $\mathbf{t}_{\text{grid}}$, yielding $\mathbf{E}_{\text{ref}}(2)$. Iteratively applying this procedure results in $\mathbf{E}_{\text{down}}(j)$ and $\mathbf{E}_{\text{up}}(j)$ bouncing back and forth between the grid and the ground with the amplitude of the jth upwelling field decaying with the power of j

$$\mathbf{E}_{\text{up}}(j) = Q^2 \mathbf{r}_{\text{ground}} \mathbf{r}_{\text{grid}} \mathbf{E}_{\text{up}}(j-1)\,. \tag{7}$$

This expression can be evaluated for $j = 2, \dots, n$, using $\mathbf{E}_{\text{up}}(1)$ given by (6). The fields $\mathbf{E}_{\text{ref}}(j)$ to be used in (5) are then calculated with

$$\mathbf{E}_{\text{ref}}(j) = \mathbf{t}_{\text{grid}} \mathbf{E}_{\text{up}}(j)\,. \tag{8}$$

For the numerical calculation of $\mathbf{E}_{\text{ref}}$, it was found to be sufficient to evaluate (5) up to $n = 10$.

3.2.4 Grid–Ground Reflectivity

To calculate the power reflectivity R of the grid–ground system, the radiometer is considered as a transmitter of an electric field $\mathbf{E}$ with $|\mathbf{E}| = 1$, and the sky is regarded as a "receiver", absorbing the total energy carried by the field $\mathbf{E}_{\text{ref}}$. This implies that R is the ratio between the reflected energy carried by $\mathbf{E}_{\text{ref}}$ and the energy transmitted by the radiometer

$$R = \frac{\left|\mathbf{E}_{\text{ref}}\right|^2}{\left|\mathbf{E}\right|^2} = \left|\mathbf{E}_{\text{ref}}\right|^2\,. \tag{9}$$

4 Results and Discussion

4.1 Grid–Ground Reflectivities Measured

Figure 3 shows the reflectivities R^p (p = H, V) of the grid–ground system measured for wire spacings g = 20, 10, 5, and 2.5 cm at grid orientations $0° \leq \varphi \leq 90°$. For g = 20 cm (circles), no clear dependence of R^p on φ can be identified. As expected, the transmissivity of the grid with g = 20 cm $\approx \lambda$ is close to unity at both polarizations, and consequently, R^p's approach the reflectivities R_0^p of the paved area (see Section 3.1).

The grid configuration with g = 10 cm (stars) provides the first evidence that R^p is affected by the presence of the grid and thus is dependent on φ. This is observed only at V-polariza-
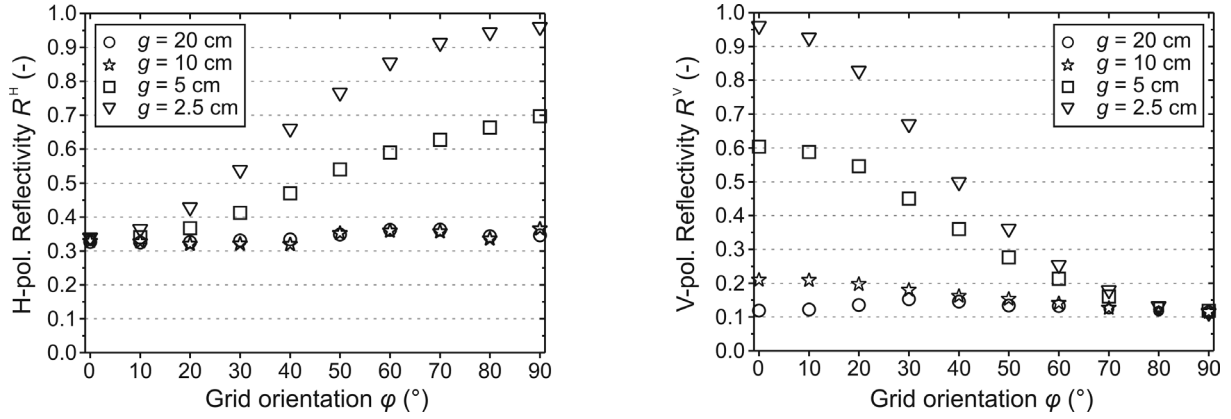
Fig. 3. Observed reflectivities of the grid–ground system at horizontal (left) and vertical polarization (right).

tion, however. At H-polarization, the same values as for $g = 20$ cm are observed, which is ascribed to absorption effects. Absorption by the lossy wooden bars of the grid frame is significant at H-polarization due to the alignment of the bars with the electric field vector (Fig. 1) and thus surpasses the small change in R^H caused by the presence of the wires. This effect also shows a dependence on φ as the alignment of the bars with the electric field vector changes with the grid orientation.

At $g = 5$ cm (squares), R^H clearly increases, and R^V clearly decreases with increasing φ. At 0° and 10°, R^H is very similar to the ground reflectivity R_0^H. With further increasing φ, however, R^H gradually increases to 0.7 at 90°. At V-polarization, the highest value of $R^V = 0.6$ is observed at 0°. R^V then gradually decreases until it matches R_0^V at 80° and 90°. This antipodal behavior of R^H and R^V is explained by the orthogonality of the H- and V-polarized fields and their orientation with respect to the wires. On the one hand, the grid with $g = 5$ cm $\approx \lambda/4$ is highly transparent when the field is perpendicular to the wires ($\varphi = 0°$ at $p = $ H and $\varphi = 90°$ at $p = $ V). On the other hand, the grid substantially reflects the wave when the electric field is parallel to the wires ($\varphi = 90°$ at $p = $ H and $\varphi = 0°$ at $p = $ V).

Reflectivities measured for the smallest realized wire spacing $g = 2.5$ cm (triangles) are even more sensitive to φ. R^p's slightly below unity are measured at both polarizations for fields parallel to the wires. However, the grid is still perfectly transparent for fields perpendicular to the wires. This observation is very similar to what is expected for an ideal wire grid. For further investigation, measured reflectivity data are compared to model simulations in the following.

4.2 Comparison of Measured and Modeled Reflectivities

Figure 4 shows the comparison between the measured and the modeled grid–ground reflectivities R^p for $g = 2.5$ cm. The gray shaded areas show the ranges of R^p, resulting from evaluating the model for grid heights 30 cm $\leq h \leq$ 40 cm. These calculations were performed, as h exhibits a certain experimental uncertainty: 1) Slightly sagging wires lead to downward deviations from the aspired grid height, and 2) the radiometrically relevant height is slightly
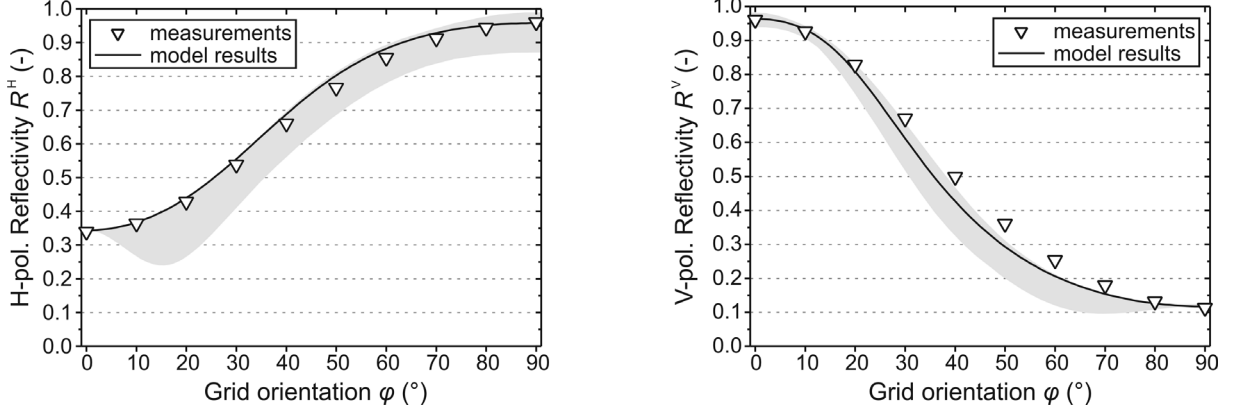
Fig 4. Comparison of modeled and measured grid–ground reflectivities for wire spacing $g = 2.5$ cm at horizontal polarization (left) and vertical polarization (right). The gray shaded areas show the ranges of R^p, resulting from evaluating the model for grid heights 30 cm $\leq h \leq$ 40 cm.

larger than the geometric height, as reflection on the ground occurs somewhat below the ground surface. The exact height of the grid above the ground reflection is not known, but is assumed to be within the considered range. The solid lines are R^p, modeled for $h = 31$ cm ($p = $ H) and 38 cm ($p = $ V), where the measurements (triangles) were reproduced best. Anisotropy in the effective ground permittivity could explain the difference between the optimal heights for H- and V-polarization.

Simulations and measurements agree perfectly at both polarizations, when the electric field is perpendicular to the wires. For this limiting case, the measured, as well as the modeled, R^p's are equal to the ground reflectivity R_0^p. This is partly inherent in the model, as it uses the same R_0^p values to represent reflection by the ground as those used in (1) to derive R^p from the measured T_B^p.

For the other limiting case, where the electric field is parallel to the wires, model results vary around the measured values $R^H = R^V = 0.96$, depending on the height for which the model was evaluated ($0.87 \leq R^H \leq 0.99$ and $0.93 \leq R^V \leq 0.98$). For $h = 31$ cm ($p = $ H) and 38 cm ($p = $ V), the modeled R^p's match the measured values exactly.

At intermediate grid orientations, R^H computed for $h = 31$ cm agrees well with the measurements at H-polarization. The largest deviation observed at $\varphi = 50°$ amounts to less than 0.04. When considering the range of R^H modeled for 30 cm $\leq h \leq$ 40 cm, the measured reflectivities are explained for all φ.

At V-polarization, model results agree somewhat less well with the measurements at the intermediate grid orientations. R^V computed for $h = 38$ cm underestimate the measured reflectivities for $30° \leq \varphi \leq 70°$ with maximum deviations of 0.07 at $\varphi = 40°$. When other heights in the range 30 cm $\leq h \leq$ 40 cm are considered, the measured reflectivities can still not be matched. This underestimation of R^V by the model cannot be explained conclusively. Possibly, it is due to errors in the phases of the superposed fields, which are caused by locally varying grid heights and not perfectly represented phase shifts at the ground surface.

Altogether, model calculations yielded good results for $g = 2.5$ cm. The main features of the measured reflectivities were reproduced well, but a strong sensitivity to the grid height h became apparent, which is due to the coherent nature of the computation. Small uncertainties in h affect the phases of the superposed fields $\mathbf{E}_{ref}(j)$ used in (5), which affects the overall reflectivity considerably. This becomes even more important when larger wire spacings are considered, as a larger fraction of radiance is transmitted through the grid. Consequently, model results become ambiguous because the reflectivities vary widely with h.

5 Final Remarks

This study demonstrates the impact of pronounced dielectric anisotropy within a scene on thermal radiation at 1.4 GHz. Despite the artificial setup, the findings can be taken as proxy for natural emitters displaying striped dielectric anisotropy (e.g., aligned vegetation) and for areas displaying similar artificial structures (e.g., supporting wires in fruit-growing).

When corresponding spatial periodicities are $\leq \lambda/4$, reflectivities derived from brightness temperature measurements can differ greatly depending on the orientation of the patterns. This can impact the retrieval of geophysical quantities from thermal brightness considerably. The model developed was able to reproduce such effects satisfactorily for a scene exhibiting extreme dielectric anisotropy (a wire grid with a wire spacing of 2.5 cm $\approx \lambda/10$ placed above an almost specular surface). The calculations also showed the difficulties involved in modeling such an apparently simple configuration, when sensitive system parameters exhibit a certain experimental uncertainty.

However, experimental results clearly showed that such striped dielectric patterns do not affect microwave signatures, and can therefore be neglected in retrieval algorithms, if their periodicities are $> \lambda/4$ (≈ 5 cm at 1.4 GHz). Amongst others, this is an important message in view of the SMOS anchor station in Valencia. It implies that the considerable number of supporting wires present in this area will not interfere with the validation and calibration of the SMOS soil moisture products.

Acknowledgement

References

[1] Y. H. Kerr, P. Waldteufel, J.-P. Wigneron, J.-M. Martinuzzi, J. Font, and M. Berger, "Soil moisture retrieval from space: The Soil Moisture and Ocean Salinity (SMOS) mission," *IEEE Trans. Geosci. Remote Sens.*, vol. 39, no. 8, pp. 1729-1735, 2001.

[2] J.-P. Wigneron, Y. H. Kerr, P. Waldteufel, K. Saleh, M.-J. Escorihuela, P. Richaume, P. Ferrazzoli, P. d. Rosnay, R. Gurney, J.-C. Calvet, J. P. Grant, M. Guglielmetti, B. Hornbuckle, C. Mätzler, T. Pellarin, and M. Schwank, "L-band Microwave Emission of the Biosphere (L-MEB) Model: Description and calibration against experimental data sets over crop fields," *Remote Sens. Environ.*, vol. 107, no. 4, pp. 639-655, 2007.

[3] M. Schwank, A. Wiesmann, C. Werner, C. Mätzler, D. Weber, A. Murk, I. Völksch, and U. Wegmüller, "ELBARA II, an L-band radiometer system for soil moisture research," *Sensors*, vol. 10, no. 1, pp. 584-612, 2010.

[4] J. R. Wang, R. W. Newton, and J. W. Rouse, "Passive microwave remote sensing of soil moisture: The effect of tilled row structure," *IEEE Trans. Geosci. Remote Sens.*, vol. GE-18, no. 4, pp. 296-302, 1980.

[5] M. Schwank and C. Mätzler, "L-Band radiometer measurements of soil water under growing clover grass," *IEEE Trans. Geosci. Remote Sens.*, vol. 43, no. 10, pp. 2225-2237, 2005.

[6] P. Ferrazzoli, L. Guerriero, and J.-P. Wigneron, "Simulating L-band emission of forests in view of future satellite applications," *IEEE Trans. Geosci. Remote Sens.*, vol. 40, no. 12, pp. 2700-2708, 2002.

[7] B. K. Hornbuckle, A. W. England, Roger D. De Roo, M. A. Fischman, and D. L. Boprie, "Vegetation canopy anisotropy at 1.4 GHz," *IEEE Trans. Geosci. Remote Sens.*, vol. 41, no. 10, pp. 2211-2223, 2003.

[8] J.-P. Wigneron, M. Pardé, P. Waldteufel, A. Chanzy, Y. Kerr, S. Schmidl, and N. Skou, "Characterizing the dependence of vegetation model parameters on crop structure, incidence angle, and polarization at L-Band," *IEEE Trans. Geosci. Remote Sens.*, vol. 42, no. 2, pp. 416-425, 2004.

[9] J. M. Bennet, "Chapter 3: Polarizers," in *Handbook of Optics*, vol. II, M. Bass, E. W. van Stryland, D. R. Williams, and W. L. Wolfe, Eds. New York: McGraw-Hill, 1995, pp. 3.1-3.70.

[10] C. Mätzler, D. Weber, M. Wüthrich, K. Schneeberger, C. Stamm, and H. Flühler, "ELBARA, the ETH L-Band radiometer for soil moisture research," in *Proc. IGARSS*, Toulouse, France, 2003, pp. 3058-3060.

[11] T. Pellarin, J.-P. Wigneron, J.-C. Calvet, M. Berger, H. Douville, P. Ferrazzoli, Y. H. Kerr, E. Lopez-Baeza, J. Pulliainen, L. P. Simmonds, and P. Waldteufel, "Two-year global simulation of L-band brightness temperatures over land," *IEEE Trans. Geosci. Remote Sens.*, vol. 41, no. 9, pp. 2135-2139, 2003.

[12] S. A. Tretyakov, "Chapter 4: Periodical Structures, Arrays, and Meshes," in *Analytical Modeling in Applied Electromagnetics*. Norwod, MA: Artech House, 2003, pp. 69-117.

Chapter III

L-Band Reflectivity of a Furrowed Soil Surface[*]

with Mike Schwank and Christian Mätzler

Abstract—**In a combined experimental and model study, we investigated thermal L-band signatures of a sandy soil with periodic topography (furrows) with dimensions close to the observation wavelength of 21 cm. Measurements were carried out with a radiometer mounted on a tower and aimed at a soil box with an artificially prepared furrowed soil surface. Corresponding reflectivities were derived from brightness temperature measurements performed under dry and moist conditions, with the furrow direction either along or perpendicular to the plane of incidence. Results showed the furrows had a pronounced effect on the reflectivity, depending on the polarization of the observed radiance, the direction of the furrows and the soil moisture.**

A physical reflectivity model for dielectric periodic surfaces was used to explain the soil reflectivities measured for the different furrow directions and soil-water contents. Using this model improved the agreement between the measured and modeled reflectivities considerably compared to the Fresnel reflectivities. The observed dependence of soil reflectivity on furrow orientation and soil moisture could be reproduced by the reflectivity model. The quantitative agreement with the observed reflectivities was further improved by using a simple empirical approach to consider the small-scale heterogeneity of the top soil layer.

Index Terms—**Electromagnetic scattering by periodic structures, electromagnetic scattering by rough surfaces, microwave radiometry, permittivity.**

1 Introduction

THE TERRESTRIAL surface layer is one of the major components of the climate system. Mass and energy fluxes at the Earth's surface control how energy received from the sun is returned to the atmosphere, thus influencing the climate considerably. The quantities involved in this mass and energy exchange are fundamentally linked with the moisture in the soil surface. For example, soil moisture strongly controls infiltration processes and the

amount of water dissipated to the atmosphere via evaporation and transpiration. Therefore, it is crucial to know how much water is stored in the top soil layer, in order to understand the processes that link the terrestrial water and energy cycles.

Almost 30 years ago, it was suggested that soil moisture could be retrieved from remotely sensed thermal radiance measured with an L-band (1–2 GHz) microwave radiometer [1], [2]. Today, L-band radiometry is one of the most promising approaches for remotely monitoring soil moisture on a large scale. It has the advantage of being unaffected by cloud cover and solar radiation, which allows all-weather continuous (day and night) measurements. Furthermore, the emission depth in soils is relatively large and the vegetation canopy is semi-transparent at L Band. The sensitive 1400−1427 MHz frequency band of most L-band radiometers is protected, which means that disturbances due to anthropogenic interferences are minimized.

Microwave radiometry is also being deployed in the recently launched Soil Moisture and Ocean Salinity (SMOS) mission of the European Space Agency. The Microwave Imaging Radiometer using Aperture Synthesis (MIRAS) on board the SMOS satellite provides global coverage of L-band brightness temperatures with a spatial resolution of approximately 50 km. The primary objective of the mission is to produce global soil moisture maps with an accuracy better than 4 vol.% and ocean salinity maps with an accuracy of 0.5–1.5 practical salinity units [3]. The reliability of these data products depends largely on the performance of the emission models applied to interpret the brightness temperatures measured on the corresponding footprints. For this reason, a large number of ground-based (e.g., [4]) and airborne radiometer experiments (e.g., [5]) at L Band over various types of terrestrial surfaces have been performed during recent decades.

It has been demonstrated that the brightness temperatures measured are affected not only by the surface moisture, but also by other parameters such as soil roughness and topography. This finding has led to extensive research on the impact of random surface roughness on the signatures measured (e.g., [6]–[9]). However, a periodic topography of a soil surface can also affect the thermal microwave signatures [10], [11]. Examples of such terrestrial surfaces are soils undergoing erosion and dispersal processes, which can produce gullies preferentially aligned with the slope. Agricultural fields may also have pronounced periodic structures, in particular furrows produced as the result of, e.g. plowing, sowing, or furrow irrigation.

Extensive experimental and theoretical investigations have been dedicated to the emission properties of periodic surfaces in the context of L-band brightness temperature measurements over the surface of the sea. Knowing these properties made it possible to correct for wind effects in sea salinity retrievals [12]. Moreover, correlations between wind direction and the characteristics of the formed periodic surface waves can be used to retrieve wind direction [13]. Although the theoretical background is available (e.g., [14] and [15]), to our knowledge not many experimental studies have been dedicated to the thermal emission of soils with periodic surface features in the range of the observation wavelength.

To investigate the thermal emission of a soil with a well-defined one-dimensional periodic topography, parallel furrows with a periodicity of ≈27 cm were imprinted into a bare soil surface. Brightness temperatures at 1.4 GHz were then measured under dry- and moist-soil con-

ditions, for soil with furrows either aligned with or perpendicular to the plane of incidence (Section 2). For comparison, smooth soil surfaces were also measured under each moisture condition. From the brightness temperatures measured, the corresponding reflectivities were derived (Section 3.1) to investigate the impact of the periodic topography on the soil reflectivity for the different furrow orientations and soil moistures. As the observation wavelength ($\lambda \approx 21$ cm) was similar to the surface periodicity, a physical reflectivity model (Section 3.2) was implemented to explain the topography-related aspects of the signatures measured. Modeled values were then additionally corrected for further effects not accounted for in the physical reflectivity model (e.g., small-scale heterogeneity of the top soil layer) with a simple empirical approach (Section 3.4). The reflectivity changes caused by the differently oriented furrows under dry- and moist-soil conditions are discussed on the basis of the measurements and the corresponding model calculations in Section 4.

2 Experiment

Measurements were performed with the L-band radiometer ELBARA [16] at the Swiss Federal Research Institute WSL in Birmensdorf (Switzerland) in January 2008 (Fig. 1). A soil box was placed in ELBARA's footprint and brightness temperatures were measured for three different soil topographies under dry- and moist-soil conditions. The experimental setup, the remote sensing system, and the measurements performed are described in more detail below.

2.1 Setup

ELBARA was mounted on a small tower with the observation angle $\theta = 50°$ relative to the vertical direction and the antenna aperture approximately 4 m above the ground (Fig. 1a). An area of about 5 m × 8 m in the radiometer footprint was leveled and paved with concrete slabs to achieve a horizontal and even surface. The paving covered at least the −12 dB footprint of ELBARA. It was ascertained experimentally that radiation emitted by the grassland surrounding the paving did not affect the signatures measured.

The 3 m × 4 m × 0.3 m soil box (made of 3 cm wooden planks mounted on top of a steel frame) was placed in the centre of the paved area with its long sides aligned with the plane of incidence. It was filled with sandy soil from the research catchment "Chicken Creek" [17]. Prior to this, the soil was sieved to remove clumps of soil particles larger than 5 mm, resulting in a homogenous sandy soil (soil texture: 88% sand, 7% silt, 5% clay) with a density of $1535 \text{ kg} \cdot \text{m}^{-3}$ and a porosity of approximately 25%. When filling the box, a layer of moist soil was placed at the bottom and gradually drier material added on top. This resulted in a rather smooth soil moisture profile, with the soil-water content wc decreasing from $\approx 0.2 \text{ m}^3 \cdot \text{m}^{-3}$ at the bottom of the soil box to $\approx 0.01 \text{ m}^3 \cdot \text{m}^{-3}$ in the top soil layer. The power penetration depth of the moist soil with $wc = 0.2 \text{ m}^3 \cdot \text{m}^{-3}$ was estimated as $\lambda / \left(4\pi \operatorname{Im} \sqrt{\varepsilon} \right) \approx 5 \text{ cm}$, whereas $\lambda \approx$ 21 cm is the observation wavelength and $\varepsilon \approx 16 + i3$ is the relative permittivity of the soil (see Section 3.3 for the relationship between wc and ε of the soil investigated). This indicates that the radiance emitted from the pavement below could not permeate the soil box and interfere

with the upward emission of the soil. Furthermore, the gradual moisture profile reduced coherent effects due to layering, which, however, cannot be ruled out altogether.

This setup with the shallow observation angle $\theta = 50°$ and the small distance of ≈ 5 m between the antenna aperture and the observed scene was chosen as a compromise. On the one hand, it ensured that the self-radiation of the antenna reflected back toward the antenna aperture was negligible, while, on the other hand, the footprint area was kept very confined so that the measured signatures were largely determined by the soil-box reflectivity. The observed scene was still within the near field of the antenna with this setup. Therefore, the fractional contribution of the soil-box radiance to the total radiance received could not be estimated using the theoretical antenna far-field pattern [18]. Instead, we determined this quantity experimentally, as described in Section 3.1.

2.2 Instrumentation

The ETH L-band radiometer ELBARA [16] was constructed at the Institute of Applied Physics, University of Bern (Switzerland) in 2001 and has been successfully deployed in numerous experiments since then [19]–[25]. It is equipped with a dual-mode Picket-horn antenna [18] (aperture diameter $d = 1.4$ m, length $l = 2.7$ m) with 23.5 dB gain and a –3 dB full beam width of 12°. ELBARA measures brightness temperatures T_{B}^{p} at horizontal ($p = $ H) and vertical ($p = $ V) polarization in the protected frequency band 1400–1427 MHz ($\lambda \approx 21$ cm). Two slightly overlapping frequency channels, each with a bandwidth of 18 MHz (1400–1418 MHz and 1409–1427 MHz), are measured quasi-simultaneously to enable the detection of narrow-band radio frequency interference (RFI) within the protected band. As no disturbances due to RFI were encountered during the measurements, the brightness temperatures associated with the two channels were averaged to use the total bandwidth of 27 MHz. The measurements were recorded with 12 s integration time, yielding a large time–bandwidth product. The estimated absolute accuracy of the T_{B}^{p} measured was ±1 K and the sensitivity was better than 0.1 K. The measured T_{B}^{p} were corrected for the radiance originating from the cables connecting the antenna with the radiometer electronics, by comparing the measured sky brightness T_{sky} with the values calculated with [26], and then correcting the measurements accordingly, as described in [27].

In addition to the radiometer measurements, air and ground temperatures were also measured. Air temperature T_{air} was recorded with a shaded Pt-100 temperature sensor installed on the radiometer scaffolding, and *in situ* soil temperatures T_{18cm} were measured with three thermistors (Campbell S-TL107) buried in the soil along a transect at a depth of 18 cm. The accuracy of these temperature measurements was approximately ±1 K. The T_{18cm} and T_{air} were used to estimate the effective temperature T_{eff}, which predominantly determines T_{B}^{p} (Section 3.1).

2.3 Measurements

Brightness temperature measurements were performed on 10 and 19 January 2008. Both days were dry, sunny and unseasonably warm, with mean air temperatures during the meas-
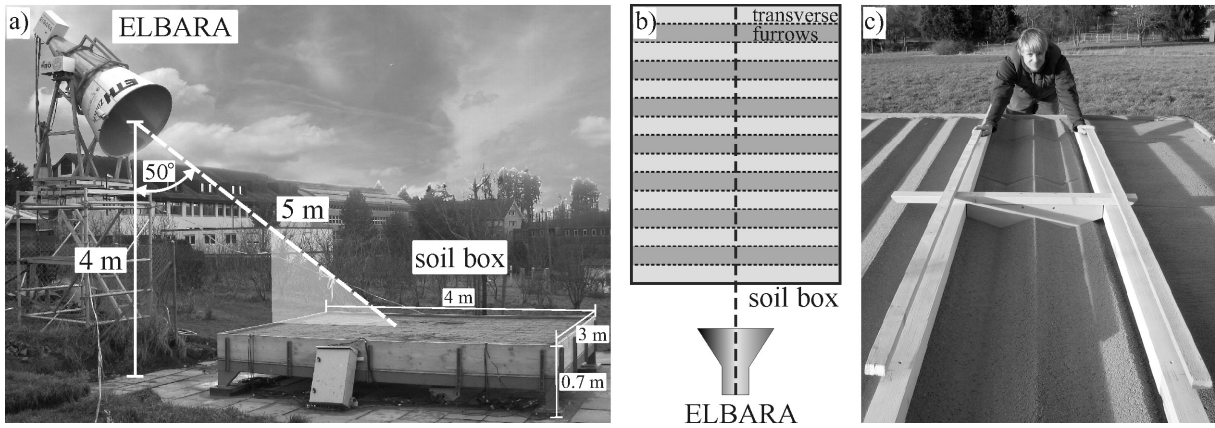
Fig. 1. a) Setup of the experiment. The dashed line is the antenna main axis, the shaded area illustrates the plane of incidence. b) Sketch of the setup as seen from above with transverse furrows (i.e., furrow orientation perpendicular to the plane of incidence) imprinted into the soil surface. c) Preparation of the furrowed surface.

urements of 12 °C and 13 °C, respectively. Mild and rainy weather prevailed between the two days of measurements, resulting in a natural wetting of the sandy soil. On 10 January (dry-soil measurements), the near-surface soil-water content was determined to be $wc = 0.014 \ \mathrm{m^3 \cdot m^{-3}}$ from soil samples taken from the surface layer (approximately the topmost 5 cm). On 19 January (moist-soil measurements), wc ranged from 0.067 to 0.094 $\mathrm{m^3 \cdot m^{-3}}$.

Three different types of surface topography were prepared for the T_{B}^{p} measurements: 1) a surface with periodic furrows parallel to the plane of incidence (*longitudinal furrows*); 2) a surface with periodic furrows perpendicular to the plane of incidence (*transverse furrows*, illustrated in Fig. 1b); and 3) a *plane surface* (i.e., smoothed surface without furrows). The plane surface was prepared by pulling a board back and forth over the soil until the surface was very smooth. This resulted in a surface with reflection characteristics that were as close to specular (Fresnel) reflection as was experimentally feasible. The furrowed surfaces were prepared from plane surfaces by pulling a wooden stencil formed like a triangular snow plough through the soil (Fig. 1c) in either a longitudinal or a transverse direction. The cross sections of the longitudinal and the transverse furrows were identical and can be described as an isosceles triangle with an altitude of 5 cm, side lengths of ≈15 cm, and a base length of ≈27 cm, corresponding to the period P of the furrows (Fig. 2). This geometry was chosen to resemble "natural" structures such as irrigation or plowing furrows to some degree, while at the same time being experimentally feasible and well defined. The smoothness of the furrow faces was approximately the same as the smoothness of the plane surface.

During both the dry-soil and the moist-soil measurements, the soil topography was changed in the following order: 1) plane surface, 2) surface with longitudinal furrows, 3) plane surface, 4) surface with transverse furrows, and 5) plane surface. For each soil topography 1) to 5), T_{B}^{p} were measured 20 times, and two soil samples were taken randomly from the top soil layer, from which wc was determined gravimetrically in the laboratory. Afterwards, the next topography was prepared, and the procedure was repeated in the same way.

These measurements resulted in a data set of T_B^p for the plane and for the two furrowed soil surfaces at different *wc*. The three measurements, namely 1), 3), and 5), of the plane surface under dry and moist conditions provided a reference, which helped to distinguish the T_B^p variations due to the different topographies from the changes caused by varying *wc*.

3 Models

Reflectivities R^p of the soil under test were derived from the T_B^p measurements of the soil box placed in the footprint using the radiative-transfer model described below. These *measured* reflectivities were then compared to *modeled* reflectivities, computed with the physical reflectivity model for dielectric periodic surfaces outlined in Section 3.2. The soil-water content *wc* is taken into account through the relative permittivity ε of the soil, which is linked to *wc*. Section 3.3 presents the experimentally derived relationship between *wc* and ε for the sandy soil used in this study. The modeled reflectivities were later corrected for effects not considered in the physical reflectivity model using the simple empirical approach described in Section 3.4.

3.1 Radiative Transfer

The measured brightness temperatures T_B^p (p = H, V) are a composite of the radiances emitted from the soil box and from the surroundings. This is considered in the radiative-transfer model (1), which describes T_B^p as the linear combination of the soil-box radiance and the radiance of the surrounding paved area. These contribute with the fractional amounts μ^p and $\left(1-\mu^p\right)$, respectively. The corresponding reflectivities are the reflectivity R^p of the soil under test and the reflectivity R_0^p of the paving, whereas a uniform effective ground temperature T_{eff} is assumed for both areas. With $T_{\text{sky}} \approx 5$ K [26] being the sky brightness, this yields

$$T_B^p = \mu^p \left[(1-R^p)T_{\text{eff}} + R^p T_{\text{sky}} \right] + (1-\mu^p) \left[(1-R_0^p)T_{\text{eff}} + R_0^p T_{\text{sky}} \right]. \qquad (1)$$

This zero-order radiative-transfer model fulfills Kirchhoff's law. Furthermore, the terms $\left(1-R^p\right)$ and $\left(1-R_0^p\right)$ express the emissivities of the soil under test and the paved area, respectively, if thermodynamic equilibrium is assumed.

Similar to the parameterization proposed by [28], T_{eff} was estimated as the mean of the air temperature T_{air} and the ground temperature $T_{18\text{cm}}$. This approximation might deviate somewhat from the unknown true value of the effective ground temperature. However, it's temporal variation is assumed to be synchronous to that of the true T_{eff}. The reflectivities $R_0^H = 0.38$ and $R_0^V = 0.13$ of the paving were derived from $T_B^p = (1-R_0^p)T_{\text{eff}} + R_0^p T_{\text{sky}}$ measured before the soil box was placed in the radiometer footprint [25]. Values for μ^p were estimated from brightness temperatures $T_{B,\text{mesh}}^p$ measured for the soil box covered with a reflector (aluminum mesh with mesh size ≈ 2 mm). Inserting $T_{B,\text{mesh}}^p$ together with $R_{\text{mesh}}^p = 1$ and the previously determined R_0^p in (1), and solving for μ^p yielded $\mu^H = 0.71$ and $\mu^V = 0.81$. The difference
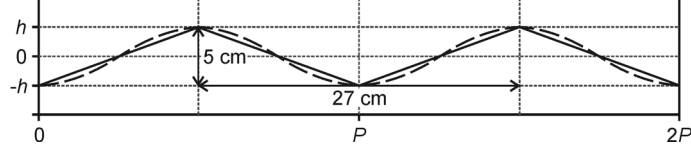
Fig. 2. Illustration of the cross section of the prepared furrows (solid line) and its mathematical representation in the reflectivity model (dashed line).

between μ^{H} and μ^{V} is attributed to the polarization-dependent reflectivity of the wooden board of the box facing the radiometer, which was not covered with the reflector during the $T_{\mathrm{B,mesh}}^{p}$ measurements.

With all quantities in (1) except for the soil reflectivity R^{p} known, R^{p} can be derived from the T_{B}^{p} measured with

$$R^{p} = \frac{T_{\mathrm{B}}^{p} - T_{\mathrm{eff}}}{\mu^{p}(T_{\mathrm{sky}} - T_{\mathrm{eff}})} + \left(1 - \frac{1}{\mu^{p}}\right)R_{0}^{p} . \tag{2}$$

3.2 Reflectivity of a Dielectric Periodic Surface

Models using full wave electromagnetism are required to simulate the interaction of electromagnetic waves with dielectric structures featuring spatial periodicities in the range of the observation wavelength. In contrast to models based on physical optics (short-wavelength approximation) or geometric optics (which ignore wave effects), the full-wave electromagnetic approaches seek solutions for Maxwell's equations at the dielectric boundaries. An extensive theoretical overview can be found in, e.g. [14] and [15].

To explain certain aspects of the signatures measured for the periodic soil surfaces described in Section 2, we implemented the reflectivity model presented in Chapter 3 of [15]. This physical model solves Maxwell's equations for the electric and the magnetic fields at a one-dimensional dielectric periodic surface using the extended boundary condition approach. This approach uses scalar functions for the surface fields, which are represented by their Fourier series expansion. The corresponding unknown Fourier coefficients are derived by solving the T-matrix equations (see [14], Chapter 2, Section 7).

To simplify the evaluation of the model, the surface was assumed to be represented by a sinusoidal function with amplitude h and periodicity P perpendicular to the direction of the furrows, as shown in Fig. 2 (the surface is invariant along the furrow direction). Furthermore, the relative permittivity of the soil was assumed to be constant with depth. In that case, closed-form expressions for the T-matrix elements exist and can be expressed by using Bessel functions. Once the surface fields (actually their Fourier coefficients) are known, the fields scattered in discrete upward directions (Floquet modes) are computed. Finally, the reflectivity R^{p} of the sinusoidal surface is derived as the ratio between the power reflected per surface period and the corresponding incident power. The power reflected is expressed by summing up the powers carried by the Floquet modes propagating in an upward direction. This approach allows R^{p} of our furrowed surface (approximated as one-dimensional sinusoidal surface with

amplitude h and period P) to be computed for arbitrary elevation and azimuth angles of the incident wave with respect to the furrow direction. The period and amplitude were set to $P = 27$ cm and $h = 2.5$ cm, respectively, resulting in a sine function with the same periodicity and amplitude as the prepared triangular furrows (Fig. 2). Another feasible assumption would have been to choose h such that the sinusoidal surface features the same root-mean-square height as the prepared furrowed surface ($h \approx 2.0$ cm). Both options yielded similar results, whereas the choice of $h = 2.5$ cm gave the best overall agreement of model results with observations.

Implementation of this mathematically quite complex reflectivity model was time-consuming and demanding. In order to forestall errors in the coding, the model was programmed independently in Mathematica, as well as in Matlab. Exemplary calculations yielded identical results for both implementations. To further validate the coding, the examples presented in [15] were recalculated and could be reproduced.

3.3 Soil Permittivity

The relation between the volumetric water content wc ($m^3 \cdot m^{-3}$) and the complex relative permittivity $\varepsilon = \varepsilon' + i\varepsilon''$ of the sandy soil used was determined experimentally. The resulting relation $\varepsilon(wc)$ was then used as input to the reflectivity model (Section 3.2) to compute R^p for the different soil topographies at the different soil moistures wc, whereas wc was assumed to be constant with depth.

To derive $\varepsilon(wc)$, first, soil samples with wc between 0 $m^3 \cdot m^{-3}$ (oven dry) and 0.2 $m^3 \cdot m^{-3}$ (almost water saturated) were prepared. The corresponding ε was then measured at room temperature (23 °C) with a network analyzer (Hewlett Packard 8753 ES) and an attached coaxial chamber (diameter of the outer conductor: 60 mm, diameter of the inner conductor: 26 mm, length: 200 mm, volume ≈470 cm^3) containing the respective soil sample. The frequency range measured was 0.1−2 GHz. In analogy to the empirical relation proposed in [29], a third-order polynomial equation was fitted to the real and imaginary parts of ε measured for 1.4 GHz

$$\varepsilon' = 671.2wc^3 + 173.9wc^2 + 4.5wc + 2.66$$
$$\varepsilon'' = 603.2wc^3 - 88.9wc^2 + 8.2wc + 0.03. \tag{3}$$

Figure 3 shows the measured relationship $\varepsilon(wc)$, together with (3) and the empirical relation of [29]. It is apparent, that the latter yields only poor results for the soil under test, whereas (3) fits the observations well. For the range $0 \, m^3 \cdot m^{-3} < wc < 0.1 \, m^3 \cdot m^{-3}$ observed during the radiometer measurements, the errors of the relations (3) are ≤ 0.23 for ε' and ≤ 0.05 for ε''. It is furthermore assumed that using the soil-specific relation (3) yields more accurate results than applying semi-empirical dielectric mixing models, such as [30] or [31].

3.4 Correction for Heterogeneities Affecting Soil Reflectivity

The soil reflectivity can be affected by a number of additional factors besides the furrows, which are not accounted for in the reflectivity model outlined in Section 3.2. On the one hand,
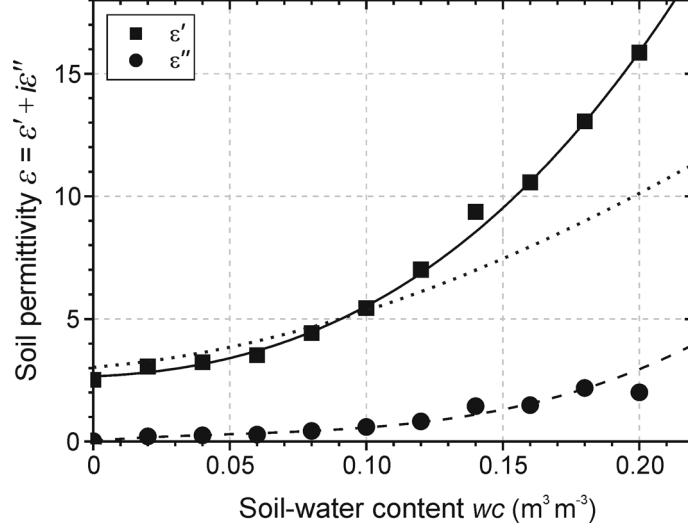
Fig. 3. Measured relationship between relative soil permittivity $\varepsilon = \varepsilon' + i\varepsilon''$ and soil-water content wc (solid symbols). The solid and dashed lines are the empirical best-fit equations (3). For comparison, the empirical relation [29] is also shown (dotted line).

small-scale surface roughness is superimposed on the prepared surfaces, and the top soil layer is expected to exhibit a certain heterogeneity due to the manipulation of the soil surface and due to drying in the course of the measurements. On the other hand, soil moisture (and thus soil permittivity) is assumed to be constant with depth in the reflectivity model, whereas in reality the soil moisture increased with depth. Other factors are uncertainties in the effective soil temperature T_{eff} and the deviation of the real cross section of the furrows from its mathematical representation in the reflectivity model (Fig. 2). Not least, it has to be noted that both the reflectivity model as well as the radiative-transfer approach (1) are based on the assumption of a fixed observation angle $\theta = 50°$ for the entire observed scene, whereas in reality the observed soil box covered local view angles ranging from approximately 40° to 60° as seen from the center of the antenna aperture.

As these factors cannot be quantified (measured) exactly and since our study focuses on the influence of the surface topography on soil reflectivity, we applied a very simple empirical approach to account for these effects

$$R^{p*} = R^p \exp\left(-h^p\right). \tag{4}$$

That means that (uncorrected) reflectivities R^p (p = H, V) were multiplied with an exponential correction function, yielding modified values R^{p*} corrected for the combination of the effects mentioned above. This single parameter correction can be seen as a simplified form of the roughness model proposed in [32]. It results from [32], when polarization mixing is assumed to be negligible, which is common practice when correcting passive L-band signatures for small-scale roughness [9], [33]. However, it is important to note that the model [32], and even more the relation (4), are empirical in nature, and therefore no clear physical meaning should be associated with the empirical h^p parameter used in (4). Furthermore, h^p can be

distinctly different for horizontal and vertical polarization as the result of dielectric anisotropy in the air-to-soil transition zone [34], [35].

The values of h^p were obtained by minimizing the cost function $CF(h^p)$ representing the sum of the squared differences between the modified R^{p*} and the corresponding observations R^p

$$CF(h^p) = \sum (R^{p*} - R^p)^2. \tag{5}$$

This approach simply adapts model results to observations empirically. This yields rather good results when applied in addition to the physical reflectivity model, as will be shown in Section 4.3.

4 Results and Discussion

In Section 4.1, we present the results of the measurements and the model simulations. The impact of the furrows on the measured and modeled soil reflectivity is further discussed in Section 4.2 on the basis of the relative reflectivity changes (relative to the plane surface reflectivity) caused by the furrows. Since both sections focus on the influence of the surface topography on the soil reflectivity, only the (uncorrected) simulations performed with the physical reflectivity model (Section 3.2) are considered. Modeled reflectivities, corrected with the approach introduced above, are shown in Section 4.3, where the model performance is discussed.

4.1 Reflectivities

Figure 4 shows the results of the measurements (solid symbols) and the model simulations (empty symbols). The measured and modeled reflectivities R^p at horizontal (squares) and vertical polarization (circles) are shown for the different soil topographies and soil moisture conditions investigated. Panel a) shows the results for dry soil, and panel b) shows those for moist soil.

The measured R^p were derived from measured brightness temperatures T_B^p using (2). The mean values of the 20 measurements performed for each surface type are given. Since the associated standard deviations were very small (≤ 0.003) in all cases, no uncertainty ranges are shown. The modeled R^p for the different surface topographies and soil moistures were computed with the physical reflectivity model. The necessary soil permittivity $\varepsilon(wc)$ was determined from the measured near-surface soil-water content wc using (3). The error bars in panel b) represent the range of R^p resulting from using the highest and lowest value of the ten wc observations made during the moist-soil measurements. This illustrates the uncertainty in R^p modeled due to the temporal and spatial variation of wc observed on that day. No error bars are shown in panel a) since wc of the soil-surface layer was constant throughout the dry-soil measurements.
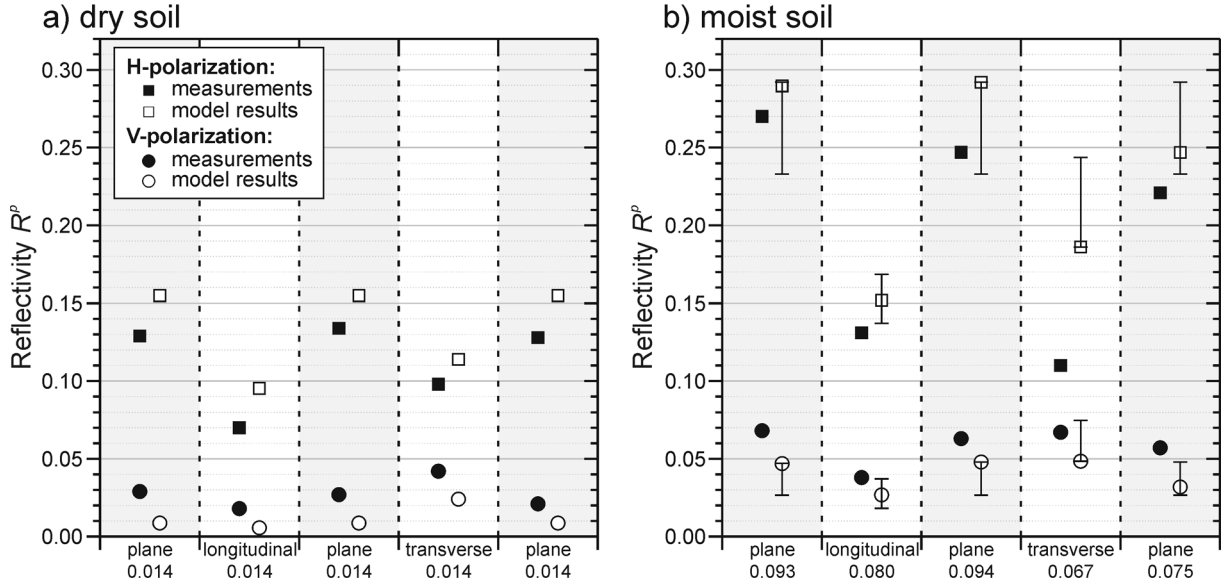
Fig. 4. Measured (solid symbols) and modeled (empty symbols) reflectivities R^p (p = H, V) of the different surfaces at horizontal (squares) and vertical polarization (circles). The abscissae labels indicate the different surface topographies (plane surface, longitudinal furrows, transverse furrows) and the corresponding *in situ* measured soil-water contents wc $(\mathrm{m^3 \cdot m^{-3}})$. Panel a) is for dry soil, and panel b) is for moist soil. Plane surface measurements are highlighted in gray for the sake of clarity.

4.1.1 Dry-Soil Measurements (Fig. 4a)

All three measurements of the plane dry-soil surface at p = H yielded $R^H \approx 0.13$. With longitudinal furrows, R^H decreased almost by half with respect to the plane surface to $R^H \approx 0.07$. Transverse furrows also decreased the reflectivity of the soil surface significantly ($R^H \approx 0.1$) but not as much as the longitudinal furrows. The measurements of the plane surface at p = V yielded values $0.02 \leq R^V \leq 0.03$. Longitudinal furrows ($R^V \approx 0.02$) slightly decreased R^V with respect to the plane surface reflectivity, whereas transverse furrows ($R^V \approx 0.04$) slightly increased R^V. The generally low values of R^V are due to the fact that the observation angle $\theta = 50°$ was only slightly below the Brewster angle, which is $\theta_B = \arctan \sqrt{|\varepsilon|} \approx 59°$ for the observed $wc = 0.014 \ \mathrm{m^3 \cdot m^{-3}}$.

The modeled reflectivities at p = H showed the same pattern as the measured reflectivities: R^H modeled for the plane surfaces was higher than R^H computed for the surface with transverse furrows, which in turn exceeded R^H computed for the surface with longitudinal furrows. For all surfaces, however, the modeled R^H overestimated measurements by 0.02 to 0.03. At V-polarization, the modeled R^V also deviated from measurements, while still showing the same sequence with different topographies as the measured R^V. In this case, however, measurements were underestimated by the model by 0.01 to 0.02.

4.1.2 Moist-Soil Measurements (Fig. 4b)

The reflectivities R^p measured for the plane moist-soil surfaces decreased in the course of the day from 0.27 to 0.22 at p = H and from 0.07 to 0.06 at p = V. The decrease is attributed to the drying of the soil surface due to solar radiation and wind. Drying was observed visibly,

especially during the last two measurements (transverse furrows and plane surface), and was also partially noticeable in the *wc* measured. However, the reflectivity decrease associated with surface drying was quite small in comparison with the influence of the furrows. At H-polarization, the R^{H} of both furrowed surfaces was substantially lower than the R^{H} measured for the plane surface ($R^{\mathrm{H}} \approx 0.13$ for longitudinal furrows, $R^{\mathrm{H}} \approx 0.11$ for transverse furrows). At V-polarization, in contrast, longitudinal furrows led to smaller ($R^{\mathrm{V}} \approx 0.04$) and transverse furrows to slightly larger reflectivity ($R^{\mathrm{V}} \approx 0.07$) compared to the adjacent measurements of the plane surface.

The modeled R^p values displayed the same pattern as the measurements, but they generally over- ($p = \mathrm{H}$) or underestimated ($p = \mathrm{V}$) the measured R^p, respectively, similar to what was observed for the dry-soil surface. The deviations between model results and measurements were in the same range as for the dry soil (0.02–0.04 for $p = \mathrm{H}$, 0.01–0.02 for $p = \mathrm{V}$), except for the R^{H} of the moist-soil surface with transverse furrows. Here, an exceptionally high deviation (0.08) between the measured and modeled R^{H} was observed (whereas the value measured for the moist-soil surface was only marginally larger than the corresponding R^{H} measured for the dry-soil surface). Generally, however, it can be stated, that moist furrows affected R^p similarly to dry ones, whereas the R^p of all moist surfaces were higher than the R^p of the corresponding dry-soil surfaces.

4.2 Relative Reflectivity Changes

The relatively constant offsets that we observed between the measured and the modeled reflectivity values are mainly attributed to a combination of the different effects mentioned in Section 3.4. One important factor is that the reflectivity model does not take into account small-scale surface roughness, which is in reality superimposed on the prepared surfaces, as well as small-scale heterogeneity of the top soil layer caused by the manipulation of the surface. Another cause for the discrepancies observed might be the assumption in the reflectivity model that soil moisture is constant with depth. Simulations, performed with a coherent radiative-transfer model for layered dielectric media [36] for hypothetical soil moisture profiles, indicated that the observed discrepancies could to some degree be errors introduced through this assumption. However, this effect cannot be quantified accurately since the exact soil moisture profile is not known.

Given the observed deviations, it seems expedient to refer to the relative reflectivity changes δR^p, which were caused by the furrows (in comparison to the plane surface reflectivities), when discussing the effects of the furrows on the soil reflectivity

$$\delta R^p \equiv \left(R^p_{\mathrm{furrow}} - R^p_{\mathrm{plane}} \right) \big/ R^p_{\mathrm{plane}} \,. \tag{6}$$

This definition of δR^p (where $p = \mathrm{H}$, V as before) is the relative difference between the reflectivity R^p_{furrow} of a furrowed surface and the reflectivity R^p_{plane} of the corresponding plane surface. Consequently, the ratio (6) is much less vulnerable to the effects discussed above,

a) horizontal polarization
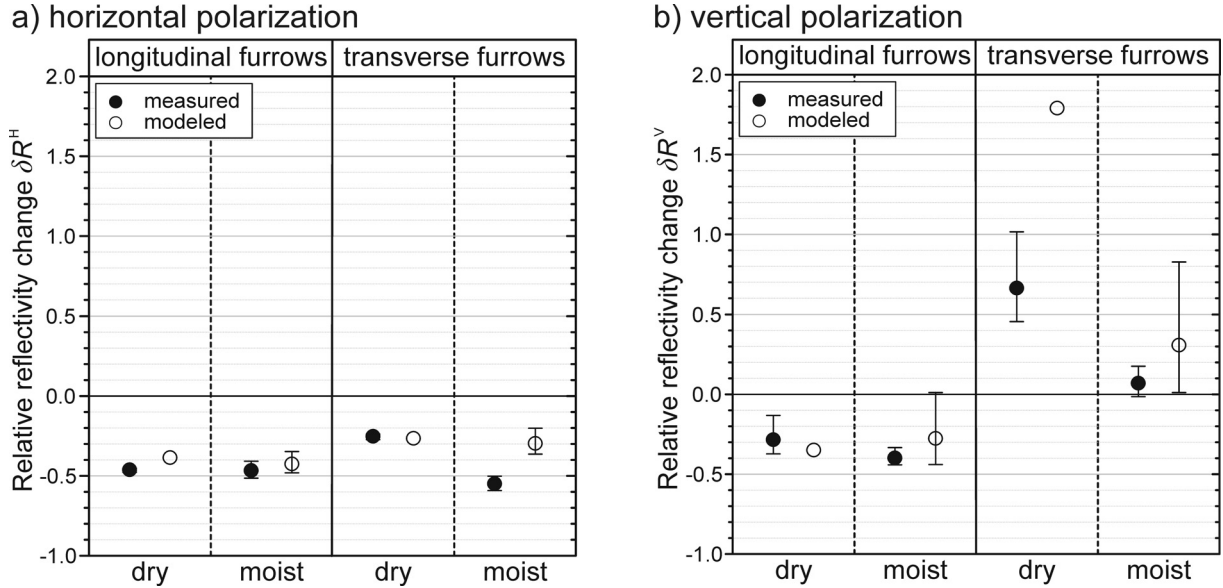

b) vertical polarization

Fig. 5. Relative reflectivity changes δR^p (p = H, V) caused by the furrows under dry- and moist-soil conditions at a) horizontal and b) vertical polarization. δR^p due to longitudinal furrows are shown in the left half of each panel, and δR^p due to transverse furrows are shown in the right half. Solid symbols are δR^p calculated from the reflectivities measured, and empty symbols are δR^p calculated from the reflectivities modeled; both of which are shown in Fig. 4.

and additionally the influences of errors introduced through the assumption of a fixed observation angle and of uncertainties in the effective soil temperature T_{eff} are strongly reduced. Therefore, it can be expected that the values of δR^p derived from the modeled and measured R^p are directly comparable, and thus suitable for analyzing the effects of the furrows on soil reflectivity.

Figure 5 shows δR^p calculated with (6) from the reflectivities presented in Fig. 4. Solid symbols refer to δR^p calculated from measured reflectivities (using the mean R^p_{plane} of the dry- and moist-soil measurements) together with the corresponding uncertainty ranges due to the decrease in R^p_{plane} in the course of the respective day. Empty symbols refer to δR^p derived from the modeled reflectivities (Section 3.2). The soil permittivity ε used as input to the reflectivity model was computed from the *in situ* soil-water content *wc* using (3). In doing so, R^p_{furrow} were modeled with the *wc* observed during the respective brightness temperature measurements, and R^p_{plane} were calculated either with the mean *wc* (symbols) or with the highest and lowest *wc* of the day of measurements (error bars).

Furrows reduced reflectivities at horizontal polarization substantially (Fig. 5a). This is illustrated by the fact that $\delta R^H < 0$ under both dry and moist conditions and for both furrow directions. The modeled and measured δR^H caused by the longitudinal furrows (left panel) were in the range of $-0.47 \leq \delta R^H \leq -0.39$. That means that longitudinal furrows reduced the reflectivity of the soil surface by almost half compared to R^H_{plane}, whereas no significant differences between dry- and moist-soil conditions were observed. The reflectivity decrease caused by the

transverse furrows (right panel) was somewhat smaller. For dry soil, the measurements and model results both yielded $\delta R^{\mathrm{H}} \approx -0.25$, i.e. $R^{\mathrm{H}}_{\mathrm{furrow}}$ was reduced by $\approx 25\%$ compared to $R^{\mathrm{H}}_{\mathrm{plane}}$. For the moist-soil surface, the δR^{H} measured and modeled deviate from each other. The model predicted approximately the same value as for dry soil ($\delta R^{\mathrm{H}} \approx -0.3$), whereas the value measured dropped to $\delta R^{\mathrm{H}} \approx -0.55$. This is a consequence of the discrepancy of 0.08 between the measured and modeled R^{H} for the moist-soil surface with transverse furrows (see Fig. 4). The strikingly low value for R^{H} measured cannot be explained conclusively. However, it is assumed that this was not solely caused by the transverse furrows but rather is a combination of different effects. Possibly, the drying of the uppermost soil layer observed during the day led to a dielectric profile with distinct layering causing coherent effects, which in turn affected R^{H}. Furthermore, an agglomeration of soil particles near the surface was observed in the course of the day, which may also have influenced measurements. For these reasons, the R^{H} measured for the moist-soil surface with transverse furrows will be excluded from the further analysis described in Section 4.3.

At vertical polarization (Fig. 5b), the relative reflectivity changes δR^{V} caused by the furrows show a more diverse pattern. The measured and modeled δR^{V} for longitudinal furrows (left panel) are in the range $-0.39 \le \delta R^{\mathrm{V}} \le -0.28$, and it is not possible to detect a clear correlation with soil moisture wc. The measurements suggest that δR^{V} decreases slightly with increasing wc, whereas the model indicates a small increase. In contrast, the δR^{V} caused by the transverse furrows (right panel) is strongly dependent on wc. Changing the surface topography from plane to transverse furrows caused the measured reflectivities to increase substantially when the soil surface was dry ($\delta R^{\mathrm{V}} \approx 0.66$), but only a small change was observed under moist conditions ($\delta R^{\mathrm{V}} \approx 0.07$). The corresponding modeled reflectivities show the same trend with soil moisture, whereas the magnitude of the δR^{V} was significantly higher for dry soil ($\delta R^{\mathrm{V}} \approx 1.79$) and somewhat larger for moist soil ($\delta R^{\mathrm{V}} \approx 0.31$). It is striking that both the modeled and the measured δR^{V} for transverse furrows were > 0, and that they were larger for dry than for moist soil even when the uncertainties of δR^{V}, arising from the uncertainties in wc, are considered. It allows drawing the conclusion that reflectivities at vertical polarization may be increased as a result of polarization crosstalk effects, which can change a horizontally or vertically polarized electromagnetic wave into an elliptically polarized wave. Similar effects are also predicted by the integral equation model (IEM) [37] when used to compute reflectivities of random rough surfaces. For dry soil, this effect is even greater, as the emission depth increases, which promotes volume scattering and hence leads to a depolarization of the radiance.

The overestimation of δR^{V} by the model can partly be explained by uncertainties in the observation angle θ. For experimental reasons, the main direction of the antenna can differ somewhat from the aspired value $\theta = 50°$ that was used in the reflectivity model. Furthermore, the local observation angles are slightly different from θ for regions on the soil surface, which are not exactly at the intersection with the antenna's main direction. Varying θ by $\pm 3°$ when calculating δR^{p} resulted in significant changes of δR^{V} due to transverse furrows under dry ($0.95 \le \delta R^{\mathrm{V}} \le 4.11$) and moist-soil conditions ($0.12 \le \delta R^{\mathrm{V}} \le 0.64$), whereas for all other cases

investigated, the resulting uncertainties in δR^p were ≤ 0.1. Furthermore, the overestimation of δR^V due to the transverse furrows by the model can also be an indication that polarization crosstalk is overrated by the reflectivity model we used. Similar discrepancies were observed in [34] when calculating rough-surface reflectivities with the IEM [37].

4.3 Model Performance

As we have shown previously, the physical reflectivity model was able to reproduce the observed dependence of soil reflectivity on furrow orientation and soil moisture reasonably well. However, when the measured and modeled reflectivities R^p (p = H, V) were compared directly, rather than comparing the relative reflectivity changes δR^p, the modeled values differed from the observations. These deviations are ascribed mainly to the small-scale surface roughness superimposed on the furrows and the heterogeneity of the soil surface layer due to drying and the manipulation of the soil surface. Additional sources of error are the assumption of a fixed observation angle and a constant soil moisture profile with soil depth, as well as our approximation for the effective ground temperature. To further improve the agreement between measurements and simulations, we used the empirical approach described in Section 3.4. Thereby, the reflectivities calculated with the physical reflectivity model were adapted to observations with (4) using the parameter values $h^H = 0.137$ and $h^V = -0.399$. These values for h^p for the best agreement between the measurements and the model results were found by minimizing the cost function (5).

To illustrate the model performance, a scatter plot with the measured and modeled reflectivities for three different model levels i is shown in Fig. 6. The measured reflectivities R^p (plotted along the X-axis) are identical to the reflectivities indicated by the solid symbols in Fig. 4. They are opposed to the modeled reflectivities R_i^p (i = 1, 2, 3) (plotted along the Y-axis), which are as follows:

1) R_1^p were simply modeled with the Fresnel equations regardless of whether the surface was plane or furrowed. The corresponding tuples (R^p, R_1^p) are shown as triangles in Fig. 6.

2) R_2^p were calculated with the reflectivity model for periodic surfaces described in Section 3.2. The model distinguishes between the different soil topographies: plane surface, longitudinal furrows, and transverse furrows. R_2^p are identical to the modeled reflectivities presented in Fig. 4. The corresponding tuples (R^p, R_2^p) are shown as circles in Fig. 6.

3) R_3^p are reflectivities derived from R_2^p using the empirical correction described in Section 3.4. The corresponding tuples (R^p, R_3^p) are shown as squares in Fig. 6.

As expected, using the Fresnel equations results in a poor agreement between measurements R^p and model simulations R_1^p (triangles). The root-mean-square differences (residua) between R^p and R_1^p are 0.0549 for p = H and 0.0176 for p = V (Table I). The large residua are mainly caused by the considerable discrepancies between the reflectivities measured for the furrowed surfaces and those modeled (solid triangles).
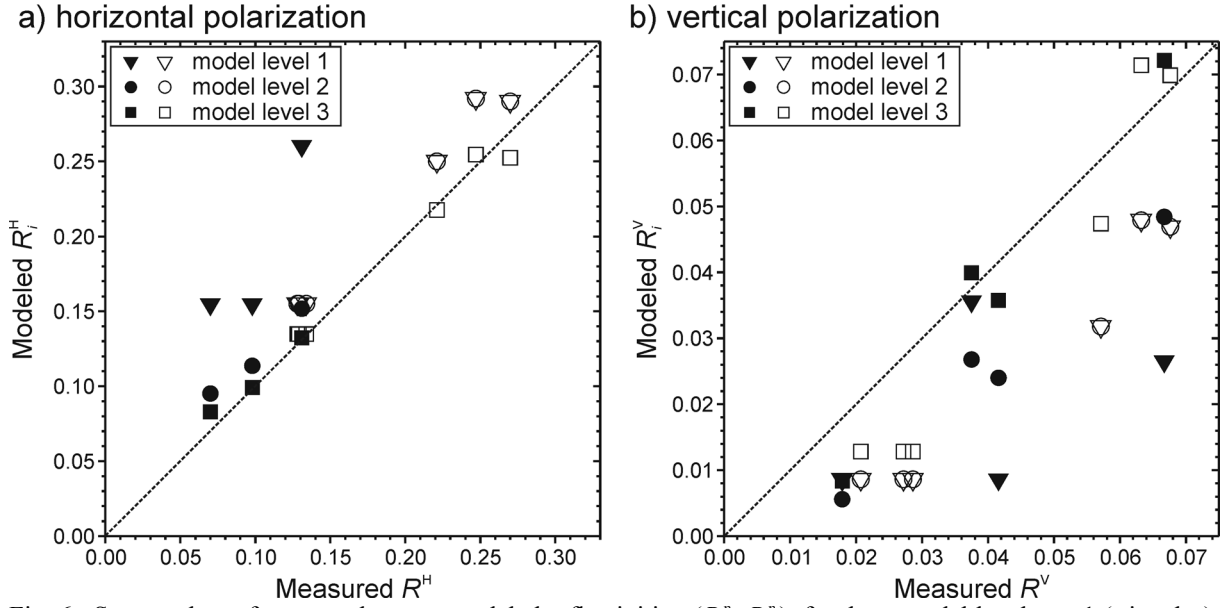
a) horizontal polarization   b) vertical polarization

Fig. 6. Scatter plots of measured versus modeled reflectivities (R^p, R_i^p) for three model levels $i = 1$ (triangles), 2 (circles), and 3 (squares) for a) horizontal and b) vertical polarization (see text for the explanation of the different model levels). Empty symbols are for plane surfaces. Solid symbols are for furrowed surfaces. The dashed line is the 1:1 line.

Using the reflectivity model for periodic surfaces yields, for the plane surfaces, the same reflectivities $R_2^p = R_1^p$ as the calculations with the Fresnel equations (empty circles). For the furrowed surfaces (solid circles), however, R_2^p deviate considerably from R_1^p resulting in a much better agreement between the measurements and simulations. This manifests itself in the considerably reduced residua of 0.0089 for $p = $ H and 0.0056 for $p = $ V (Table I). However, at horizontal polarization, the modeled reflectivity still overestimates the measurements $(R_2^H > R^H)$, while, at vertical polarization, the model underestimates the observations $(R_2^V < R^V)$.

Using the correction presented in Section 3.4 results in a further improvement of the model performance (squares). At $p = $ H, the modeled R_3^H values are in very good agreement with the measured R^H, resulting in a residuum of 0.0028. At $p = $ V, the improvement was not as striking, but here as well the resulting data tuples (R^V, R_3^V) were moved toward the 1:1 line, and the residuum was further reduced to 0.0029.

5 Conclusions

We found that furrows had a distinct impact on the observed soil reflectivities at both polarizations and for both furrow directions investigated. At horizontal polarization, furrows generally reduced the reflectivity $(\delta R^H < 0)$. The relative change δR^H with respect to the plane surface reflectivity was more pronounced for longitudinal than for transverse furrows, and no significant dependence of δR^H on soil moisture was observed. At vertical polarization, the re-

Table I. Root-mean-square differences (residua) between the measured R^p and modeled R_i^p for the three different model levels i = 1, 2, 3 shown in Fig. 6.

model level i		residua	
		p = H	p = V
1	Fresnel equations	0.0549	0.0176
2	reflectivity model (Section 3.2)	0.0089	0.0056
3	reflectivity model + empirical correction	0.0028	0.0029

flectivity of the soil was reduced by the longitudinal furrows ($\delta R^V < 0$) with no clear dependence of δR^V on soil moisture. In contrast to that, transverse furrows led to an increase in the soil reflectivity ($\delta R^V > 0$), which, however, showed a strong dependence on soil moisture. These results demonstrate the importance of considering the adequate soil topography when retrieving geophysical parameters from L-band signatures emitted from a furrowed soil surface.

The model simulations performed illustrate that this can be achieved by choosing an appropriate reflectivity model. When reflectivities were computed with the physical reflectivity model that takes into account the periodic soil topography, the residua between the measured and modeled reflectivities were reduced by a factor of ≈6 (p = H) and ≈3 (p = V), respectively, in comparison with the residua obtained by using the Fresnel equations (Table I). The agreement between the measured and modeled reflectivities was further improved by additionally applying a simple empirical correction to account for the small-scale heterogeneity of the top soil layer. This reduced the residua again by a factor of ≈3 (p = H) and ≈2 (p = V), respectively (Table I).

The knowledge gained in this study is useful for estimating the implications of periodic soil topography with dimensions in the range of the observation wavelength on soil moisture retrievals, e.g. from SMOS or airborne radiometer measurements over agricultural areas. In addition, the findings can be used to identify such particular surface patterns on the basis of the brightness temperatures measured.

Acknowledgement

References

[1] T. Schmugge, "Remote sensing of soil moisture," in *Encyclopedia of Hydrological Forecasting*, M. G. Anderson and T. Burt, Eds. New York: Wiley, 1985, pp. 101-124.

[2] A. M. Shutko, "Microwave radiometry of lands under natural and artificial moistening," *IEEE Trans. Geosci. Remote Sens.*, vol. GE-20, no. 1, pp. 18-26, 1982.

[3] Y. H. Kerr, P. Waldteufel, J. P. Wigneron, S. Delwart, F. Cabot, J. Boutin, M. J. Escorihuela, J. Font, N. Reul, C. Gruhier, S. E. Juglea, M. R. Drinkwater, A. Hahne, M. Martin-Neira, and S. Mecklenburg, "The SMOS Mission: New tool for monitoring key elements of the global water cycle," *Proc. IEEE*, vol. 98, no. 5, pp. 666-687, 2010.

[4] J.-P. Wigneron, Y. H. Kerr, P. Waldteufel, K. Saleh, M.-J. Escorihuela, P. Richaume, P. Ferrazzoli, P. d. Rosnay, G. R., J.-C. Calvet, J. P. Grant, M. Guglielmetti, B. Hornbuckle, C. Mätzler, T. Pellarin, and M. Schwank, "L-band Microwave Emission of the Biosphere (L-MEB) model: Description and calibration against experimental data sets over crop fields," *Remote Sens. Environ.*, vol. 107, no. 4, pp. 639-655, 2007.

[5] K. Saleh, Y. H. Kerr, G. Boulet, P. Maisongrande, P. d. Rosnay, D. Floricioiu, M. J. Escorihuela, J.-P. Wigneron, A. Cano, E. López-Baeza, J. P. Grant, J. Balling, N. Skou, M. Berger, S. Delwart, P. Wursteisen, P. Panciera, and J. P. Walker, "The CoSMOS L-band experiment in Southeast Australia," in *Proc. IGARSS*, Barcelona, Spain, 2007, pp. 3948-3951.

[6] B. J. Choudhury, T. J. Schmugge, A. Chang, and R. W. Newton, "Effect of surface roughness on the microwave emission from soil," *J. Geophys. Res.*, vol. 84, no. C9, pp. 5699-5706, 1979.

[7] M. J. Escorihuela, Y. H. Kerr, P. de Rosnay, J.-P. Wigneron, J.-C. Calvet, and F. Lemaître, "A simple model of the bare soil microwave emission at L-band," *IEEE Trans. Geosci. Remote Sens.*, vol. 45, no. 7, pp. 1978-1987, 2007.

[8] T. Mo and T. J. Schmugge, "A Parameterization of the effect of surface roughness on microwave emission," *IEEE Trans. Geosci. Remote Sens.*, vol. GE-25, no. 4, pp. 481-486, 1987.

[9] J.-P. Wigneron, L. Laguerre, and Y. H. Kerr, "A simple parameterization of the L-band microwave emission from rough agricultural soils," *IEEE Trans. Geosci. Remote Sens.*, vol. 39, no. 8, pp. 1697-1707, 2001.

[10] S. Paloscia, P. Pampaloni, L. Chiarantini, S. Coppo, S. Gagliani, and G. Luzi, "Multifrequency passive microwave remote sensing of soil moisture and roughness," *Int. J. Remote Sensing*, vol. 14, no. 3, pp. 467-483, 1993.

[11] J. R. Wang, R. W. Newton, and J. W. Rouse, "Passive microwave remote sensing of soil moisture: The effect of tilled row structure," *IEEE Trans. Geosci. Remote Sens.*, vol. GE-18, no. 4, pp. 296-302, 1980.

[12] X. Yin, Y. Liu, and H. Zhang, "Removing the impact of wind direction on remote sensing of sea surface salinity," *Chin. Sci. Bull.*, vol. 51, no. 11, pp. 1368-1373, 2006.

[13] O. Isoguchi and M. Shimada, "Preliminary study on developing an L-band wind retrieval model function using ALOS/PALSAR," presented at the Envisat Symp., Montreux, Switzerland, 2007.

[14] L. Tsang, J. A. Kong, and K.-H. Ding, *Scattering of Electromagnetic Waves: Theories and Applications*, vol. I. New York: Wiley, 2000.

[15] L. Tsang, J. A. Kong, K.-H. Ding, and C. O. Ao, *Scattering of Electromagnetic Waves: Numerical Simulations*, vol. II. New York: Wiley, 2001.

[16] C. Mätzler, D. Weber, M. Wüthrich, K. Schneeberger, C. Stamm, and H. Flühler, "ELBARA, the ETH L-band radiometer for soil moisture research," in *Proc. IGARSS*, Toulouse, France, 2003, pp. 3058-3060.

[17] W. Gerwin, W. Schaaf, D. Biemelt, A. Fischer, S. Winter, and R. F. Hüttl, "The

artificial catchment "Chicken Creek" (Lusatia, Germany) - A landscape laboratory for interdisciplinary studies of initial ecosystem development," *Ecological Engineering*, vol. 35, no. 12, pp. 1786-1796, 2009.

[18] H. M. Picket, J. C. Hardy, and F. Jam, "Characterization of a dual-mode horn for submillimeter wavelengths," *IEEE Trans. Microw. Theory Tech.*, vol. MTT-32, no. 8, pp. 936-937, 1984.

[19] M. Guglielmetti, M. Schwank, C. Mätzler, C. Oberdörster, J. Vanderborght, and H. Flühler, "FOSMEX: Forest soil moisture experiments with microwave radiometry," *IEEE Trans. Geosci. Remote Sens.*, vol. 46, no. 3, pp. 727-735, 2008.

[20] M. Guglielmetti, M. Schwank, C. Mätzler, C. Oberdörster, J. Vanderborght, and H. Flühler, "Measured microwave radiative transfer properties of a deciduous forest canopy," *Remote Sens. Environ.*, vol. 109, no. 4, pp. 523-532, 2007.

[21] K. Schneeberger, M. Schwank, C. Stamm, P. d. Rosnay, C. Mätzler, and H. Flühler, "Topsoil structure influencing soil water retrieval by microwave radiometry," *Vadose Zone J.*, vol. 3, no. 4, pp. 1169-1179, 2004.

[22] M. Schwank, M. Guglielmetti, C. Mätzler, and H. Flühler, "Testing a new model for the L-band radiation of moist leaf litter," *IEEE Trans. Geosci. Remote Sens.*, vol. 46, no. 7, pp. 1982-1994, 2008.

[23] M. Schwank and C. Mätzler, "L-band radiometer measurements of soil water under growing clover grass," *IEEE Trans. Geosci. Remote Sens.*, vol. 43, no. 10, pp. 2225-2237, 2005.

[24] M. Schwank, M. Stähli, H. Wydler, L. Jörg, C. Mätzler, and H. Flühler, "Microwave L-band emission of freezing soil," *IEEE Trans. Geosci. Remote Sens.*, vol. 42, no. 6, pp. 1252-1261, 2004.

[25] I. Völksch, M. Schwank, and C. Mätzler, "L-band reflectivity of a wire grid above a dielectric surface," *IEEE Geosci. Remote Sens. Lett.*, vol. 7, no. 3, pp. 601-605, 2010.

[26] T. Pellarin, J.-P. Wigneron, J.-C. Calvet, M. Berger, H. Douville, P. Ferrazzoli, Y. H. Kerr, E. Lopez-Baeza, J. Pulliainen, L. P. Simmonds, and P. Waldteufel, "Two-year global simulation of L-band brightness temperatures over land," *IEEE Trans. Geosci. Remote Sens.*, vol. 41, no. 9, pp. 2135-2139, 2003.

[27] M. Schwank, A. Wiesmann, C. Werner, C. Mätzler, D. Weber, A. Murk, I. Völksch, and U. Wegmüller, "ELBARA II, an L-band radiometer system for soil moisture research," *Sensors*, vol. 10, no. 1, pp. 584-612, 2010.

[28] B. J. Choudhury, T. Schmugge, and T. Mo, "A parameterization of effective soil temperature for microwave emission," *J. Geophys. Res.*, vol. 87, no. C2, pp. 1301-1304, 1982.

[29] G. C. Topp, J. L. Davis, and A. P. Annan, "Electromagnetic determination of soil water content: Measurements in coaxial transmission lines," *Water Resour. Res.*, vol. 16, no. 3, pp. 574-582, 1980.

[30] M. C. Dobson, F. T. Ulaby, M. T. Hallikainen, and M. A. El-Rayes, "Microwave dielectric behaviour of wet soil: Part II - Dielectric mixing models," *IEEE Trans. Geosci. Remote Sens.*, vol. 23, no. 1, pp. 35-44, 1985.

[31] V. L. Mironov, L. G. Kosolapova, and S. V. Fomin, "Physically and mineralogically based spectroscopic dielectric model for moist soils," *IEEE Trans. Geosci. Remote Sens.*, vol. 47, no. 7, pp. 2059-2070, 2009.

[32] J. R. Wang and B. J. Choudhury, "Remote sensing of soil moisture content over bare field at 1.4 GHz frequency," *J. Geophys. Res.*, vol. 86, no. C6, pp. 5277-5282, 1981.

[33] E. G. Njoku, T. J. Jackson, V. Lakshmi, T. K. Chan, and S. V. Nghiem, "Soil moisture retrieval from AMSR-E," *IEEE Trans. Geosci. Remote Sens.*, vol. 41, no. 2, pp. 215-229, 2003.

[34] M. Schwank, I. Völksch, J.-P. Wigneron, Y. H. Kerr, A. Mialon, P. d. Rosnay, and C. Mätzler, "Comparison of two bare-soil reflectivity models and validation with L-band radiometer measurements," *IEEE Trans. Geosci. Remote Sensing*, vol. 48, no. 1, pp. 325-337, 2010.

[35] J. Shi, K. S. Chen, Q. Li, T. Jackson, P. E. O'Neill, and L. Tsang, "A parameterized surface reflectivity model and estimation of bare-surface soil moisture with L-band radiometer," *IEEE Trans. Geosci. Remote Sensing*, vol. 40, no. 12, pp. 2674-2686, 2002.

[36] J. A. Dobrowolski, "Chapter 42: Optical Properties of Films and Coatings," in *Handbook of Optics*, vol. I, M. Bass, E. W. v. Stryland, D. R. Wiliams, and W. L. Wolfe, Eds. New York: McGraw-Hill, 1995, pp. 42.1-42.130.

[37] A. K. Fung, *Microwave Scattering and Emission Models and Their Application*. Boston, MA: Artech House, 1994.

Chapter IV

Monitoring the Brightness Temperature at 1.4 GHz of a Recently Renaturated Soil Surface

with Mike Schwank, Manfred Stähli, Stefan Seifert, and Christian Mätzler

Abstract—In a combined experimental and model study, we investigated the thermal L-band signatures of a sandy soil, especially focusing on the impact of the surface relief on the microwave emission. The ETH L-band radiometer ELBARA was installed in a recently renaturated, former lignite-mining area in Northern Germany, and brightness temperatures of two adjacent footprint areas were measured quasi-simultaneously for 1.5 years. The first footprint observed featured a distinct relief pattern in the form of three erosion gullies with steep and differently orientated slopes, whereas the surface of the second footprint was smooth. In addition to the brightness temperature measurements, auxiliary hydrometeorological variables and *in situ* soil moisture and temperature were measured, and digital elevation models of the two scenes were derived from terrestrial laser scanning. Brightness temperatures of the two footprints were simulated based on the *in situ* data and the digital elevation models, using a facet model that takes into account the topography of the observed surfaces, locally varying soil permittivity, as well as the directivity pattern of the ELBARA antenna. Radiometric measurements and simulated brightness temperatures were analyzed and compared with each other.

We found that brightness temperatures of the soil surface with the distinct relief pattern were increased at horizontal polarization and decreased at vertical polarization with respect to those of the plane surface. The simulations showed that this behavior is mainly an effect of the modification of the local observation angles and of polarization mixing, caused by the pronounced surface relief of this footprint. The comparison of the measurement results for the two areas furthermore revealed that the brightness temperatures of both areas react differently to changing meteorological conditions. That means, the observed difference between the brightness temperatures of the two footprints changes with time. This was only partly reproduced in the simulations, indicating different hydrological properties of both areas.

Index terms— Microwave radiometry, relief, topography, soil moisture.

1 Introduction

Within the last decades, microwave radiometry at L Band (1–2 GHz) has become a well-established method for the remote sensing of soil moisture [1], [2]. It is currently being deployed, e.g. in the European Space Agency's Soil Moisture and Ocean Salinity (SMOS) mission, to globally monitor soil moisture with a spatial resolution of approximately 45 km and a revisit time of less than three days [3]. It was first suggested almost 30 years ago that soil moisture can be retrieved from remotely sensed thermal radiance measured with an L-band radiometer [4], [5]. Since then, many methodological studies have attempted to improve the emission models applied to retrieve soil moisture from the signatures measured, and have investigated the influence of, e.g. vegetation [6], [7], soil temperature [8], [9], snow cover [10], soil frost [11] and surface roughness [12], [13] on the microwave emission of land surfaces.

In most of these studies, the scene observed by a radiometer is assumed to be a horizontal plane with uniform (effective) dielectric properties observed under the same observation angle throughout the entire footprint. This is an appropriate assumption, when the antenna field of view is narrow and the surface observed has no pronounced relief. However, when the field of view becomes wider, different regions within the footprint area are observed under significantly different local observation angles. Furthermore, when the scene has a distinct relief, the local observation angles change for different regions within the footprint area as a function of the surface slope and aspect, and depolarization effects occur due to the rotation of the plane of linear polarization. Additionally, some regions can be obscured from the sky radiation by their surroundings and are then illuminated by the elevated landscape instead [14].

Only in recent years have the effects of relief on microwave signatures been increasingly addressed in scientific studies (e.g., [15]–[17]), and little appropriate experimental data is available to date [18]. Most of this research has concentrated on large-scale topographic effects, such as the impact of mountain slopes and valleys, relevant for satellite remote-sensing applications such as SMOS, and tends to be based on simulation results only. In this study, a combined experimental and modeling approach was used to investigate the influence of much smaller surface features, namely erosion gullies, which are not accounted for in the studies mentioned above. The main objective of this study was to investigate these relief effects and how they vary with time as a result of changing ambient conditions.

To this end, brightness temperatures at 1.4 GHz of two adjacent, mainly vegetation-free footprint areas with similar soils but different relief characteristics were measured quasi-simultaneously from September 2008 to December 2009 with an L-band radiometer mounted on a tower (Section 2.1). One of the footprints observed was crossed by distinct erosion gullies with steep and differently orientated slopes, whereas the surface of the other footprint can be regarded as being planar. In addition to the brightness temperature measurements, auxiliary hydrometeorological and *in situ* soil measurements were carried out (Section 2.2), and digital elevation models of the two footprint areas were derived from terrestrial laser scanning (Section 2.3).

A complex model based on geometric optics was developed to simulate brightness temperatures of the two scenes at horizontal and vertical polarization (Section 3). To this end, the

44

footprints were approximated by a mosaic of individual facets corresponding to the pixels of the digital elevation models. The local reflectivity of each facet was calculated from soil-water profiles (simulated with a numerical soil-water and heat-transfer model based on the hydrometeorological measurements) with a coherent radiative-transfer model, taking into account the local observation angles for the individual facets. From the dual-polarized local facet reflectivities, the contribution of each facet to the total brightness temperature at horizontal and vertical polarization of the scene was calculated with a radiative-transfer scheme, considering for depolarization and shadowing effects caused by the relief. The local contributions were then summed up to total simulated antenna temperatures, taking into account the antenna directivity pattern and projection effects.

The simulated and measured brightness temperatures were investigated and compared with each other, as well as between both areas, to analyze the effects of the relief on the microwave emission. In Section 4, first the footprint topographies and their influence on local facet emission are discussed in detail by means of an exemplary brightness temperature simulation for a single time step. Then, brightness temperature measurements and simulations are analyzed for the entire time period of almost 1.5 years rather generally, followed by a more specific analysis for an exemplary time period of six weeks. The results of the analysis are discussed in Section 5, and summarized in Section 6.

2 Experimental Setup and Measurements

The following sections present the measurements carried out in this long-term experiment. In Section 2.1, the setup of the radiometer, the investigation area and the brightness-temperature measurements are described. Section 2.2 presents auxiliary hydrometeorological measurements used in this work. The determination of the topography through laser scanning is explained in Section 2.3, as is the processing of the corresponding data.

2.1 Brightness Temperatures

2.1.1 Setup and Investigation Areas

In the late summer of 2008, the ETH L-Band radiometer ELBARA [19] was installed in the artificial research catchment "Chicken Creek", close to the city of Cottbus in Northeastern Germany (51°36' N, 14°16' E; 130 m a.s.l.). This catchment area was established as a joint research site of the Transregional Collaborative Research Centre (SFB/TR 38) "Structures and processes of the initial ecosystem development phase in an artificial water catchment", where the main objective was to investigate the abiotic and biotic structures and processes controlling the first steps in the development of a new ecosystem [20]. The catchment was completed in 2005 and then left to allow an ecosystem to develop without further restrictions and interference. Further information about this site can be found in [21] and [22]. When ELBARA was set up in September 2008, distinct erosion gullies had already formed in the catchment area. Together with the comprehensive monitoring network present, the catchment was con-

sidered to be an ideal study site to investigate relief effects on L-band emission under natural, but well-characterized, conditions.

ELBARA was installed close to the south-western boundary of the research catchment just outside the ring fence enclosing the entire artificial catchment area and marking the approximate watershed boundaries. It was mounted on a tower with the antenna aperture approximately 10 m above the ground (Fig. 1). ELBARA was equipped with an automated elevation stage [23] and a revolving platform [24], which made it possible to change the view direction of ELBARA in elevation, e.g. to perform sky brightness measurements for external calibration, as well as in azimuth. This enabled us to measure the brightness temperatures of two footprints with different surface characteristics (Fig. 1) quasi-simultaneously.

At the time of installation, footprint area 1 (*A1*, situated just inside the ring fence) was crossed by two very distinct parallel erosion gullies with steep slopes and up to ≈0.5 m deep. A third less distinct gully ran through the area approximately midway between the other two. Footprint area 2 (*A2*), situated just outside the ring fence, was leveled and smoothed prior to beginning the measurements to restore the area to a state comparable to the initial state of the research catchment just after completion. No distinct gullies were therefore present in A2 at the start of the measurement campaign, and the surface can be regarded as smooth. Both areas were covered with only very sparse vegetation (A1) or none at all (A2), and its presence is assumed to have no significant influence on the L-band signatures measured. The soil material of both footprint areas is a sandy substrate several meters thick, underlain by a layer of clay. The substrate is characterized as loamy sand with a bulk density of approximately 1700 kg·m^{-3} and a porosity between 31 and 38% [21]. Neither the relief nor the vegetation cover in A1 changed significantly throughout the entire measurement campaign. In A2, a sparse vegetation cover similar to that in A1 developed in 2009, while the surface relief remained approximately the same.

2.1.2 Remote Sensing System

Brightness temperatures were measured with the ETH L-Band radiometer ELBARA [19]. This Dicke-type radiometer is equipped with a dual-mode Picket-horn antenna [25] (diameter: 1.4 m, length: 2.7 m), with 23.5 dB gain and a −3 dB full beam width of ±6° around the antenna main direction. ELBARA measures brightness temperatures T_B^p at horizontal ($p = H$) and vertical ($p = V$) polarization in the protected frequency range 1400–1427 MHz, corresponding to a vacuum wavelength of $\lambda \approx 0.21$ m. A full measuring cycle consists of two calibration measurements of an internal hot (338 K) and cold source (278 K), and the measurements of the observed scene at horizontal and vertical polarization. All measurements are recorded with 12 s integration time, resulting in an absolute accuracy of the T_B^p measured of around ±1 K and a sensitivity better than 0.1 K. By comparing the measured sky brightness with the theoretical sky brightness calculated with [26], measured T_B^p's were corrected for instrumental noise according to [27]. More information about the technical details of ELBARA can be found in [19].
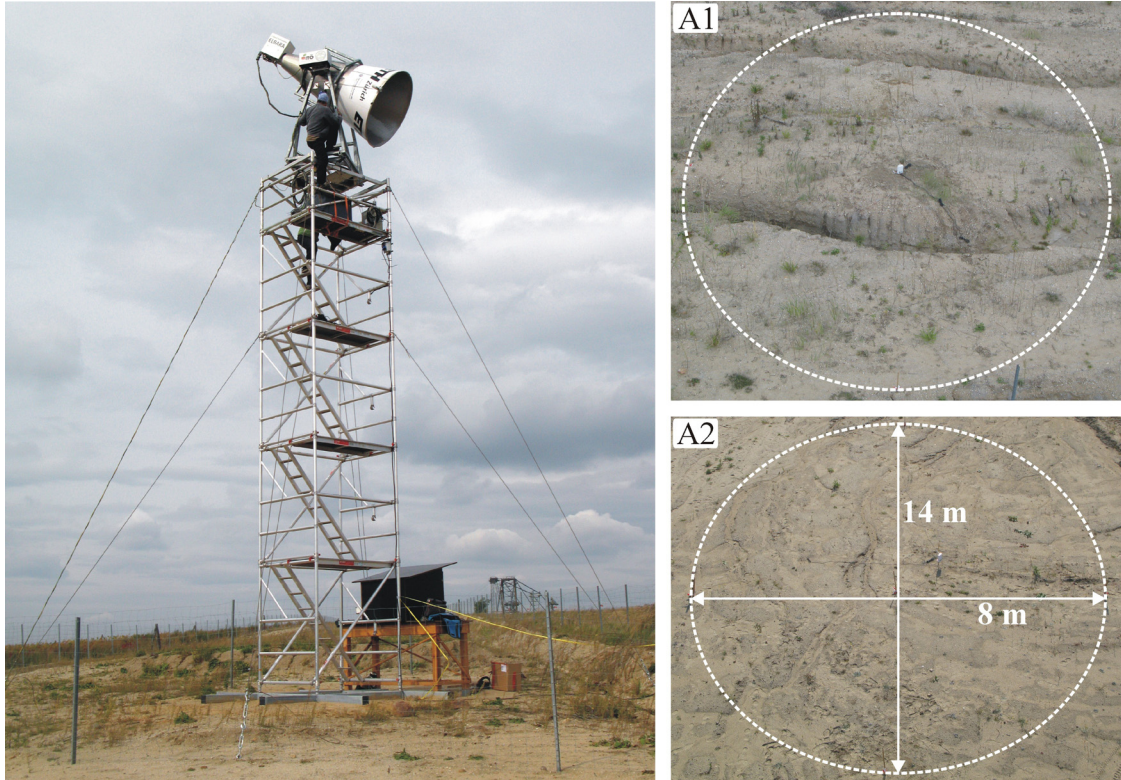
Fig. 1. Left) ELBARA, mounted on a 9 m tower and looking toward footprint A1 at the observation angle $\theta_{RM} = 55°$. The fence on the right is the ring fence enclosing the artificial research catchment "Chicken Creek". The picture was taken from footprint A2. Right) The two areas investigated, as seen from the radiometer tower. The dashed circles show approximately the -12 dB footprint areas ($\pm 13°$ around the antenna main direction), and the arrows indicate the dimensions of the footprint ellipses.

2.1.3 Measurements

Measurements were carried out from the beginning of September 2008 until the end of 2009. Throughout September 2008, only footprint A2 was observed. Brightness temperatures were measured at 2-min intervals at the fixed radiometer observation angle $\theta_{RM} = 55°$ relative to the vertical direction. At the beginning of October 2008, the setup of ELBARA was completed and, afterwards, T_B^p of both footprints (A1, A2) were measured quasi-simultaneously.

One complete measuring cycle consisted of 22 individual T_B^p measurements: First, 16 measurements of footprint A1 were carried out, before ELBARA rotated toward A2. Then, six T_B^p measurements of A2 were taken, before ELBARA rotated back toward A1 and the measuring cycle started again. The individual T_B^p measurements were initiated every five minutes, and a whole measuring cycle lasted 120 minutes. Both footprints were observed at $\theta_{RM} = 55°$. Additionally, sky measurements for external calibration were performed on a regular basis about once every month at $\theta_{RM} = 140°$. For experimental reasons (failure of power supply, broken gear belt connecting the motor with the revolving stage), the time series of T_B^p contains some gaps. The longest time period of consecutive measurements of both footprints lasted for about three months from the beginning of February until the beginning of May 2009. After August 2009, only measurements of A1 are available.

2.2 Meteorological and *in situ* Soil Data

Additional hydrometeorological measurements were carried out in the monitoring network of the SFB/TR38 [28]. Meteorological variables (precipitation, air temperature, relative humidity, shortwave radiation and wind speed) were recorded by two standard weather stations at a temporal resolution of 10 minutes. Snow coverage and snow depth were estimated from daily webcam images. In view of the large spatial variation of the shallow snow cover due to wind drift and surface relief, it was impossible to determine an average snow depth representative of the entire catchment or even sub-areas, such as the erosion gullies. Therefore, we mainly used this information to identify the presence or absence of snow. Groundwater level measurements were made manually at least monthly in groundwater observation pipes located on a 20 m × 20 m grid across the catchment. At the site of the radiometer, the groundwater level fluctuated seasonally between 1.0 and 1.8 m depth.

Volumetric soil-water content wc and soil temperature T_s were recorded at numerous locations both inside and outside the gullies in the artificial catchment area, and also specifically in the footprints A1 and A2 observed by the radiometer. We used ECH_2O EC-TM sensors from Decagon Devices [29], which were installed vertically at 10−15 cm depth in summer 2008. Note that the sensors only measure the liquid soil water, which leads to a significant drop in wc, when the soil freezes.

2.3 Footprint Topography

The topography of the footprints A1 and A2 was derived from terrestrial laser scanning. Measurements were carried out on 6 August 2009 with the time-of-flight laser scanner *RIEGL* LMS-Z420i [30]. The scanner was mounted on the highest platform of the radiometer tower (≈3 m underneath the pivotal point of ELBARA, Fig. 1), and had approximately the same view of the footprints as ELBARA. Additionally, two measurements were performed with the scanner installed on a mobile tower (height: 6.5 m) within the research catchment and looking toward ELBARA, to obtain information about the gully slopes facing away from the radiometer. All scans were performed in last-target mode, i.e. the last return signal of the laser pulse was used to measure the distance. The scanning resolution was set to 0.01° in the vertical and 0.11° in the horizontal direction, resulting in a maximum horizontal measurement point distance of 5 cm × 1 cm within the footprint areas.

The first post-processing of the data was done using the RiSCAN PRO 1.4.3 software package [30]. First, measurements from the radiometer tower were merged with the measurements from within the research catchment, and the raw scan data was clipped approximately to the −12 dB footprint areas A1 and A2 (Fig. 1). Then, measurement points clearly related to vegetation were manually removed from the data. In a next step, a minimum-z-filter with a grid size of 5 cm was applied to retrieve the lowest point in z-direction of each grid cell, which should represent the ground. The filtered point set was then triangulated with a maximum edge length of 0.3 m and a maximum tilt angle of 30° for the triangles in the resulting triangulated irregular network (*TIN*). Because of the deep gullies in footprint A1, the corresponding TIN had some large gaps in the steep gully slopes. By applying a second trian-

gulation with a maximum tilt angle of 90°, these gaps could be partly closed, but not completely.

The resulting surface patches of both footprint areas were converted to ESRI raster data sets and further manipulated in ArcGIS [31]. The data were first manually checked for plausibility, and clearly defective points were removed. Then, the TINs were interpolated to a regular 5 cm × 5 cm grid using the ArcGIS inverse distance weighting tool, which yielded the digital elevation models (x, y, z) of both footprints. The data triples (x, y, z) describe the elevation z of (5×5) cm^2 facets at position (x, y). Using standard surface analysis tools of ArcGIS, the surface normals $\hat{\mathbf{n}}$ of the facets were calculated and facets that cannot be seen from the radiometer were identified and flagged as invisible. Finally, the facets of footprint A1 situated inside the erosion gullies were flagged as such manually.

3 Brightness Temperature Simulations

The signal of a microwave radiometer observing a land surface is composed of surface and atmospheric contributions, both of which depend, amongst other things, on the relief [32]. The relief-dependency of the atmospheric contributions is ignored in this discussion as the atmosphere is mostly transparent at the observation wavelength $\lambda = 0.21$ m of ELBARA and, additionally, the distance to the observed footprints is small (< 30 m). More relevant for the following discussion is the surface of the observed footprints, which is rather smooth in A2, but shows distinct erosion gullies with steep and differently oriented slopes in A1 (Fig. 1). Furthermore, both footprints (leaving aside the erosion gullies) are slightly tilted with respect to the horizontal ($\approx 4°$). Under such circumstances, deviations occur from the standard hemispheric emission of a horizontal surface. On the one hand, the local incidence angle and the orientation of the plane of linear polarization of a tilted surface depend on the tilt angle, the orientation and the position of the surface with respect to the view direction of the sensor. On the other hand, the tilted surfaces imply a variable and elevated horizon that may obscure parts of the sky. Along these directions, the incident radiance is no longer the cold sky radiation but the much stronger radiation from the elevated landscape.

To describe these effects, a facet model was implemented. That means, we approximated the actual surfaces of the observed footprints by a mosaic of small planar surface elements (*facets*), which are tangential to the actual surface and whose deviations from the real surface are much smaller than the observation wavelength. The locations of the individual facets are given by their spatial coordinates (x, y, z), and the facets' inclination (tilt) and orientation (exposition) are described by their surface normals $\hat{\mathbf{n}}$ (Section 2.3). The facets were assumed to be locally smooth and specularly reflecting, i.e. diffuse scattering was ignored. Furthermore, we assumed the soil temperature and soil-water content were the same everywhere within both footprint areas except for facets situated inside the erosion gullies. In a first step, we calculated the local emissions of the individual facets toward ELBARA. Subsequently, the total signal received by the radiometer antenna was determined in geometrical optics from the con-

volution of the local emissions from all facets with the antenna directivity pattern. Such a model was proposed in [33], further investigated in [14], and has been used, e.g. to describe the microwave emission of a mountainous region in Northern Italy in [17].

Below, we make some basic definitions that are essential for understanding our facet model. Then, we give a short overview of the general modeling approach in Section 3.2, before describing the different sub-modules in more detail in Sections 3.3 to 3.6.

3.1 Basic Definitions and Radiative Transfer

When calculating the local emission from an individual tilted facet toward the radiometer, located at (x_{RM}, y_{RM}, z_{RM}), we have to consider the tilt and exposition of the facet as well as the deviation of the direction of the antenna main axis $\mathbf{k}_{RM}$ from the view direction $\mathbf{k}_F = (x_{RM} - x, y_{RM} - y, z_{RM} - z)$ from the facet toward the radiometer (Fig. 2). For this reason, we introduce the following three *planes of incidence* (POI) and corresponding elevation angles[1] to begin with:

-- The *radiometer* or *global plane of incidence* (RM-POI) is normal to the XY -plane (thus parallel to the vertical $\hat{\mathbf{z}}$ direction), and comprises the antenna main axis $\mathbf{k}_{RM}$. That means, it is spanned by the two unit vectors $\hat{\mathbf{k}}_{RM}$ (given by the radiometer setup) and $\hat{\mathbf{z}} = (0,0,1)$. The corresponding *radiometer elevation angle* $\theta_{RM} = 55°$ is the nadir angle of the antenna main axis.

-- The *view-direction plane of incidence* (VD-POI) of a facet is also normal to the XY-plane, but is spanned by the two unit vectors $\hat{\mathbf{k}}_F$ and $\hat{\mathbf{z}}$. The corresponding *view-direction elevation angle* θ_{VD} is the observation angle under which an individual facet is seen from ELBARA. It is given by the scalar product

$$\cos\theta_{VD} = \hat{\mathbf{z}} \cdot \hat{\mathbf{k}}_F. \tag{1}$$

-- The *facet* or *local plane of incidence* (F-POI) is the local plane of incidence of the facet. It is normal to the facet's surface (thus parallel to its surface normal $\hat{\mathbf{n}}$, but not, in general, to $\hat{\mathbf{z}}$), also comprises $\hat{\mathbf{k}}_F$, and is consequently spanned by $\hat{\mathbf{n}}$ and $\hat{\mathbf{k}}_F$. The corresponding *facet elevation angle* θ_F is the angle of incidence of radiation incident on a facet, which is then reflected toward ELBARA. It is given by the scalar product

$$\cos\theta_F = \hat{\mathbf{n}} \cdot \hat{\mathbf{k}}_F. \tag{2}$$

With the different planes of incidence identified, the emission from a single surface facet in direction $\hat{\mathbf{k}}_F$ toward the radiometer was calculated with

$$T_B^p = \left(1 - R_{RM}^p\right)T_{eff} + R_{RM}^p T_{in}. \tag{3}$$

This zero-order radiative-transfer model fulfills Kirchhoff's law and describes the *p*-polarized brightness temperature T_B^p (*p* = H, V) emitted by a facet with reflectivity R_{RM}^p and effec-

---

[1] A complete list of used abbreviations and symbols with short explanations can be found in Appendix A.
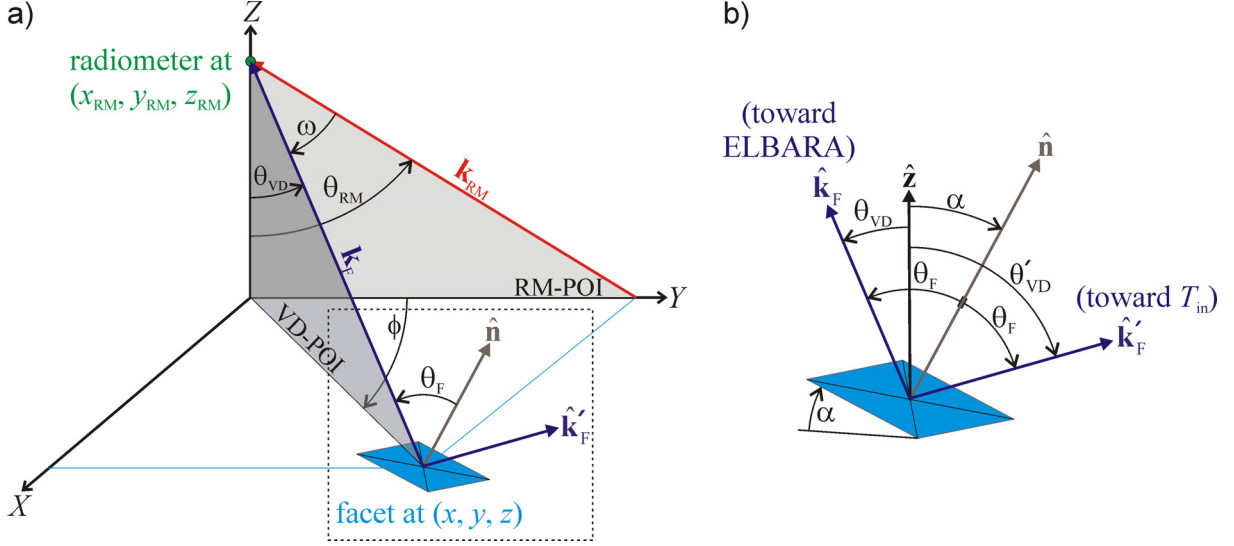
a)

b)

Fig. 2. a) Sketch illustrating the setup that has to be considered, when calculating the reflection on and emission from a tilted facet toward ELBARA. The cut-out inside the dotted box is shown in more detail in panel b). The radiometer is mounted at (x_{RM}, y_{RM}, z_{RM}), with the observation angle $\theta_{RM} = 55°$ relative to the vertical and the antenna main axis $\mathbf{k}_{RM}$. The facet considered is located at (x, y, z) and tilted with respect to the horizontal by the angle α. It is observed from the radiometer under the view-direction elevation angle θ_{VD}, and $\mathbf{k}_F$ is the view direction from the facet to the radiometer. The vector $\hat{\mathbf{k}}'_F$ points toward the direction of radiation T_{in} incident on the facet that is specularly reflected toward ELBARA. The vector $\hat{\mathbf{n}}$ is the facet's surface normal and the angle θ_F is the facet elevation angle. Additionally, the angle ω between $\mathbf{k}_{RM}$ and $\mathbf{k}_F$ and the azimuth angle ϕ between the RM-POI and the VD-POI (illustrated by the gray shaded areas) are shown. b) Cut-out from panel a) illustrating the relationship between the unit vectors $\hat{\mathbf{k}}_F$, $\hat{\mathbf{k}}'_F$, $\hat{\mathbf{z}}$ and $\hat{\mathbf{n}}$ and the angles α, θ_F, θ_{VD} and θ'_{VD}. The F-POI (not especially illustrated for the sake of better readability) comprises the vectors $\hat{\mathbf{n}}$, $\hat{\mathbf{k}}_F$ and $\hat{\mathbf{k}}'_F$, but not the vertical $\hat{\mathbf{z}}$.

tive physical temperature T_{eff} as the sum of the radiation emitted from the facet and the fraction of radiation T_{in} incident on the facet, which is specularly reflected on the facet toward ELBARA. The radiation T_{in} is either the sky radiation $T_{sky} \approx 6$ K [26] or the radiation of the surrounding landscape T_{eff} for facets, which are obscured from the sky by their surroundings. For the following description of the modeling approach, it is important to bear in mind that R^p_{RM} (p = H, V with respect to the RM-POI) describes the facet's global reflectivity at $\theta_{RM} = 55°$.

3.2 General Modeling Approach

The signal at the output of the radiometer antenna (i.e. the antenna brightness temperature) is a weighted mean of the brightness temperatures of the individual facets within the respective footprint. To simulate the facets' brightness temperatures taking into account the surface relief, we followed the course of action illustrated in the flowchart in Fig. 3. First, we calculated the soil-water content and soil temperature profiles for the entire time span of the experiment with a numerical soil-water and heat-transfer model (Section 3.3). From the soil temperature profiles we derived the effective temperature T_{eff} needed in (3). The soil-water content profiles were converted into soil permittivity profiles and subsequently used as input

to a coherent radiative-transfer model for layered dielectric media. Evaluating this model yielded the local reflectivities R_F^p of all facets at the respective times of the radiometer measurements (Section 3.4). These local values describe the facet reflectivities at polarization $p = $ H, V with respect to the facets' local planes of incidence (F-POI) and local elevation angles θ_F.

In the next step, the global facet reflectivities R_{RM}^p were derived from R_F^p by applying a transformation from the local to the global plane of incidence (Section 3.5). This transformation accounts for the rotation of the plane of linear polarization resulting from the tilt of the facets and the deviation of the facets' view directions $\hat{\mathbf{k}}_F$ from the antenna main axis $\hat{\mathbf{k}}_{RM}$. Once the reflectivities R_{RM}^p of all facets were known, they were used in (3) to calculate the emission of the individual facets toward ELBARA for all the times of the radiometer measurements. Summing up the contributions of all facets within the respective footprint area, taking into account the antenna's directivity pattern as well as shadowing and projection effects, eventually yielded time series of simulated antenna brightness temperatures for A1 and A2 for the times of the radiometer measurements (Section 3.6).

3.3 Soil-Water Content and Soil Temperature Profiles

Soil-water content wc and soil temperature T_s profiles were simulated for the time period from September 2008 to December 2009 at one-hour time intervals using the one-dimensional numerical soil-water and heat-transfer model COUP [11], [34]. The model calculates the water and heat fluxes from the soil surface to a depth of 3 m, assuming a layered vertical soil profile with predefined thermal and hydrological properties.

The upper boundary conditions of the profile are governed by the soil surface energy balance, which takes into account the evaporation fluxes and a potentially present snow cover. To this end, hourly values of precipitation, air temperature, relative humidity, shortwave radiation and wind speed are the driving model variables. Furthermore, groundwater level measurements were used as input to the COUP model, determining the lower hydraulic boundary conditions. The vertical water flow in the unsaturated zone was represented with the Richards equation [35], using *pF* curves parameterized according to Brooks and Corey [36] and the Mualem function for unsaturated hydraulic conductivity. The applied parameter values (Table I) were approximated based on information on soil texture and *in situ* hydraulic conductivity measurements [21], and further tuned to give a best match with the *in situ wc* and T_s measurements at a depth of 10–15 cm.

The model was first run for a typical location outside the erosion gullies. A second simulation represented the conditions of a typical gully, having an approximately 50 cm shorter distance to the groundwater table and thus a higher and more balanced water content. The simulated *wc* profiles were subsequently used as input to the local facet reflectivity model (Section 3.4), and from the T_s profiles we derived the effective soil temperature T_{eff}, which was assumed to be the simulated temperature at a depth of 8 cm. This choice gave the best overall agreement of measurement and simulation results, when T_{eff} was approximated by the soil
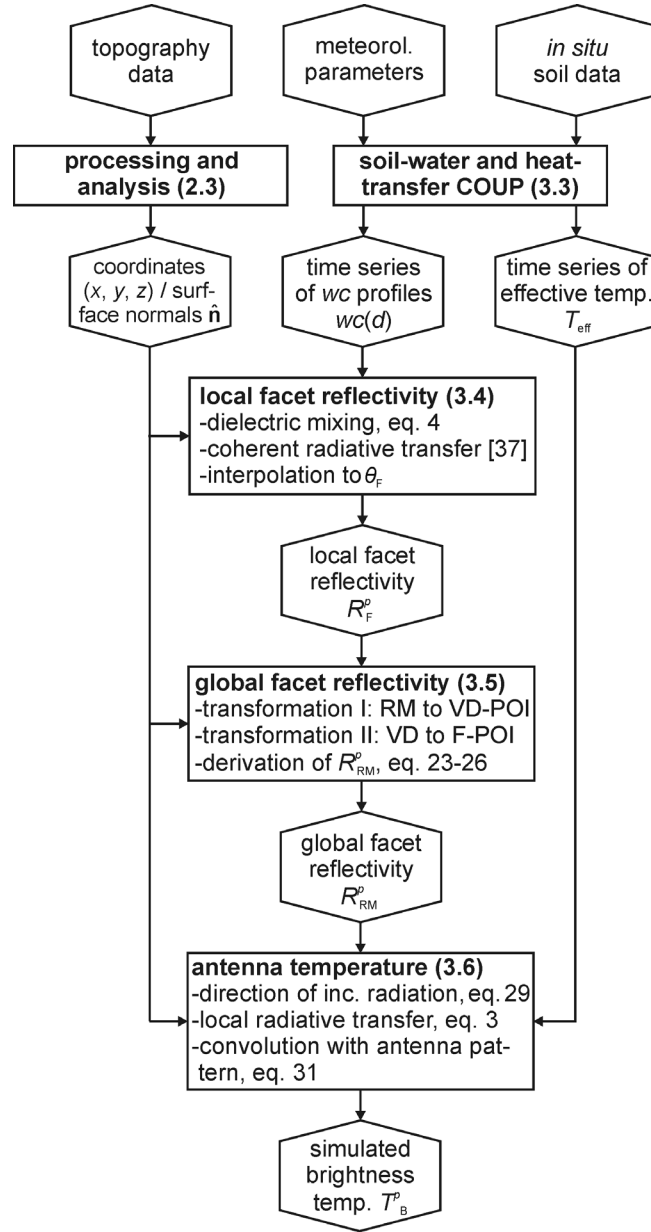
Fig. 3. Flowchart illustrating the process chain followed to simulate brightness temperatures. Hexagons indicate the model in- and outputs. Boxes show the sub-modules of the facet model, which are further explained in the sections indicated by the numbers in parentheses.

Table I. Soil parameter values used in the COUP model for the simulation of the soil-water content and soil temperature profiles (wc_{sat} = saturation water content, ψ_a = air entry pressure, λ_p = pore size distribution index, wc_{res} = residual water content, k_{sat} = saturated hydraulic conductivity).

soil depth	wc_{sat}	ψ_a	λ_p	wc_{res}	k_{sat} [a]	k_{sat} [b]
(m)	(m$^3 \cdot$m^{-3})	(cm)	(–)	(m$^3 \cdot$m^{-3})	(mm$\cdot$d^{-1})	(mm$\cdot$d^{-1})
0–0.06	0.27	15	0.60	0.055	200	50
0.06–0.30	0.31	15	0.60	0.055	2500	250
0.30–0.70	0.28	10	0.15	0.080	4000	400

[a] incl. macropores

[b] excl. macropores

temperature at a certain constant depth in the brightness temperature simulations. However, the depth of 8 cm might be an overestimation for moist soil states and an underestimation for very dry soil.

3.4 Local Facet Reflectivity

To calculate the local facet reflectivities R_F^p (p = H, V), we used a coherent radiative-transfer model for layered dielectric media [37]. The model is based on a matrix formulation of the boundary conditions at the layer interfaces derived from Maxwell's Equations. Inputs to the model are the soil permittivity profile $\varepsilon(d)$ (d = depth below surface), observation wavelength λ, polarization p, and the observation angle θ_F. The model's output is the reflectivity of the layer stack. The model was evaluated for dielectric layers with a thickness of 2 mm $\ll \lambda$.

The soil permittivity profiles required were generated from the *wc* profiles calculated with the COUP model for locations inside and outside the erosion gullies (Section 3.3). First, simulated *wc* were linearly interpolated to the depths d of the dielectric layers (corresponding to the model discretization), and then the soil permittivity profile $\varepsilon(d)$ was derived from *wc*(d) by applying the empirical mixing model for mineral soils with $0\ \mathrm{m^3 \cdot m^{-3}} \leq wc \leq 0.55\ \mathrm{m^3 \cdot m^{-3}}$ derived in [38][2]

$$\varepsilon = 3.03 + 9.3wc + 146.0wc^2 - 76.7wc^3. \tag{4}$$

Evaluating the dielectric layer model for each individual facet and corresponding local observation angle was not feasible due to the large number of facets (Table II), which would have required great computational effort to handle. To save computing time, we used the following approach based on look-up tables instead. First, the dielectric layer model was evaluated for observation angles $0° \leq \theta_F \leq 90°$ in steps of 5°, yielding $R_F^p(\theta_F)$ for each soil-water content profile *wc*(d) simulated. Subsequently, these reflectivities were interpolated to the times of the radiometer measurements since the COUP simulations were only available at hourly time intervals. Thus, two look-up tables of local facet reflectivities (inside and outside the gullies) were generated, each containing $R_F^p(t, \theta_F)$ for all times t of radiometer measurements and observation angles θ_F between 0° and 90° in steps of 5°. Subsequently, we derived the local facet reflectivities $R_F^p(t, \theta_F)$ from the appropriate look-up table (depending on the location of the facet considered) by interpolating to the actual local angles of incidence θ_F of the individual facets.

3.5 Global Facet Reflectivity

From the local values R_F^p, we subsequently derived the global reflectivities R_{RM}^p describing the reflectivity of a considered surface facet at global *p*-polarization. To derive expressions for R_{RM}^p (p = H, V), we reversed the field propagation directions and considered ELBARA to be a transmitter of *p*-polarized radiation with the unit field vector $\hat{\mathbf{E}}_{RM}^p$. Further-

---

[2] An estimation of the uncertainties introduced through the choice of the dielectric mixing model can be found in Appendix C.

more, the sky was regarded as an unpolarized receiver absorbing the energy carried by the field $\mathbf{E}_{\text{ref}}$ reflected along the forward direction on the facet. This implies that R_{RM}^{p} is the ratio between the reflected energy carried by $\mathbf{E}_{\text{ref}}$ and the energy transmitted by the radiometer. As the energy carried by these electric fields is proportional to their squared field amplitudes, we can compute R_{RM}^{p} as

$$R_{\text{RM}}^{p} = \frac{\left|\mathbf{E}_{\text{ref}}\right|^{2}}{\left|\hat{\mathbf{E}}_{\text{RM}}^{p}\right|^{2}} = \left|\mathbf{E}_{\text{ref}}\right|^{2}. \tag{5}$$

To determine $\left|\mathbf{E}_{\text{ref}}\right| = \text{E}_{\text{ref}}$, the transmitted field $\hat{\mathbf{E}}_{\text{RM}}^{p}$ was first decomposed into its locally horizontal and vertical components $\mathbf{E}_{\text{F}}^{\text{H}}$ and $\mathbf{E}_{\text{F}}^{\text{V}}$, which are reflected on the facet with the local reflectivities R_{F}^{H} and R_{F}^{V}, respectively. That means, once the fields $\mathbf{E}_{\text{F}}^{p}$ incident on the facet were known, the local reflectivities R_{F}^{p} computed beforehand (Section 3.4) could be used to calculate E_{ref} and, in turn, R_{RM}^{p}.

Determining $\mathbf{E}_{\text{F}}^{p}$ from $\hat{\mathbf{E}}_{\text{RM}}^{p}$ requires the following steps: 1) A transformation from the global plane of incidence (RM-POI) to the view-direction plane of incidence (VD-POI), as the radiance emitted by ELBARA is propagating along $-\hat{\mathbf{k}}_{\text{RM}}$, which deviates from the view direction $-\hat{\mathbf{k}}_{\text{F}}$ toward the facet, and 2) a transformation from the VD-POI to the local plane of incidence (F-POI) because the facet's surface normal $\hat{\mathbf{n}}$, which defines the F-POI, deviates from the vertical $\hat{\mathbf{z}}$ direction defining the VD-POI.

3.5.1 Transformation I: RM-POI to VD-POI

A globally horizontal electric field $\hat{\mathbf{E}}_{\text{RM}}^{\text{H}}$ transmitted by the radiometer propagates along $-\hat{\mathbf{k}}_{\text{RM}}$, which deviates from the view direction toward the facet $-\hat{\mathbf{k}}_{\text{F}}$ in elevation by $\left(\theta_{\text{RM}} - \theta_{\text{VD}}\right)$ and in azimuth by the angle ϕ (Fig. 2). As a consequence, $\hat{\mathbf{E}}_{\text{RM}}^{\text{H}}$ is globally horizontal, but has a horizontal component $\mathbf{E}_{\text{VD}}^{\text{HH}}$, as well as a vertical component $\mathbf{E}_{\text{VD}}^{\text{HV}}$, with respect to the VD-POI[3]. Similarly, this holds true for a globally vertical field $\hat{\mathbf{E}}_{\text{RM}}^{\text{V}}$. To derive the field vectors $\mathbf{E}_{\text{VD}}^{pp'}$[4], we projected $\hat{\mathbf{E}}_{\text{RM}}^{p}$ onto the directions p' (p' = H, V) with respect to the VD-POI, given by the two unit vectors

$$\hat{\mathbf{E}}_{\text{VD}}^{\text{H}} = \frac{\hat{\mathbf{z}} \times \hat{\mathbf{k}}_{\text{F}}}{\left|\hat{\mathbf{z}} \times \hat{\mathbf{k}}_{\text{F}}\right|} \qquad \text{for } p' = \text{H, and}$$

$$\hat{\mathbf{E}}_{\text{VD}}^{\text{V}} = \frac{\hat{\mathbf{E}}_{\text{VD}}^{\text{H}} \times \hat{\mathbf{k}}_{\text{F}}}{\left|\hat{\mathbf{E}}_{\text{VD}}^{\text{H}} \times \hat{\mathbf{k}}_{\text{F}}\right|} \quad \text{for } p' = \text{V.} \tag{6}$$

---

[3] These two vectors are usually not sufficient to describe $\hat{\mathbf{E}}_{\text{RM}}^{\text{H}}$ completely. A third vector $\mathbf{E}_{\text{VD}}^{\text{H}\hat{\mathbf{k}}_{\text{F}}}$, parallel to $\hat{\mathbf{k}}_{\text{F}}$, and therefore not propagating toward the facet, is necessary. Only $\mathbf{E}_{\text{VD}}^{\text{HH}}$ and $\mathbf{E}_{\text{VD}}^{\text{HV}}$ propagate along $-\hat{\mathbf{k}}_{\text{F}}$ toward the facet, which implies, on the one hand, that not all the energy carried by $\hat{\mathbf{E}}_{\text{RM}}^{\text{H}}$ reaches the facet and, on the other hand, that only $\mathbf{E}_{\text{VD}}^{\text{HH}}$ and $\mathbf{E}_{\text{VD}}^{\text{HV}}$ are reflected on the facet.

[4] The notation has to be read like this: The field vector $\mathbf{E}_{\text{VD}}^{pp'}$ is the component of $\hat{\mathbf{E}}_{\text{RM}}^{p}$ (p = H, V with respect to the RM-POI), which is p'-polarized (p' = H, V) with respect to the VD-POI.

Projecting $\hat{\mathbf{E}}_{RM}^{H}$ onto the two directions given by (6) yields the two field vectors

$$
\begin{aligned}
\mathbf{E}_{VD}^{HH} &= \left(\hat{\mathbf{E}}_{RM}^{H} \cdot \hat{\mathbf{E}}_{VD}^{H} \right) \hat{\mathbf{E}}_{VD}^{H} \\
\mathbf{E}_{VD}^{HV} &= \left(\hat{\mathbf{E}}_{RM}^{H} \cdot \hat{\mathbf{E}}_{VD}^{V} \right) \hat{\mathbf{E}}_{VD}^{V}
\end{aligned}
\tag{7}
$$

and proceeding equally for $\hat{\mathbf{E}}_{RM}^{V}$ yields

$$
\begin{aligned}
\mathbf{E}_{VD}^{VH} &= \left(\hat{\mathbf{E}}_{RM}^{V} \cdot \hat{\mathbf{E}}_{VD}^{H} \right) \hat{\mathbf{E}}_{VD}^{H} \\
\mathbf{E}_{VD}^{VV} &= \left(\hat{\mathbf{E}}_{RM}^{V} \cdot \hat{\mathbf{E}}_{VD}^{V} \right) \hat{\mathbf{E}}_{VD}^{V}.
\end{aligned}
\tag{8}
$$

Once the components $\mathbf{E}_{VD}^{pp'}$ were known, the coefficients $a_1^{pp'}$ relating their magnitudes $\mathbf{E}_{VD}^{pp'} = \left| \mathbf{E}_{VD}^{pp'} \right|$ to the magnitudes of $\hat{\mathbf{E}}_{RM}^{H}$ and $\hat{\mathbf{E}}_{RM}^{V}$ were computed

$$
\begin{aligned}
\mathbf{E}_{VD}^{HH} &= a_1^{HH} \left| \hat{\mathbf{E}}_{RM}^{H} \right| = a_1^{HH} \\
\mathbf{E}_{VD}^{HV} &= a_1^{HV} \left| \hat{\mathbf{E}}_{RM}^{H} \right| = a_1^{HV} \\
\mathbf{E}_{VD}^{VH} &= a_1^{VH} \left| \hat{\mathbf{E}}_{RM}^{V} \right| = a_1^{VH} \\
\mathbf{E}_{VD}^{VV} &= a_1^{VV} \left| \hat{\mathbf{E}}_{RM}^{V} \right| = a_1^{VV}.
\end{aligned}
\tag{9}
$$

The coefficients $a_1^{pp'}$ can also be expressed by means of the elevation angles θ_{RM} and θ_{VD} and the azimuth angle ϕ between the RM-POI and VD-POI. Elaborate algebraic calculations yield

$$
\begin{aligned}
a_1^{HH} &= \cos\phi \\
a_1^{HV} &= \sin\phi \cos\theta_{VD} \\
a_1^{VH} &= \sin\phi \cos\theta_{RM} \\
a_1^{VV} &= \sin\theta_{RM} \sin\theta_{VD} + \cos\phi \cos\theta_{RM} \cos\theta_{VD}.
\end{aligned}
\tag{10}
$$

The angle ϕ is given by the scalar product of the projections of $\hat{\mathbf{k}}_{RM}$ and $\hat{\mathbf{k}}_{F}$ onto the XY-plane (denoted as $\hat{\mathbf{k}}_{RM,xy}$ and $\hat{\mathbf{k}}_{F,xy}$, respectively)

$$
\cos\phi = \frac{\hat{\mathbf{k}}_{RM,xy} \cdot \hat{\mathbf{k}}_{F,xy}}{\left| \hat{\mathbf{k}}_{RM,xy} \right| \cdot \left| \hat{\mathbf{k}}_{F,xy} \right|}.
\tag{11}
$$

3.5.2 *Transformation II: VD-POI to F-POI*

The local F-POI of a facet is different from its VD-POI, when the facet considered is tilted (Fig. 2). Consequently, the orientation of linear polarization of the F-POI is rotated by an angle φ with respect to the corresponding polarization direction of the VD-POI. This angle of polarization rotation was determined as follows: The direction of H-polarization with respect to the F-POI is normal to both $\hat{\mathbf{n}}$ and $\hat{\mathbf{k}}_{F}$, and thus parallel to their cross product $\hat{\mathbf{n}} \times \hat{\mathbf{k}}_{F}$. The direction of H-polarization with respect to the VD-POI is defined by $\hat{\mathbf{E}}_{VD}^{H}$ given in (6). That means the angle φ is given by

$$\cos\varphi = \frac{\hat{\mathbf{E}}_{VD}^{H} \cdot \left(\hat{\mathbf{n}} \times \hat{\mathbf{k}}_{F}\right)}{\left|\hat{\mathbf{n}} \times \hat{\mathbf{k}}_{F}\right|}. \tag{12}$$

Knowing φ, an electric field $\mathbf{E}_{VD}^{H}$ incident on the facet can be decomposed into a locally horizontal field $\mathbf{E}_{F}^{HH}$ and a locally vertical field $\mathbf{E}_{F}^{HV}$, with the magnitudes given by

$$
\begin{aligned}
\mathrm{E}_{F}^{HH} &= \cos\varphi \left|\mathbf{E}_{VD}^{H}\right| \\
\mathrm{E}_{F}^{HV} &= \sin\varphi \left|\mathbf{E}_{VD}^{H}\right|.
\end{aligned}
\tag{13}
$$

Likewise, an incident field $\mathbf{E}_{VD}^{V}$ can be decomposed into the locally horizontal and vertical fields

$$
\begin{aligned}
\mathrm{E}_{F}^{VH} &= \sin\varphi \left|\mathbf{E}_{VD}^{V}\right| \\
\mathrm{E}_{F}^{VV} &= \cos\varphi \left|\mathbf{E}_{VD}^{V}\right|.
\end{aligned}
\tag{14}
$$

Similarly to (9), we substituted $a_{2}^{pp'}$ for the coefficients in (13) and (14), yielding

$$\mathrm{E}_{F}^{pp'} = a_{2}^{pp'} \left|\mathbf{E}_{VD}^{p}\right| \tag{15}$$

with the coefficients

$$
\begin{aligned}
a_{2}^{HH} &= \cos\varphi \\
a_{2}^{HV} &= \sin\varphi \\
a_{2}^{VH} &= \sin\varphi \\
a_{2}^{VV} &= \cos\varphi.
\end{aligned}
\tag{16}
$$

3.5.3 Derivation of the Global Facet Reflectivity R_{RM}^{p}

Using the calculations described above, we can now express a globally horizontal field through its horizontal and vertical polarization with respect to the local F-POI, and thus determine R_{RM}^{H} as explained below. The globally H-polarized electric field transmitted by the radiometer is $\hat{\mathbf{E}}_{RM}^{H}$. The corresponding field $\mathbf{E}_{in}$ incident on the facet can then be described with the two field vectors $\mathbf{E}_{VD}^{HH}$ and $\mathbf{E}_{VD}^{HV}$, which are H- and V-polarized with respect to the VD-POI (Transformation I, Section 3.5.1)

$$\mathbf{E}_{in} = \mathbf{E}_{VD}^{HH} + \mathbf{E}_{VD}^{HV}. \tag{17}$$

They, in turn, are further decomposed into locally horizontal and vertical field vectors $\mathbf{E}_{F}^{pp'}$ (Transformation II, Section 3.5.2), yielding

$$\mathbf{E}_{in} = \overbrace{\mathbf{E}_{F}^{HH} + \mathbf{E}_{F}^{HV}}^{\mathbf{E}_{VD}^{HH}} + \overbrace{\mathbf{E}_{F}^{VH} + \mathbf{E}_{F}^{VV}}^{\mathbf{E}_{VD}^{HV}}. \tag{18}$$

These fields, which are H- and V-polarized with respect to the F-POI, are reflected on the facet with R_F^H and R_F^V, respectively. The following holds true for the magnitudes of the reflected fields

$$\left(E_{F,ref}^{pp'}\right)^2 = R_F^{p'}\left(E_F^{pp'}\right)^2.$$
(19)

The total field $\mathbf{E}_{ref}$ reflected on the facet is the linear combination of all the reflected fields $\mathbf{E}_{F,ref}^{pp'}$. Thus using (19), we can write for the magnitude E_{ref}

$$\left(E_{ref}\right)^2 = R_F^H\left(E_F^{HH}\right)^2 + R_F^V\left(E_F^{HV}\right)^2 + R_F^H\left(E_F^{VH}\right)^2 + R_F^V\left(E_F^{VV}\right)^2.$$
(20)

Inserting (15) into (20) we get

$$\left(E_{ref}\right)^2 = R_F^H\left(a_2^{HH}\left|\mathbf{E}_{VD}^H\right|\right)^2 + R_F^V\left(a_2^{HV}\left|\mathbf{E}_{VD}^H\right|\right)^2 + R_F^H\left(a_2^{VH}\left|\mathbf{E}_{VD}^V\right|\right)^2 + R_F^V\left(a_2^{VV}\left|\mathbf{E}_{VD}^V\right|\right)^2$$
(21)

and now inserting (9) yields

$$\left(E_{ref}\right)^2 = \left[\left(a_1^{HH}a_2^{HH}\left|\mathbf{E}_{RM}^H\right|\right)^2 + \left(a_1^{HV}a_2^{VH}\left|\mathbf{E}_{RM}^H\right|\right)^2\right]R_F^H +$$
$$\left[\left(a_1^{HH}a_2^{HV}\left|\mathbf{E}_{RM}^H\right|\right)^2 + \left(a_1^{HV}a_2^{VV}\left|\mathbf{E}_{RM}^H\right|\right)^2\right]R_F^V.$$
(22)

Substituting $\left(E_{ref}\right)^2 = R_{RM}^H$ and $\left|\hat{\mathbf{E}}_{RM}^H\right| = 1$ in (22) yields

$$R_{RM}^H = \left[\left(a_1^{HH}a_2^{HH}\right)^2 + \left(a_1^{HV}a_2^{VH}\right)^2\right]R_F^H + \left[\left(a_1^{HH}a_2^{HV}\right)^2 + \left(a_1^{HV}a_2^{VV}\right)^2\right]R_F^V$$
(23)

and, inserting the expressions (10) and (16) for $a_i^{pp'}$ $(i = 1, 2)$, we eventually get

$$R_{RM}^H = \left(\cos^2\phi\cos^2\varphi + \sin^2\phi\cos^2\theta_{VD}\sin^2\varphi\right)R_F^H +$$
$$\left(\cos^2\phi\sin^2\varphi + \sin^2\phi\cos^2\theta_{VD}\cos^2\varphi\right)R_F^V.$$
(24)

Following the corresponding procedure for a transmitted field $\hat{\mathbf{E}}_{RM}^V$ yields eventually

$$R_{RM}^V = \left[\left(a_1^{VH}a_2^{HH}\right)^2 + \left(a_1^{VV}a_2^{VH}\right)^2\right]R_F^H + \left[\left(a_1^{VH}a_2^{HV}\right)^2 + \left(a_1^{VV}a_2^{VV}\right)^2\right]R_F^V, \text{ and}$$
(25)

$$R_{RM}^V = \left(\sin^2\phi\cos^2\theta_{RM}\cos^2\varphi + \left(\sin\theta_{RM}\sin\theta_{VD} + \cos\phi\cos\theta_{RM}\cos\theta_{VD}\right)^2\sin^2\varphi\right)R_F^H +$$
$$\left(\sin^2\phi\cos^2\theta_{RM}\sin^2\varphi + \left(\sin\theta_{RM}\sin\theta_{VD} + \cos\phi\cos\theta_{RM}\cos\theta_{VD}\right)^2\cos^2\varphi\right)R_F^V$$
(26)

for the facet reflectivity R_{RM}^V at global V-polarization.

Using (23) and (25), the global facet reflectivities R_{RM}^p were then calculated from the local facet reflectivities R_F^p calculated previously with the coherent radiative-transfer model for layered dielectric media (Section 3.4).

3.6 Antenna Brightness Temperature

Before the global facet reflectivities could be used in the radiative-transfer model (3) to calculate the brightness temperatures of the individual facets, we had to determine the direction of the radiation T_{in} incident on the facets and reflected toward ELBARA. This was necessary to distinguish facets receiving radiation from the sky from facets, which receive radiation from the surrounding landscape or even self-emission from the antenna.

The radiation that is specularly reflected on the facet toward the radiometer is incident from the direction $-\hat{\mathbf{k}}'_{\mathrm{F}}$, as shown in Fig. 2. From the relationship $\hat{\mathbf{k}}_{\mathrm{F}} + \hat{\mathbf{k}}'_{\mathrm{F}} = \cos\theta_{\mathrm{F}}\left|\hat{\mathbf{k}}_{\mathrm{F}}\right|\hat{\mathbf{n}} + \cos\theta_{\mathrm{F}}\left|\hat{\mathbf{k}}'_{\mathrm{F}}\right|\hat{\mathbf{n}}$ between the unit vectors $\hat{\mathbf{k}}_{\mathrm{F}}$, $\hat{\mathbf{k}}'_{\mathrm{F}}$ and $\hat{\mathbf{n}}$ follows

$$\hat{\mathbf{k}}'_{\mathrm{F}} = \left(2\cos\theta_{\mathrm{F}} \cdot \hat{\mathbf{n}}\right) - \hat{\mathbf{k}}_{\mathrm{F}} . \tag{27}$$

Knowing $\hat{\mathbf{k}}'_{\mathrm{F}}$ for each facet, we determined the polar angle θ'_{VD} characterizing the direction of the incident radiation from the scalar product of the vertical $\hat{\mathbf{z}}$ and the direction $\hat{\mathbf{k}}'_{\mathrm{F}}$

$$\cos\theta'_{\mathrm{VD}} = \hat{\mathbf{k}}'_{\mathrm{F}} \cdot \hat{\mathbf{z}} . \tag{28}$$

We assumed a flat horizon, meaning that facets with $\theta'_{\mathrm{VD}} \leq 90°$ are illuminated by the sky, whereas facets with $\theta'_{\mathrm{VD}} > 90°$ are obscured from the sky by the surrounding landscape. This yields the following expression for T_{in}

$$T_{\mathrm{in}} = \begin{cases} T_{\mathrm{sky}} & \text{for } \theta'_{\mathrm{VD}} \leq 90° \\ T_{\mathrm{eff}} & \text{for } \theta'_{\mathrm{VD}} > 90°. \end{cases} \tag{29}$$

For a facet to receive self-emission of ELBARA and reflect it back toward the antenna, the radiation incident on the facet must come from the direction of the radiometer. That means, $\hat{\mathbf{k}}_{\mathrm{F}} = \hat{\mathbf{k}}'_{\mathrm{F}} = \hat{\mathbf{n}}$ must be fulfilled, which was not the case for any facet.

When we knew the global facet reflectivities R^p_{RM} and T_{in} for each facet within the footprint area, we calculated the contributions $T^p_{\mathrm{B},f}$ (p = H, V) of all visible facets (numbered from $f = 1$ to n, whereas n denotes the total number of all visible facets) to the total radiation received by ELBARA with (3). When summing up these contributions $T^p_{\mathrm{B},f}$ to the total signal $T^p_{\mathrm{B,total}}$ received by ELBARA the directivity $D(\omega)$ of the antenna (ω = angle between $\hat{\mathbf{k}}_{\mathrm{RM}}$ and $\hat{\mathbf{k}}_{\mathrm{VD}}$, Fig. 2) has to be considered, as well as the fact that tilted surface facets appear enlarged or reduced in size, depending on the local incidence angle θ_{F} and the slope α of the facets (projection effect). The directivity pattern of the ELBARA antenna can be approximated by $D(\omega) = \exp(-0.01781 \cdot \omega^2)$ [27]. The projection effect is taken into account by means of the solid angle Ω under which a facet appears as seen from the antenna position

$$\Omega = A \cdot \frac{\cos\theta_{\mathrm{F}}}{r^2} = \frac{A^{\mathrm{h}}}{\cos\alpha} \cdot \frac{\cos\theta_{\mathrm{F}}}{r^2} \tag{30}$$

where A is the true area of the facet, $A^{\mathrm{h}} = (5 \times 5)$ cm^2 is the projection of A onto a horizontal plane, and r is the distance between the facet and the antenna. The slope α of the facet is the

same as the tilt angle between its surface normal $\hat{\mathbf{n}}$ and the vertical $\hat{\mathbf{z}}$, and is calculated from the scalar product as $\cos\alpha = \hat{\mathbf{z}}\cdot\hat{\mathbf{n}}$.

Now, the total signal at polarization p received by the radiometer antenna (the antenna brightness temperature) was calculated as the beam-weighted sum of the radiation $T_{\mathrm{B},f}^{p}$ from all visible facets within the footprint area

$$T_{\mathrm{B,total}}^{p} = \frac{\sum_{f=1}^{n} D_f T_{\mathrm{B},f}^{p} \Omega_f}{\sum_{f=1}^{n} D_f \Omega_f} . \tag{31}$$

Following this course of action, we calculated the time series of simulated brightness temperatures for the footprint areas A1 and A2 for all times, when radiometer measurements were carried out.

4 Results

In the following sections, we describe and discuss the measurement and simulation results. After a short overview of the meteorological conditions during the measurement campaign (Section 4.1), the simulated and measured soil moisture and temperature dynamics are discussed in Section 4.2. In Section 4.3, the geometrical characteristics relevant for the emission of the observed footprints are described, and then the process of the brightness temperature simulation is illustrated by means of a concrete example. In Section 4.4, we finally show the entire time series of simulated and measured brightness temperatures, and compare and discuss them in more detail for an illustrative time period in Section 4.5.

4.1 Meteorological Conditions

In the time period from September 2008 to December 2009, the meteorological station in the research catchment "Chicken Creek" recorded 778 mm of precipitation, which is close to the long-term average [21]. Several intense rainfall events occurred in autumn 2008, with the most intense rainfall on 29 and 30 October (40 mm in two days), while spring 2009 was very dry. During April and the first half of May, hardly any precipitation at all was recorded. The most intense rainfall events in summer 2009 were 20 mm on 1 July and 17 mm on 4 July, both within only one hour. Early autumn 2009 was again drier than in typical years.

Both winters (2008/09 and 2009/10) were colder than average. There was shallow snow cover for approximately half of the time from mid-November 2008 to the end of February 2009. On some days, however, only the gullies were filled with snow, while the other areas were almost bare. During the first half of January and the second half of February 2009, when most snow (5–10 cm) was observed, the footprint areas were entirely snow-covered, with large spatial deviations in snow depth due to wind drift. In winter 2009/10, partial snow cover was observed after 12 December.

4.2 Soil-Water Content and Temperature Dynamics

The *in situ* measurements of the soil water content *wc* were distinctly different for locations inside and outside the erosion gullies (Fig. 4). Inside the gullies, *wc* was generally higher, with little temporal change except for January and February 2009, when there was also substantial soil freezing (Fig. 5). Outside the gullies, *wc* showed much more short-term dynamics, clearly reflecting individual rainfall and snowmelt events, as well as the subsequent drying of the soil. The long rainless period in April and May 2009 illustrates this pattern particularly well.

The *wc* measurements within footprint A2 showed a rather narrow range of spatial variation and were similar to the measurements outside the erosion gullies elsewhere in the catchment (Fig. 4). This was expected as the soil surface had been initially leveled and there were no deep gullies in A2. In contrast, the five sensors in footprint A1 detected much more spatial variation since they represent areas inside as well as outside the gullies. The presence of gullies in A1 led to a higher mean *wc*. Nevertheless, one sensor specifically positioned at the bottom of a gully never reached the very high *wc* (≈ 0.4 m$^3 \cdot$m^{-3}) of the gullies elsewhere in the catchment, even though it recorded the highest *wc* in A1. This demonstrates that the *wc* in gullies can differ significantly depending on the amount of runoff, which is determined by the size, depth and location of the gully in question. The *wc* outside the gullies, however, seems to be more uniform.
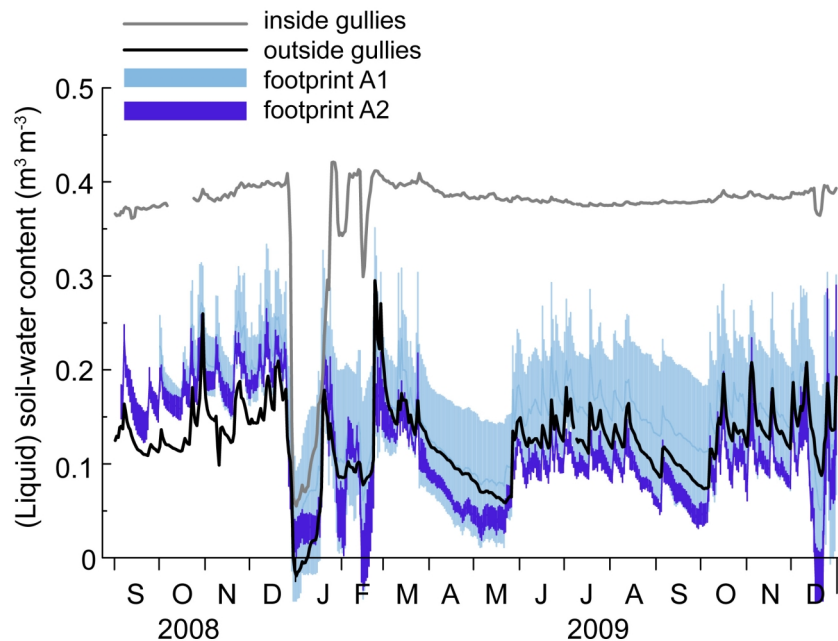
Fig. 4. Soil-water content measurements at a depth of 10–15 cm inside (gray line, mean of 5 sensors) and outside (black line, mean of 15 sensors) the erosion gullies. For the footprints A1 and A2, the spatial variation of the measurements is indicated by the pale blue area and the dark blue area (mean ± standard deviation), respectively. The very low and the apparently negative values in January, February and December 2009 are due to soil freezing.

After the calibration of the COUP model (Section 3.3), *wc* simulated for areas outside the gullies correlated very well with the corresponding measurements (Fig. 5a). An R^2-value of 0.65 and a root-mean-square error (*RMSE*) of 0.03 m$^3 \cdot$m^{-3} indicate that the model performance for these areas was excellent over the entire time period. From this generally good agreement between the simulated and measured *wc*, and given that the model was forced to match observed groundwater depth, it can be concluded that the chosen hydraulic properties of the uppermost soil layers are appropriate and that soil evaporation rates are well represented. The temporal variations of *wc* inside the gullies were somewhat overestimated by the model, whereas the absolute values were underestimated. The offset between the simulated and measured *wc* of approximately 0.1 m$^3 \cdot$m^{-3} represents the difference in saturation. This can either be an overestimation in the measurements, an underestimation in the model parameterization or a true difference between different gullies.

Soil temperatures T_s at the depth 10–15 cm were reproduced very well by the simulations (Fig. 5b). The excellent match between the measured and simulated T_s suggests that the surface energy balance and the vertical heat flux in the soil (which depends on *wc*, amongst other things) are appropriately simulated. The differences in T_s for areas inside and outside the gullies were very small and the correspondence between the simulations and the measurements was similar for both ($R^2 = 0.98$, *RMSE* = 1.14 K).

The satisfactory agreement of simulations and *in situ* measurements for the 10–15 cm soil layer suggests that these model results are a reasonable choice as input for the reflectivity and local radiative-transfer model (Section 3.4).
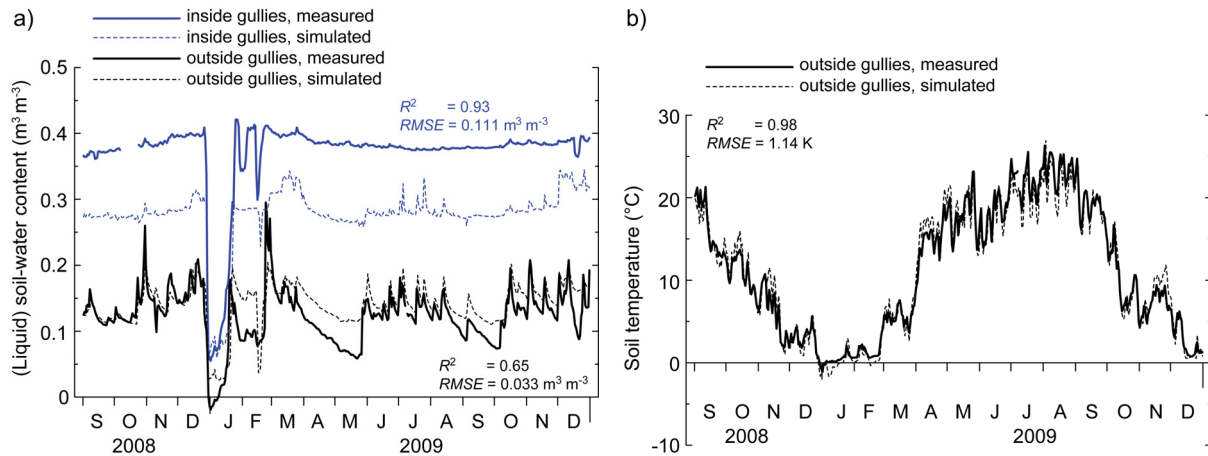
Fig. 5. a) Measured and simulated time series of soil-water content at a depth of 10–15 cm. For the measurements, the mean values of 15 sensors located outside the gullies (solid black line) and the mean values of five sensors representing typical gully locations (solid blue line) are displayed. b) Corresponding time series of soil temperatures for areas outside the gullies. Soil temperatures inside the gullies were very similar and are not shown for the sake of clarity.

4.3 Geometrical Footprint Characteristics and Exemplary Brightness Temperature Simulation

In Table II and Fig. 6, the most important geometrical parameters derived from the topography data of the footprints A1 and A2 and the viewing configuration of the radiometer are summarized. For the following discussion of these parameters, see also Fig. 8 which shows, amongst other things, the topography of both footprint areas.

The angles ϕ, ω and θ_{VD} describe the deviation of the VD-POI from the RM-POI for the different facets (Fig. 2). Since the topography measurements covered about the same fractions of both footprints, the ranges of ϕ, ω and θ_{VD} are approximately the same for A1 and A2. The angles α, θ_F and φ nicely illustrate the different surface characteristics (relief) of both areas, which are mainly caused by the erosion gullies in A1. Due to the steep gully slopes we see a much wider range of tilt angles α in A1 than in A2, which, in turn, leads also to a much wider distribution of facet elevation angles θ_F in A1. Low values of θ_F are mostly observed in gully slopes facing the radiometer, whereas slopes facing away from the radiometer usually exhibit values of θ_F larger than 90°. The range of θ_F encountered in A2, however, mainly resembles differences caused by the different locations of the individual facets within the footprint area. This is also illustrated by the fact that, in A2, the range of θ_F is not much larger than the range of θ_{VD}, whereas in A1 the difference between both is substantial. In accordance with these observations, the angle of polarization rotation φ spans the whole range between 0° and 90° in A1, but is always smaller than 40° in A2.

Table II. Geometrical parameters determining the emission behavior of the footprints A1 and A2 (Fig. 2). Numbers in parentheses show the respective values just for the facets visible for ELBARA.

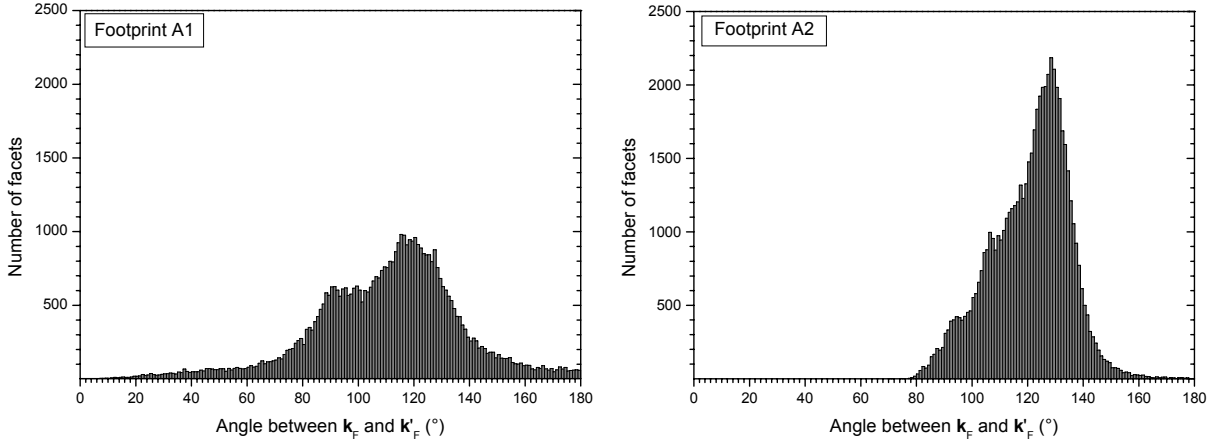|	footprint area	
	A1	A2
total number of facets / area of footprint	48529 / 121 m^2	60089 / 150 m^2
number of invisible facets	3077	99
number of facets in gullies	3666 (2546)	0
number of facets receiving radiation from the surrounding landscape	3466 (1619)	445 (380)
azimuth angle ϕ between $\hat{\mathbf{k}}_{RM}$ and $\hat{\mathbf{k}}_F$	$0° \leq \phi \leq 23°$	$0° \leq \phi \leq 21°$
polar angle ω between $\hat{\mathbf{k}}_{RM}$ and $\hat{\mathbf{k}}_F$	$0° \leq \omega \leq 19°$	$0° \leq \omega \leq 18°$
VD-elevation angle θ_{VD}	$36° \leq \theta_{VD} \leq 66°$	$39° \leq \theta_{VD} \leq 66°$
distance r between radiometer and facets	$13.18\ \text{m} \leq r \leq 25.26\ \text{m}$	$14.22\ \text{m} \leq r \leq 29.64\ \text{m}$
slope (tilt angle) α	$0° \leq \alpha \leq 75°$	$0° \leq \alpha \leq 43°$
local (facet) elevation angle θ_F	$1° \leq \theta_F \leq 127°$	$35° \leq \theta_F \leq 97°$
angle φ of polarization rotation	$0° \leq \varphi \leq 90°$	$0° \leq \varphi \leq 40°$
elevation angle θ'_{VD}	$1° \leq \theta'_{VD} \leq 179°$	$14° \leq \theta'_{VD} \leq 129°$

Fig. 6. Histograms of the angles between the view directions $\hat{\mathbf{k}}_F$, from the facets toward the radiometer, and $\hat{\mathbf{k}}'_F$, from the facets toward radiation T_{in} incident on the facets and reflected toward ELBARA. For footprint A1 (left), the smallest angle is 2°, and for A2 (right), all angles are larger than 71°.

Due to the erosion gullies in A1, about 6% of the facets in this area (mainly situated in gully slopes facing away from the radiometer) were "invisible" for ELBARA, whereas in A2 basically all facets were visible. Furthermore, we observed a much wider range of elevation angles θ'_{VD} of the radiation incident on the facets in A1 than in A2. This is also illustrated by Fig. 6, which gives the histograms of the angles between $\hat{\mathbf{k}}_F$ and $\hat{\mathbf{k}}'_F$ ($= 2\theta_F$) for both footprints. For A2, the distribution is concentrated between 80° and 160°, with the maximum at about 130°, whereas in A1 the distribution spans a much wider range, with the maximum at about 120°. However, the smallest angle observed is 2°, i.e. no facet reflects self-emission of ELBARA back toward the radiometer.

To illustrate the calculation process described in Section 3 and Fig. 3, we show the detailed results of a brightness temperature simulation for one single time step (23 April 2009, 9:12 a.m.) in Fig. 7 and 8. At that time, the effective temperature $T_{eff} = 11.7$ °C was approximately the same everywhere within both footprint areas, whereas the soil moisture difference for areas inside and outside the erosion gullies was at a maximum. The soil-water content of the 10–15 cm soil layer (taken from the simulated wc profile used as input to the local reflectivity model) was $wc = 0.27$ m$^3 \cdot$m^{-3} inside and 0.14 m$^3 \cdot$m^{-3} outside the gullies. The air temperature was $T_{air} = 8.4$ °C.

Figure 7a shows the local facet reflectivities R_F^p (p = H, V; Section 3.4). The broken lines are the output of the coherent radiative-transfer model for observation angles between 0° and 90° for the wc profiles simulated for locations inside the gullies and the solid lines for those outside the gullies. From these, the R_F^p of the individual facets (dots) were derived by interpolating to the local facet elevation angles θ_F. For footprint A1, this yielded values $0.08 \leq R_F^H \leq 1$ and $0 \leq R_F^V \leq 1$ distributed along the broken as well as the solid lines for locations inside and outside the gullies, and covering the entire range of observation angles. For A2, however, the R_F^p ($0.13 \leq R_F^H \leq 0.97$, $0 \leq R_F^V \leq 0.92$) are distributed along the solid lines

only and span the much narrower range of observation angles $35° \leq \theta_F \leq 90°$. This is due to the absence of gullies in A2.

Panel b) shows the resulting facet reflectivities R_{RM}^p in the global (radiometer) reference frame, which were derived from R_F^p by considering the transformation from the F-POI to the RM-POI (Section 3.5). That means, both the tilt of the facets as well as the deviation of their view directions $\hat{\mathbf{k}}_F$ from the radiometer main direction $\hat{\mathbf{k}}_{RM}$ are considered in R_{RM}^p. The resulting reflectivities are $0.02 \leq R_{RM}^H \leq 1$ and $0 \leq R_{RM}^V \leq 0.99$ for A1, and $0.13 \leq R_{RM}^H \leq 0.97$ and $0 \leq R_{RM}^V \leq 0.89$ for A2. As expected, the difference between R_{RM}^p and R_F^p is more pronounced in footprint A1 as a result of the steeper slopes (tilt angles α) of some of the facets caused by the erosion gullies.

The brightness temperatures T_B^p of the facets shown in panel c) were calculated by inserting R_{RM}^p, together with the effective soil temperature T_{eff} and the incident radiation T_{in}, into (3) (Section 3.6). This yielded brightness temperatures $68.4 \text{ K} \leq T_B^H \leq 284.8 \text{ K}$ and $153.0 \text{ K} \leq T_B^V \leq 284.8 \text{ K}$ for A1, and $121.8 \text{ K} \leq T_B^H \leq 284.8 \text{ K}$ and $233.2 \text{ K} \leq T_B^V \leq 284.8 \text{ K}$ for A2. The constant values $T_B^p = 284.8 \text{ K}$ for different θ_F in A1 and A2 are the brightness temperatures of facets receiving radiation from the surrounding landscape, which are identical with the surrounding's effective temperature T_{eff}. From the convolution of the facets' radiances T_B^p with the antenna pattern, we eventually received the simulated brightness temperatures $T_B^H = 223.5 \text{ K}$ and $T_B^V = 275.0 \text{ K}$ for footprint A1, and $T_B^H = 206.9 \text{ K}$ and $T_B^V = 281.9 \text{ K}$ for footprint A2. The corresponding measurement results were $T_B^H = 239.9 \text{ K}$ and $T_B^V = 277.7 \text{ K}$ for A1, and $T_B^H = 214.5 \text{ K}$ and $T_B^V = 279.0 \text{ K}$ for A2.

Figure 8 gives a spatial representation of the facets' brightness temperatures T_B^p shown in Fig. 7c. The T_B^p's of the individual facets were overlain on the digital elevation model of the corresponding footprint to give an impression of the dependence of the T_B^p on the facets' location within the footprint, on the one hand, and the tilt of the facets, on the other. In both footprints, we see a decrease (p = H) or increase (p = V) in the direction away from ELBARA (toward the right) for facets situated outside the erosion gullies. This change in the facets' T_B^p corresponds to the differing local elevation angles θ_F of these facets, which range roughly from 40° (left) to 70° (right). At vertical polarization, T_B^V actually starts to decrease again for large θ_F exceeding the Brewster angle at approximately 65° (see Fig. 7c), which can be observed to some extent in the illustration for A2. At the bottom of the erosion gullies, we find T_B^p are colder than the surroundings at both polarizations, as a result of the generally higher water contents within the gullies. The facet elevation angles θ_F of the gully slopes facing the radiometer (toward left) are approximately in the range $10° \leq \theta_F \leq 30°$, resulting in rather high (p = H) and low (p = V) values, respectively, for the T_B^p's of these slopes. For most of the slopes facing away from the radiometer (toward the right), θ_F is larger than 60°. This leads to significantly colder T_B^H and slightly warmer T_B^V than in the surroundings. However, due to their steepness, most of these slopes receive radiation from the surrounding landscape (i.e., $T_{in} = T_{eff}$ in (3)) and were therefore assigned $T_B^p = T_{eff}$, corresponding to the highest T_B^p within both areas.
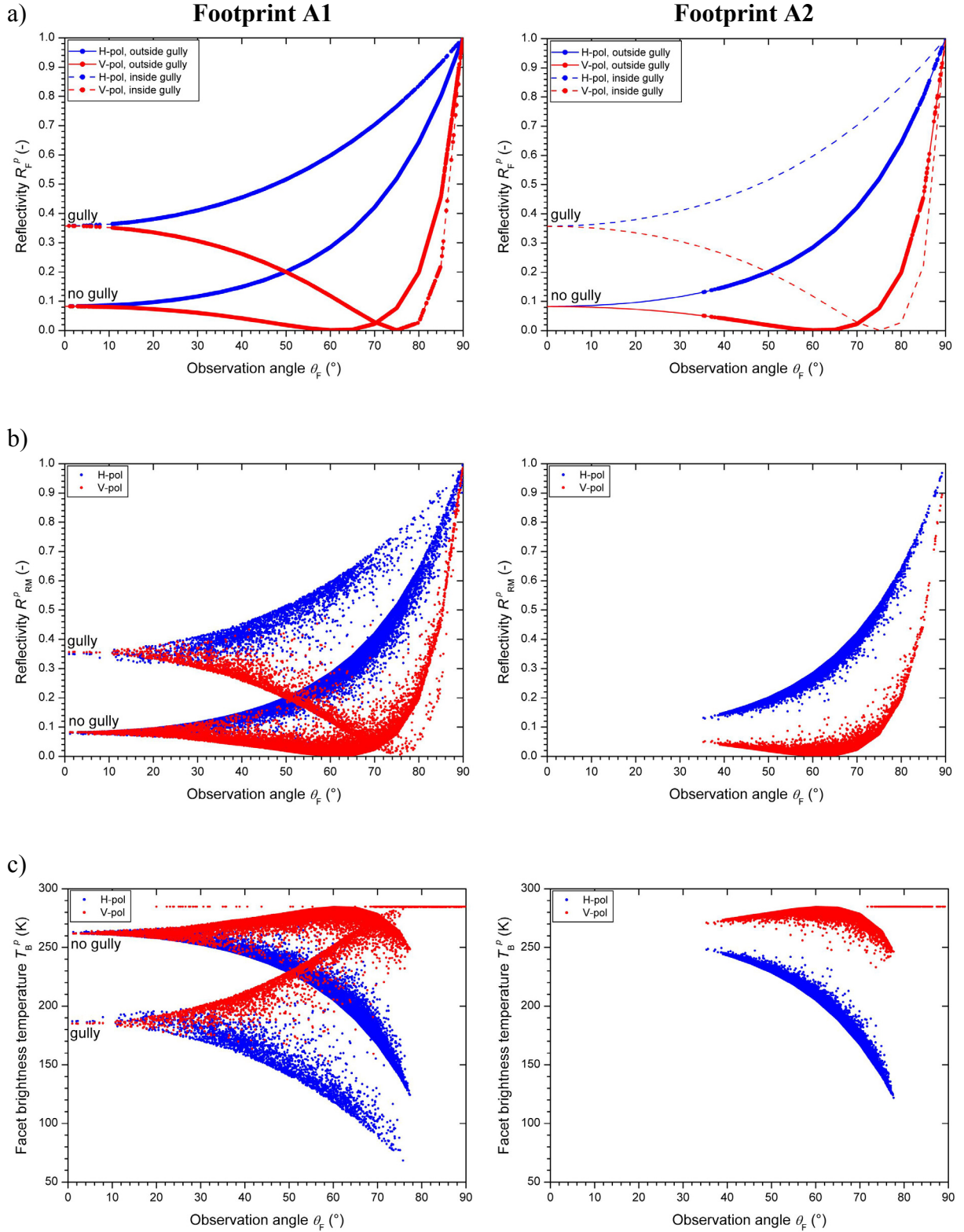
Fig. 7. Calculation results of the facet model for 23 April 2009, 9:12 a.m. for footprints A1 (left) and A2 (right). a) Reflectivities calculated with the coherent radiative-transfer model for observation angles between 0° and 90°, based on the simulated soil-water contents for locations inside (broken lines) and outside the gullies (solid lines). Dots show the local facet reflectivities R_F^p (p = H, V) derived by interpolating these look-up tables to the facet elevation angles θ_F. b) Global facet reflectivities R_{RM}^p for $0° \leq \theta_F \leq 90°$. c) Brightness temperatures T_B^p of the facets for $0° \leq \theta_F \leq 90°$, calculated with (3) from R_{RM}^p, the effective soil temperature T_{eff} and the incident radiation T_{in}.

Footprint A1
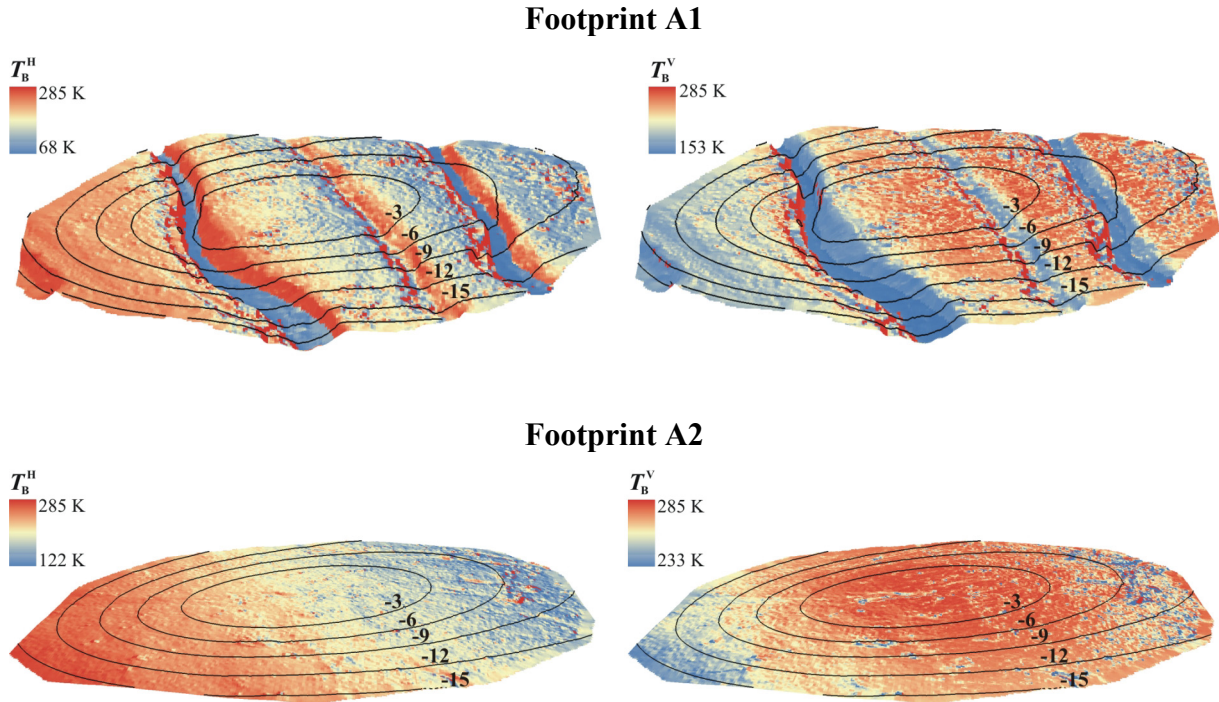
Footprint A2

Fig. 8. Spatial distribution of facet brightness temperatures T_B^p (p = H, V) for the footprints A1 (top) and A2 (bottom), at horizontal (left) and vertical polarization (right). Brightness temperatures were overlain on the digital elevation models of the footprints, which are shown so that the view direction toward ELBARA (situated to the left and above) is approximately the same for both. The isolines show the antenna pattern of the ELBARA antenna in dB. The areas shown are approximately 15 m × 11 m for A1, and 17 m × 11 m for A2, measured along the lines of greatest distance.

4.4 Brightness Temperature Time Series

Brightness temperatures T_B^p (p = H, V) of both footprint areas were simulated for all times of radiometer measurements with the facet model described in Section 3. The complete time series of T_B^p measured and simulated for the time period between September 2008 and December 2009 is shown in Appendix B. Furthermore, air temperature, effective soil temperature, snow coverage, modeled and measured soil-water content and precipitation are also given. Below, we first describe the general behavior of the measured and simulated T_B^p, before they are directly opposed to each other in Section 4.4.3. A more specific discussion of the measurement and simulation results on the basis of an illustrative time period is presented in Section 4.5.

4.4.1 Measured Brightness Temperatures

The brightness temperatures T_B^p measured (Appendix B, top panel) clearly reflect the weather and soil conditions prevailing at the time of the measurements. First of all, the T_B^p follow the dynamics of the effective soil temperature T_{eff}, which in turn is correlated with the air temperature T_{air}. This is most obvious in the diurnal changes in T_B^p, corresponding to the daily fluctuations of T_{eff} and T_{air}. Furthermore, T_B^p were generally lower in winter than in summer, reflecting the seasonal fluctuations of T_{eff} and T_{air}.

Superimposed on this underlying trend are miscellaneous weather events, such as precipitation and soil frost. Of course, precipitation leads to an increase in soil-water content wc shortly after the onset of precipitation, which, in turn, results in a sudden drop in the T_{B}^{p}. After precipitation stops, the T_{B}^{p} subsequently start to increase again. Initially, this happens quite fast as the surface runoff stops and the uppermost soil layers dry out. This is then usually followed by a more gradual increase related to the subsequent drying of the deeper soil. This behavior is especially pronounced after longer rainless periods, when the soil is dry prior to the onset of precipitation, such as at the end of April 09 or in the first week of September 09.

Intense soil frost, e.g. at the end of the year 08, leads to a sudden loss of liquid wc as the water in the soil-pore spaces freezes (lower two panels). This, in turn, results in a sharp increase in the T_{B}^{p}, which can be seen, e.g. on 25 December 08. Quite often this sudden increase is followed by an abrupt drop in the T_{B}^{p}, when the frost period is only of short duration and the soil thaws again. Several nice examples of such sharp spikes in the T_{B}^{p} can be seen, e.g. on 9 December 08 or 25 March 09.

The situations hardest to interpret are times, when snow, rain, soil freezing and thawing all occur within a short time period. This leads to a constant change in wc conditions as precipitation sometimes falls as snow and sometimes as water, snow melt leads to infiltration and an increase in wc, whereas soil freezing decreases the liquid wc again. This, in turn, results in very heterogeneous soil (surface) properties and highly complex temporal changes in the T_{B}^{p}, such as those that occurred in January and February 09.

Comparing the T_{B}^{p} of the footprints A1 (with gullies) and A2 (without gullies) with each other, we see distinct differences. At vertical polarization, $T_{\mathrm{B}}^{\mathrm{V}}$ is generally lower in A1 than in A2, with a mean difference of $\Delta \overline{T}_{\mathrm{B}}^{\mathrm{V}} = 4.4 \text{ K}$ [5] (Table III). However, the difference $\Delta T_{\mathrm{B}}^{\mathrm{V}}$ is rather variable with time. It is usually more pronounced, when the soil is moist and $T_{\mathrm{B}}^{\mathrm{V}}$ is low (e.g., from 16 to 25 December 08), and is small or even approaching 0 K, when the soil is dry and $T_{\mathrm{B}}^{\mathrm{V}}$ is high (e.g., in April 09). In A1, $T_{\mathrm{B}}^{\mathrm{V}}$ is usually more sensitive to changes in wc and T_{eff} and to the occurrence of soil frost or snow melt than it is in A2. That means, on the one hand, that the decrease in the $T_{\mathrm{B}}^{\mathrm{V}}$ with increasing wc is often more pronounced in A1 than in A2, resulting in a larger $\Delta T_{\mathrm{B}}^{\mathrm{V}}$ after precipitation and snow melt or when the soil is moist (e.g., on 6 October 08 or 23 April 09). On the other hand, with decreasing wc due to soil drying or freezing, $T_{\mathrm{B}}^{\mathrm{V}}$ in A1 increases more than in A2, and $\Delta T_{\mathrm{B}}^{\mathrm{V}}$ becomes smaller. When the soil is very dry, $\Delta T_{\mathrm{B}}^{\mathrm{V}}$ eventually approaches 0 K and both areas show almost identical $T_{\mathrm{B}}^{\mathrm{V}}$ (e.g., during the dry spell in April 09).

At horizontal polarization, $T_{\mathrm{B}}^{\mathrm{H}}$ is almost always higher in A1 than in A2, with a mean difference of $\Delta \overline{T}_{\mathrm{B}}^{\mathrm{H}} = 25.8 \text{ K}$ (Table III). The difference $\Delta T_{\mathrm{B}}^{\mathrm{H}}$ does not change as obviously in response to changing ambient conditions as was the case at $p = \mathrm{V}$, making it more challenging

---

[5] For the following discussion we introduce the term $\Delta T_{\mathrm{B}}^{p} = \left| T_{\mathrm{B,A1}}^{p} - T_{\mathrm{B,A2}}^{p} \right|$ ($p = \mathrm{H, V}$) describing the difference between the brightness temperature $T_{\mathrm{B,A1}}^{p}$ of A1 and the brightness temperature $T_{\mathrm{B,A2}}^{p}$ of A2. The mean difference is given by $\Delta \overline{T}_{\mathrm{B}}^{p} = \left| \overline{T}_{\mathrm{B,A1}}^{p} - \overline{T}_{\mathrm{B,A2}}^{p} \right|$, where $\overline{T}_{\mathrm{B,A1}}^{p}$ and $\overline{T}_{\mathrm{B,A2}}^{p}$ are the mean values of the brightness temperatures measured in the respective footprints.

Table III. Comparison of the mean values $\overline{T}_B^p$ (p = H, V) of the footprints A1 and A2 for measurements (left) and simulations (right) for the time period between 1 October 2008 and 13 August 2009, when both footprint areas were measured quasi-simultaneously. The number of data-points evaluated for A1 and A2 are given in parentheses.

measurements	A1 (30655)	A2 (11076)	A1 − A2	simulations	A1 (30655)	A2 (11076)	A1 − A2
$\overline{T}_B^H$ (K)	200.6	174.8	25.8	$\overline{T}_B^H$ (K)	199.1	181.7	17.4
$\overline{T}_B^V$ (K)	260.0	264.4	−4.4	$\overline{T}_B^V$ (K)	261.4	272.1	−10.7
$\overline{T}_B^V - \overline{T}_B^H$ (K)	59.4	89.6		$\overline{T}_B^V - \overline{T}_B^H$ (K)	62.3	90.4	

to interpret temporal changes in ΔT_B^H. Only in March and April 09 do T_B^H behave distinctly different in both areas. In that time period, T_B^H in A1 responds more strongly to changing T_{eff} (e.g., on 5 March 09) and precipitation (e.g., on 19 and 23 March 09), and increases faster and more distinctly with decreasing wc in combination with increasing T_{eff} (29 March to 12 April 09). In general, the response of T_B^H to changes in ambient conditions is faster and slightly more distinct in A1 than in A2, whereas the difference in the behavior of both areas is not as pronounced as at p = V. Contrary to what was observed at p = V, the T_B^H of both areas do not approach each other with decreasing wc.

From the fact that T_B^p of A1 are usually larger than those of A2 at p = H, but lower at p = V, it follows that the difference between the brightness temperatures of both polarizations is usually smaller in A1 than in A2. This is confirmed, when the mean differences $\overline{T}_B^V - \overline{T}_B^H$ of both areas are compared (Table III).

4.4.2 Simulated Brightness Temperatures

The general behavior of the T_B^p in response to changing ambient conditions was reproduced well with the simulations. In the simulated T_B^p (Appendix B, second panel), we also see the daily and seasonal fluctuations associated with the corresponding changes in T_{eff} and T_{air}. The sudden decrease in the T_B^p with precipitation and increasing wc, and the subsequent, more gradual increase in the T_B^p during the drying of the soil were also reproduced well. However, the rate of this increase differs sometimes for simulations and observations. This is especially obvious during the dry spell in April 09 at p = H. In that time period, the simulated T_B^p furthermore start to decrease again with advancing soil drying, while the measured T_B^p still increase, or at least remain stable. This phenomenon is observed at both polarizations, but is much more pronounced at p = H, and is possibly a response to decreasing T_{eff}. The reaction of T_B^p to soil freezing was reproduced very well with the simulations. The largest deviations between the simulation results and the measurements are observed between 14 January and 26 February 09. As already mentioned in Section 4.4.1, the interpretation of this time period is difficult since ambient and soil conditions constantly change in a highly complex manner. Due to this, it is furthermore expected that soil conditions (T_{eff}, wc) for this period were not as well simulated by the COUP model as those for other times.

The differences ΔT_B^p between the brightness temperatures of both areas were reproduced reasonably well by the simulations. At $p = $ V, simulated T_B^V are always lower in A1 than in A2, and at $p = $ H, simulated T_B^H for A1 always exceed those of A2, whereas the mean difference $\Delta \overline{T}_B^p$ is more pronounced at $p = $ H. However, the absolute values of $\Delta \overline{T}_B^p$ were somewhat underestimated at $p = $ H ($\Delta \overline{T}_B^H = 17.4$ K) and overestimated at $p = $ V ($\Delta \overline{T}_B^V = 10.7$ K), compared to the measurements (Table III). The mean differences $\overline{T}_B^V - \overline{T}_B^H$ for both areas agree very well with the values obtained from the measurements.

The response of the simulated T_B^p to changing ambient conditions does not differ as significantly between the two areas as it does in the measured T_B^p. Nevertheless, at vertical polarization, the T_B^V of both areas behave similarly to what was observed in the measurements, and the temporal change in ΔT_B^V was reproduced reasonably well. At horizontal polarization, the simulated T_B^H of the two areas behave quite similarly and ΔT_B^H does not change significantly with time.

4.4.3 Evaluation of the Simulation Results

To illustrate the model performance, scatter plots with the simulated and measured brightness temperatures and histograms of the corresponding residuals are shown in Fig. 9 for footprint A1 (with gullies) and for A2 (without gullies) in Fig. 10. Additionally, the bias B of the simulations, the root-mean-square error $RMSE$, and the coefficient of determination R^2 (calculated as the square of Pearson's product-moment correlation coefficient) are given in Table IV. Furthermore B, $RMSE$ and R^2 for simulations, where the footprint areas were approximated by tilted planes fitted through the digital elevation model of the respective footprint, are shown.

The overall agreement of the measurement and simulation results is better at vertical than at horizontal polarization and better for footprint A1 than for A2 (Table IV). On average, simulations for A1 slightly underestimated measurements at horizontal polarization ($B = -1.4$ K), but slightly overestimated measurements at vertical polarization ($B = 1.4$ K). For footprint A2, simulated T_B^p exceeded measurements on average at both polarizations with a bias of 6.9 K at $p = $ H and 7.7 K at $p = $ V. The $RMSE$ of the simulations is generally smaller at $p = $ V than at $p = $ H, and is larger for A2 than for A1 at both polarizations. The temporal dynamics of the T_B^V at vertical polarization were simulated well for both areas, as indicated by the high R^2-values of 0.81 for A1 and of 0.78 for A2. At horizontal polarization, the simulation results were somewhat less accurate in this regard, with R^2-values of still 0.69 for A1, but only 0.54 for A2.

In accordance with the above, the data tuples in the scatter plots of A1 (Fig. 9) are more closely distributed around the 1:1 line than the data tuples in the scatter plots of A2 (Fig. 10). Furthermore, the frequency distributions of the residuals are centered approximately around 0 K for A1, but shifted somewhat toward positive values for A2, corresponding to the larger biases of these simulations. Additionally, the distributions of the residuals are much closer to a normal distribution at vertical polarization than at horizontal polarization. This indicates that

Fig. 9. Scatter plots of measured versus simulated brightness temperatures T_B^p (top), and histograms of the corresponding residuals (bottom) for footprint A1. Panel a) is for horizontal polarization, and panel b) is for vertical polarization.
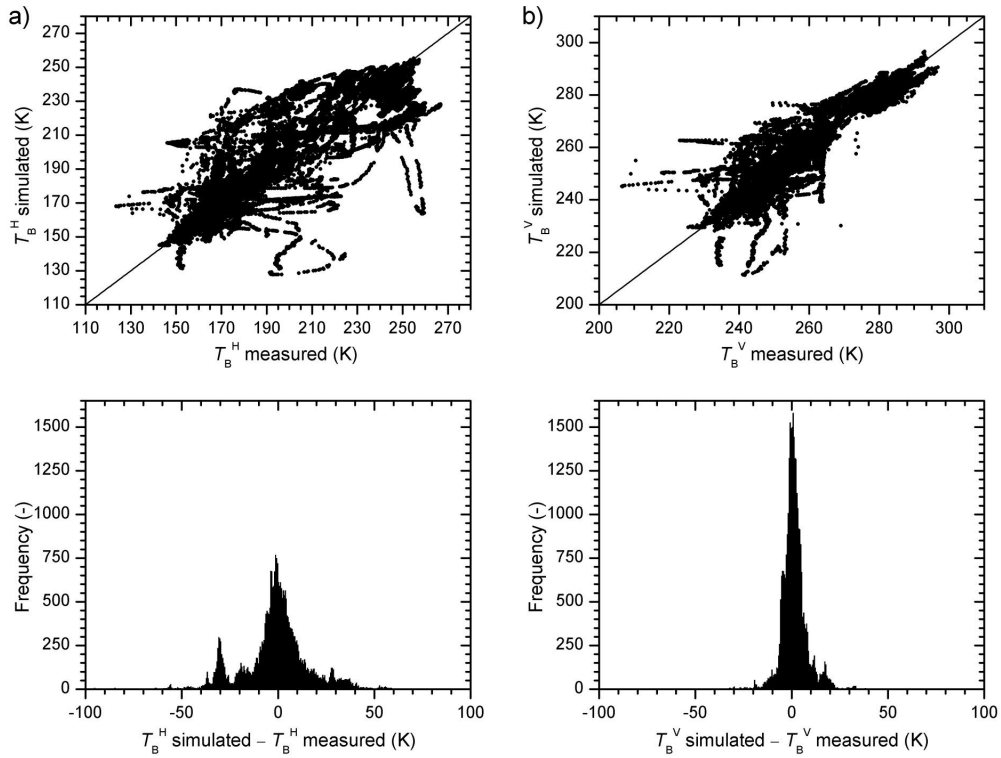

Fig. 10. Scatter plots of measured versus simulated brightness temperatures T_B^p (top), and histograms of the corresponding residuals (bottom) for footprint A2. Panel a) is for horizontal polarization, and panel b) is for vertical polarization.
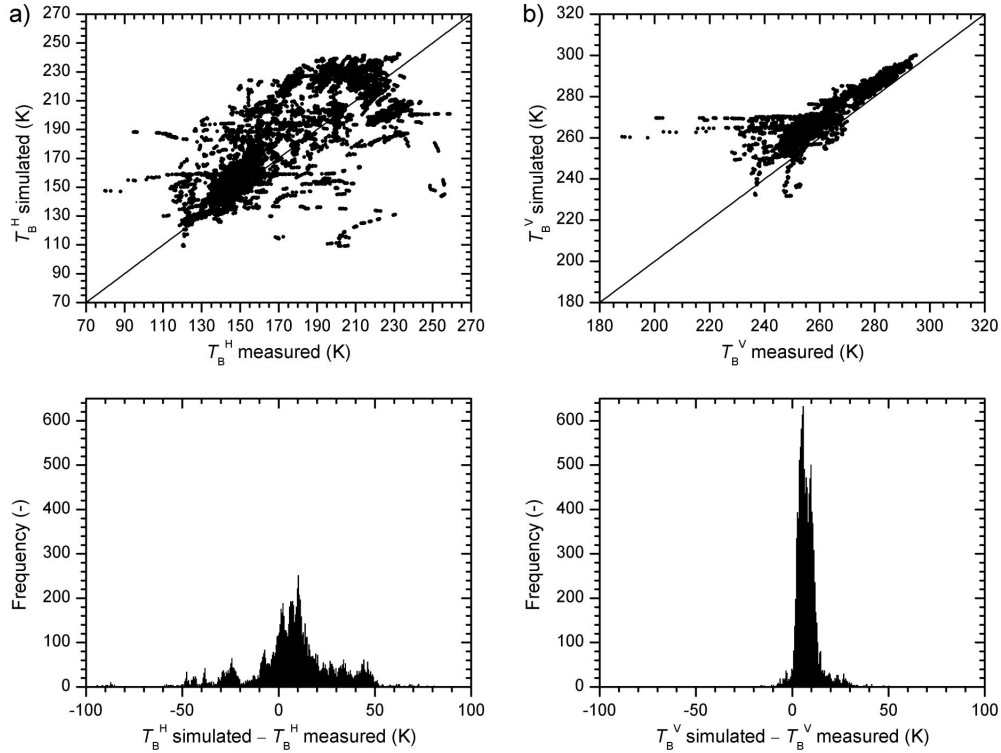
Table IV. Bias B, root-mean-square error $RMSE$ and coefficient of determination R^2 for the brightness tempera-
ture simulations for footprints A1 and A2.

Footprint	horizontal polarization			vertical polarization		
	B (K)	$RMSE$ (K)	R^2	B (K)	$RMSE$ (K)	R^2
A1[a]	−1.4	17.9	0.69	1.4	6.8	0.81
A2[a]	6.9	24.5	0.54	7.7	9.9	0.78
A1[b]	−7.9	20.2	0.69	8.9	11.0	0.82
A2[b]	6.0	24.4	0.54	8.7	10.7	0.78

[a] simulations with measured footprint topography
[b] simulations with footprints approximated by simple, tilted planes

simulation errors at $p = $ V are more of a random nature, whereas at $p = $ H, there may be proc-
esses that are not adequately represented by the model used.

To test whether the observed differences between the brightness temperatures of both areas
can be attributed to relief effects, we performed additional simulations in which the footprint
areas were approximated by simple planes fitted to the measured footprint topographies. This
led to a significant deterioration in the simulation results for A1. This is most obvious in the
much larger biases B, but the $RMSE$ also increased at both polarizations (Table IV). However,
the R^2-values were almost the same as before, indicating that the temporal changes in the T_B^p
were simulated with approximately the same quality. Approximating A2 by a simple plane
yielded almost identical results as the simulations with the measured topography. This is not
surprising and confirms our supposition that, due to the lack of erosion gullies, this area can
be considered to be radiometrically smooth.

4.5 Brightness Temperatures of an Illustrative Time Period

Figure 11 shows the measurement and simulation results for the time period from 23
March to 1 May 2009, when several typical weather conditions occurred, making it ideally
suited to investigate process-driven brightness temperature variations. The first two days of
this time period were rainy and cold, and were then followed by a short frost event with sub-
stantial soil freezing. Afterwards, there was no significant precipitation for five weeks, and it
gradually became warmer, resulting in an extended drying period for the soil. This dry spell
was interrupted by only two rainfall events, which differed in duration as well as in the
amount of precipitation. At the end of this period, dry and warm conditions prevailed.

The two topmost panels in Fig. 11 show the T_B^p measured and simulated for footprints A1
(with gullies) and A2 (without gullies). To allow for an easy comparison of the simulation and
measurement results, the T_B^p measured and simulated for each footprint are plotted in the
same panel, unlike in Appendix B! Additionally, the special events discussed below are
indicated by consecutive numbers. The third panel shows air temperature T_{air} and effective
soil temperature T_{eff}. The light blue and the blue lines in the lowermost panel indicate the
results of the soil-water content wc simulations with the COUP model for areas outside and
inside the erosion gullies, respectively, for two different soil depths (dotted line: 0–3 cm,

solid line: 10–15 cm). The gray shaded area illustrates the range mean ± standard deviation of the ten *in situ wc* sensors in A1 and A2. The blue bars indicate the precipitation *P*.

4.5.1 Measured Brightness Temperatures

The brightness temperatures observed during this time period demonstrate the daily T_B^p variations due to the diurnal cycle of temperature and solar irradiation particularly well. However, the focus here is not on these diurnal oscillations, and when we refer to T_B^p changes below, we mean either the rapid changes in T_B^p due to short-term changes in ambient conditions (e.g., the onset of precipitation) or to the rather long-term trends in T_B^p due to more gradual changes, such as soil drying.

The steady but moderate rainfall on 23 and 24 March (11 mm in two days) resulted in an increase in the soil-water content *wc*, which was noticeable in the measurements as well as in the simulations ①. This increase in *wc*, accompanied by declining temperatures, led to a decrease in T_B^p, which was somewhat more pronounced for A1 than for A2 at both polarizations (see also Appendix B, p. 87, where the T_B^p of both footprint areas are plotted in the same panel).

In the night of 24 to 25 March, air temperature T_{air} dropped below 0 °C and soil temperature T_{eff} reached the freezing point ②. This resulted in a brief soil frost, causing a pronounced decrease in the liquid *wc* measured and in the *wc* simulated for the uppermost soil layer. It does not, however, show in the *wc* simulated for the 10–15 cm soil layer. Brightness temperatures abruptly increased, when the soil froze, and then suddenly decreased again, when the soil thawed. At *p* = V, this change was more pronounced in A1, so that the T_B^V of A1 almost reached those of A2 during freezing and became distinctly different again afterwards. At *p* = H, the change in the T_B^H associated with soil freezing was, however, more pronounced in A2.

Another 3 mm of precipitation fell over the three days following the frost event, and then a long, rainless period began, which lasted for several weeks ③. During this dry spell, the T_B^p of both areas gradually increased with decreasing *wc* and rising temperatures. However, at *p* = V, the initial increase (26 to 31 March) was somewhat greater in A1 than in A2, so that the T_B^V of both areas approached each other. After 31 March, the T_B^V of both areas were almost identical for about three weeks ($\Delta T_B^V \leq 3\,\mathrm{K}$). At *p* = H, the initial increase in T_B^H was faster and more pronounced in A1 also, resulting in a larger difference ΔT_B^H between the brightness temperatures of both areas. After 8 April, however, the T_B^H of A1 remained approximately stationary, whereas the T_B^H of A2 was still increasing. Just before the faint rainfall on 17 April, the difference ΔT_B^H was approximately the same again as at the beginning of the dry spell.

The rainless period ended with very slight rainfall (0.4 mm in 1 h) on 17 April, which is not visible in the simulated or measured *wc* ④. Nevertheless, it led to a noticeable drop in T_B^p. This decrease is more obvious at *p* = H than at *p* = V, and more pronounced in A1 than in A2 at both polarizations. The same general behavior was observed after the more intense rain on 23 April (3 mm in 2 h), but the decrease in the T_B^p was much larger ⑤. As a result of the more

pronounced decrease in the brightness temperatures in A1, the $T_{\mathrm{B}}^{\mathrm{V}}$ of both areas differed distinctly again after the rainfall, whereas the $T_{\mathrm{B}}^{\mathrm{H}}$ of both areas approached each other. Interestingly, this rainfall was still not visible in the measured *wc*. Also the *wc* simulated for the 10–15 cm soil layer outside the gullies did not change noticeably, whereas the simulations for the uppermost soil layer show a strong increase in *wc* outside the gullies. This indicates that infiltration rates were low and surface runoff pronounced, which is typical for this soil [21]. Soil-water content simulations for gullies showed a very small increase for both depths.

In the days that followed ⑥, the behavior of the T_{B}^{p} was similar to that observed prior to the rainfalls. During the last days of April, the $T_{\mathrm{B}}^{\mathrm{V}}$ of both areas were identical again, whereas the $T_{\mathrm{B}}^{\mathrm{H}}$ of the two areas differed in approximately the same way as at the beginning of the dry spell.

4.5.2 Simulated Brightness Temperatures

The decrease in brightness temperatures due to the rainfall on 23 and 24 March was also observed in the simulations, but was partly overestimated, especially for footprint A1 ①.

The subsequent frost event on 24 and 25 March is represented very well in the simulations ②. Both the sudden increase in the T_{B}^{p} associated with soil freezing and the following decrease, when the soil thawed again, are represented in the simulated T_{B}^{p}. At $p = \mathrm{V}$, the increase in brightness temperatures was more pronounced in A1, and at $p = \mathrm{H}$, it was more pronounced in A2. Consequently, the $T_{\mathrm{B}}^{\mathrm{V}}$ of both areas were almost identical during freezing and the $T_{\mathrm{B}}^{\mathrm{H}}$ of both areas converged, as the measurements also showed (see also Appendix B, p. 87). The onset of the sudden T_{B}^{p} increase, however, is somewhat delayed compared to the measurements (except for $T_{\mathrm{B}}^{\mathrm{V}}$ of A2). Probably the beginning of soil freezing and the ensuing decrease in the liquid *wc* was slightly missed by the simulations of T_{eff} and *wc*, possibly as a result of the hourly time intervals in the COUP simulations. The subsequent drop in the T_{B}^{p} associated with the thawing of the soil and the renewed increase in *wc* was underestimated in all cases. As a result, the T_{B}^{p} simulated for A1 and A2 were distinctly larger than the measured T_{B}^{p} at the beginning of the dry spell.

During the long rainless period, the simulations and measurements for A1 correspond remarkably well ③. Especially at $p = \mathrm{V}$, simulated $T_{\mathrm{B}}^{\mathrm{V}}$ matches the measurements very well. At $p = \mathrm{H}$, the increase in the simulated $T_{\mathrm{B}}^{\mathrm{H}}$ slightly lags behind the measurements initially (30 and 31 March), and is overestimated compared to the later measurements (1 to 6 April). This change from under- to overestimation coincides with the abrupt drop in the *wc* simulated for the uppermost soil layer outside the gullies. This implies that the initial decline in *wc* is underestimated, whereas the following drying of the uppermost soil happens too fast in the COUP simulations. This is further corroborated by the fact that after 6 April, the simulated $T_{\mathrm{B}}^{\mathrm{H}}$ remained approximately stationary, whereas $T_{\mathrm{B}}^{\mathrm{H}}$ measured was still rising. This is probably due to a more gradual drying of the uppermost soil than was simulated.

In footprint A2, the overall behavior of the simulated T_{B}^{p} during the dry spell is the same, but the differences between the measurements and simulations are more distinct than in A1. The simulated brightness temperatures already exceeded the measured T_{B}^{p} at the beginning of
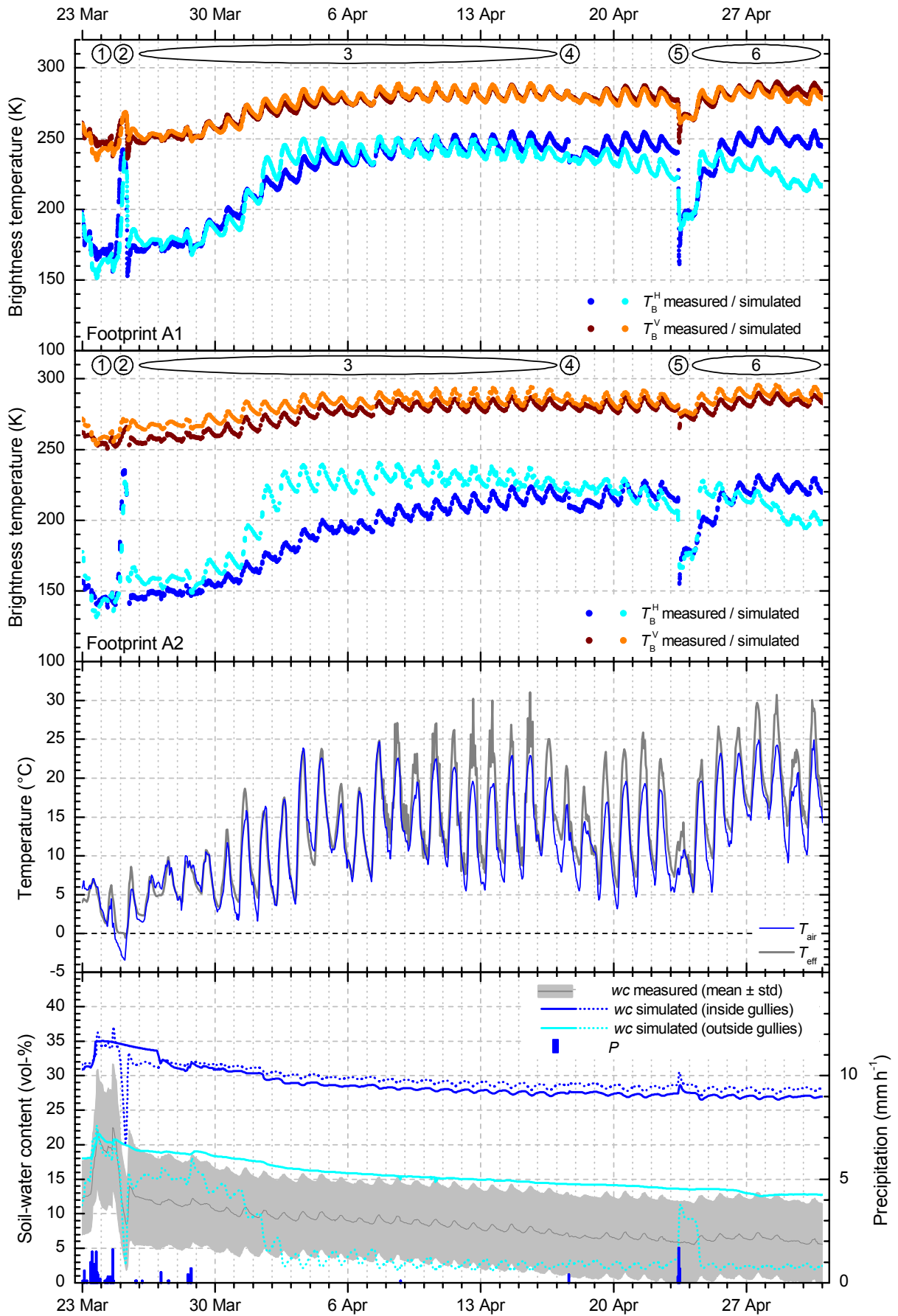
Fig. 11. Measurement and simulation results for the time period from 23 March to 1 May 2009 (refer to the text for a detailed description of the different symbols).

the dry spell, mainly still because the simulated values after the frost event were too high. Furthermore, the overestimation of the T_B^H increase after 31 March is even more pronounced in A2, leading to a large deviation between the measured and simulated T_B^H. After 6 April, simulated and measured T_B^p converged again as a result of the same behavior already observed for A1. Measured T_B^p still increased, whereas simulations remained approximately stationary or even started to decrease again after 13 April (possibly in response to decreasing soil temperatures).

The slight rainfall on 17 April is not visible in the simulations at $p = \mathrm{V}$, and only barely perceptible at $p = \mathrm{H}$ ④. After the rain, the same behavior as before is observed. The simulated T_B^p decreased further unlike the measured T_B^p, which remained approximately stable at $p = \mathrm{V}$ and increased slightly at $p = \mathrm{H}$. The stronger rainfall on 23 April led to a distinct increase in the simulated wc for the uppermost soil layer, unlike after the rainfall on 17 April, and a considerable drop in the simulated T_B^p ⑤. In both footprints, however, the T_B^p decrease is distinctly underestimated and the subsequent renewed increase is overestimated compared to the measurements. This indicates an initial underestimation of the wc increase near the surface (and possibly surface runoff) after precipitation, which is then followed by too fast soil drying in the COUP simulations.

In the last week of April, simulated T_B^p remained approximately stable at $p = \mathrm{V}$, and decreased distinctly in both areas at $p = \mathrm{H}$ ⑥. At the end of the time period considered, the simulations and measurements agree well for T_B^V, whereas the simulated T_B^H significantly underestimate the measured T_B^H. The decrease in the simulated T_B^H starts just after the abrupt drop in the wc simulated for the uppermost soil layer on 24 April, and then continues until the end of the example period, even though the simulated wc remained approximately constant after 25 April. This behavior cannot be explained conclusively. One possible reason is that the rate of soil surface drying is overestimated in the COUP simulations, and since the emission depth increases with decreasing wc, the contributions of the deeper and moister soil layers to the total emission gain in importance. This can lead to smaller T_B^p in consequence. Furthermore, coherent effects are probably overestimated in the simulations since the soil is represented by a perfectly layered, vertical profile in the model.

The differences in the behavior of the T_B^p of both areas were reproduced reasonably well with the simulations (see Appendix B, p. 87). At vertical polarization, T_B^V of A1 showed a stronger reaction in response to changing wc, which is especially obvious during the soil-frost event ② and after the rainfall ⑤. This behavior was observed in the measurements as well, and indicates pronounced polarization mixing in A1 as a result of the distinct relief (gully slopes). Polarization mixing in A2 is much less pronounced due to its comparatively smooth surface. In consequence, the difference $\Delta T_\mathrm{B}^\mathrm{V}$ between the T_B^V of both areas was small during the soil-frost event and the long dry spell, and increased again both after the soil thawed and after precipitation. However, the simulated T_B^V of A1 was at no time identical to that of A2, unlike the measurements. At horizontal polarization, the simulated T_B^H of both areas behaved very similarly most of the time. Therefore, $\Delta T_\mathrm{B}^\mathrm{H}$ did not change significantly throughout this time period in the simulations. Above all, the slower and less pronounced increase in the T_B^H of A2

observed in the measurements at the beginning of April could not be reproduced, leading to a significant deviation between the measured and simulated T_B^H for A2 in the first two weeks of April.

Looking at the diurnal T_B^p oscillations, we observed that they were more pronounced at $p = H$ than at $p = V$ on several days, both in the simulations and the measurements. This implies that they are not solely caused by the fluctuating T_{eff} since, due to the proportionality of T_B^p and T_{eff}, T_B^V should change more in response to changing T_{eff} than T_B^H. Test simulations, using first a constant value and then the simulated slightly fluctuating value for the wc of the uppermost soil layer, showed that this behavior can in fact be attributed to the very small daily wc fluctuations, which were observed also when the soil was very dry[6].

5 Discussion

The measurement results presented in the previous sections demonstrate the distinct influence of the relief of a soil surface on its thermal emission at L-band frequencies. At horizontal polarization, the brightness temperatures T_B^H of footprint A1 with the pronounced surface relief generally clearly exceeded the emission of the almost smooth area A2, whereas, at vertical polarization, the T_B^V of A1 were usually smaller than those of A2. The difference between the brightness temperatures of both areas was much more distinct at horizontal polarization. This furthermore implies that the difference $T_B^V - T_B^H$ was more pronounced for A2 than for A1.

This general behavior was reproduced well by the simulations and can mostly be explained by means of the analysis of the footprint topographies described in Section 4.3. Due to the pronounced relief in A1, the span of local observation angles θ_F is much larger for A1 than for A2 (Table II). In particular, significantly more regions of A1 are observed under very small, i.e. steep, observation angles. Emission from these regions is effectively lower at vertical polarization and higher at horizontal polarization compared to the emission of regions observed under larger, i.e. shallower, observation angles. This can be seen in Fig. 7c, when the T_B^p of A1 and A2 are compared to each other. Another effect of a distinct relief is polarization mixing due to surface tilting and the ensuing rotation of the plane of linear polarization. The enhanced polarization mixing in A1 is illustrated by the wider range of the polarization-rotation angle φ in A1 compared to A2 (Table II). This results in larger deviations of local reflectivities R_F^p from global ones R_{RM}^p (see Fig. 7a and b), which, in turn, lead to an additional decrease in T_B^V and increase in T_B^H of A1 compared to A2[7].

The difference in the span of brightness temperatures observed for each footprint as a result of varying local observation angles and the rotation of the polarization plane is much

---

[6] A more elaborate discussion of this effect can be found in Appendix D.

[7] Polarization crosstalk from horizontal to vertical polarization furthermore explains to some extent the stronger reaction of T_B^V in A1 to soil moisture changes, which was observed in the measurements as well as in the simulations.

greater at horizontal than at vertical polarization (Fig. 7c). Additionally, the brightness temperature changes caused by these effects are further enhanced at $p = \mathrm{H}$, but partly compensated for at $p = \mathrm{V}$ by the enhanced brightness temperatures of regions shielded from the cold sky and illuminated by their surroundings. This explains why the differences between the brightness temperatures of both footprint areas are larger at horizontal than at vertical polarization, as both the measurements and the simulations indicate. Figure 7c also illustrates why the difference between both polarizations is greater for A2 than for A1. Firstly, the T_B^p at both polarizations increasingly approach each other with decreasing local observation angles and, secondly, the T_B^H are additionally increased and the T_B^V decreased due to the polarization-rotation effects. Both effects are less pronounced for A2 than for A1, as described above.

This general behavior is not significantly influenced by the usually much lower brightness temperatures of the gully regions in A1 (Fig. 7c), which result from the higher soil-water content inside the gullies. Test simulations in which all regions were assigned identical soil-water content profiles yielded the same general differences between the brightness temperatures of A1 and A2 as described above, probably because the gullies cover only about 8% of the total area considered. Furthermore, they do not lie along the main line of observation, where the radiometer antenna is most sensitive (Fig. 8).

The prevailing stronger response of the brightness temperatures of A1 to changing meteorological conditions suggests a different hydrological behavior (e.g., infiltration, runoff, and soil drying) of both footprints. This leads, in turn, to different soil moisture dynamics in both areas. It seems reasonable to assume that the hydrology of A1 is strongly affected by the presence of the erosion gullies. On the one hand, gullies lead to more and faster surface runoff in A1 since they are close to saturation most of the time, and also because water from upstream in the catchment area gets funneled into the gullies. This results in a faster and more pronounced soil moisture increase in A1 than in A2 after the onset of precipitation. On the other hand, surface runoff may stop rather soon after a rainfall, and the areas outside the gullies will dry quite fast as the soil water can drain via the erosion gullies. Following this argumentation, the overall increase in soil moisture is less pronounced in A2, where no gullies are present, but subsequently the soil very probably dries more gradually. These hydrological differences could be further enhanced by the different soil properties of A1 and A2 arising from their different histories. The initial leveling and smoothing of A2 prior to beginning the measurement campaign certainly played an important role. These hypotheses explain the following observations:

-- The T_B^p measured in A1 react faster and more strongly to changing meteorological conditions.

-- The T_B^p measured in A1 initially increase faster after the end of precipitation.

-- The T_B^p measured in A1 cease to increase in times of intense soil drying when the T_B^p of A2 are still rising.

Differences in the hydrology of both areas could furthermore explain why this behavior is not as apparent in the brightness temperatures simulated. The same soil parameter values were

used for both footprints in the COUP model (Table I). That means, the soil-water content wc and the soil temperature T_{eff} used in the T_{B}^{p} simulations were identical for all locations outside the gullies, which made up most parts of both footprints. However, the hypothesis cannot be corroborated by the *in situ wc* measurements since they yield inaccurate information about the wc near the soil surface (which is exactly the soil layer that affects T_{B}^{p} most), and allow no clear conclusions as to the general wc behavior of both areas due their large spatial variation (Section 4.2). To turn the argument on its head, this shows the advantages of using microwave radiometry for the retrieval of near-surface soil moisture. This is also nicely illustrated by the two precipitation events of April 2009, which are not visible in the *in situ wc* measurements, but led to distinct changes in T_{B}^{p} (Section 4.5).

Some of the observed deviations between the measurement and the model results cannot be explained conclusively due to the complexity of the model and the simplifying assumptions that had to be made. These simplifications can be roughly subdivided into two categories. The first category are assumptions regarding or affecting the representation of the radiative-transfer in the model (Sections 3.4 to 3.6). Most important among these are:

-- The observed scene is approximated by a mosaic of planar, specular facets. That means, small-scale surface roughness and diffuse scattering are ignored.

-- The empirical dielectric mixing model (4) applied to derive soil permittivity from soil-water content does not take into account the specific soil characteristics of the investigation site. Furthermore, the imaginary part of the soil permittivity was assumed to be zero, i.e. losses are not considered, and thus coherent effects at greater soil depths might be overrated.

-- When distinguishing facets shielded from the cold sky by other facets, we assumed a flat horizon (29), and represented such facets as black-body radiators in the radiative-transfer model (3).

-- The effective physical temperature of the ground was approximated by the soil temperature at a depth of 8 cm throughout the whole investigation period regardless of the soil-water content.

The second kind of simplifications has to do with the parameterization of the soil and the modeling of soil-water content and temperature in the model (Section 3.3):

-- The COUP model used to compute soil-water content and temperature profiles is a one-dimensional approach that does not take into account lateral water and heat flow.

-- The thermal and hydrological soil properties were assumed to be identical everywhere laterally and only three different parameterizations were used in vertical direction in the COUP model (Table I). The erosion gullies were only regarded in terms of their shorter distance to the groundwater table.

-- The parameterization of the COUP model was mainly based on soil texture and *in situ* measurements within the artificial research catchment. It does not take into account the different histories of both footprint areas, especially the initial leveling and smoothing of footprint A2.

-- The soil parameterization was identical for the entire investigation period. That means, temporal variations in soil properties caused, e.g. by a redistribution of the different soil fractions were neglected.

Due to the complex interplay of the different processes involved, it is very hard to quantify the uncertainties resulting from these approximations. It can be assumed that most errors in the simulations introduced through the assumptions in the radiative transfer affect both footprints rather similarly and result in deviations in the absolute values of brightness temperatures measured and simulated. Errors arising from the assumptions regarding the soil parameterization and the hydrological modeling probably affect brightness temperatures of both areas differently and furthermore change with time and prevailing meteorological conditions. This is, for example, corroborated by the fact that the simulation results are more accurate for footprint A1, where the soil parameterization in the COUP model is also expected to perform better. Furthermore, major deviations in the overall behavior of the brightness temperatures measured and simulated mostly followed pronounced changes in the meteorological conditions and can be linked to peculiarities in the soil-water content simulations (Section 4.5).

6 Summary and Conclusions

The work presented provides a comprehensive data set of brightness temperatures, which allowed us to analyze and quantify relief effects on the decimeter to meter scale by directly comparing brightness temperatures of a plane surface with those of a surface with a distinct relief. We found that brightness temperatures of the soil surface with a distinct relief are increased at horizontal polarization and decreased at vertical polarization with respect to those of the plane surface, whereas this effect is more pronounced at horizontal polarization.

This was shown in the measurements and well reproduced by the simulations, indicating that the model developed is able to account for the main mechanisms controlling the thermal emission at 1.4 GHz. By analyzing the footprint topographies together with the brightness temperatures simulated for the individual facets, we were able to show that these effects are mainly due to the large range of local observation angles and to polarization mixing caused by the surface relief. At horizontal polarization, these effects are further enhanced, and at vertical polarization, they are partly compensated for by the increase in the emission of some of the facets due to the surrounding elevated terrain.

Comparing the brightness temperatures of both areas with each other furthermore showed that the two areas respond differently to changing meteorological conditions. Consequently, differences between the brightness temperatures of both areas changed with time, which was only partly reproduced in the simulations. This might indicate that the different responses of the brightness temperatures of both areas are mostly caused by differing soil characteristics and infiltration, runoff and soil drying behavior (as a consequence of the erosion gullies in A1 and the initial manipulation of the soil surface in A2), which are not specially taken into account in the simulations.

Comparing the measurements and the simulation results showed that the facet model developed is capable of explaining the prominent relief-related brightness temperature differences between both areas, and that it is not seriously limited by the simplifying assumptions made for the radiative transfer. The major deviations between the simulation and measurement results could, to a large degree, be attributed to an erroneous representation of the hydrological behavior (infiltration, runoff, soil drying) of both areas in the COUP model. A more complex (two-dimensional) hydrological model and a better knowledge of the soil characteristics would be necessary to account for this better. Reversing this chain of argumentation implies that using a facet model, calibrated to the specific investigation site, in an inversion scheme to retrieve soil moisture from brightness temperature measurements can result in a significant improvement of the retrievals for areas with a distinct surface relief.

Appendix A: List of Abbreviations and Symbols

A.1 Abbreviations

A1: observed footprint area with pronounced surface relief (erosion gullies)

A2: observed footprint area with approximately plane surface

POI: plane of incidence

RM-POI: radiometer or global plane of incidence

The RM-POI is the POI with respect to the radiometer. It is spanned by $\hat{\mathbf{z}}$ and $\hat{\mathbf{k}}_{RM}$, and is normal to the XY-plane.

VD-POI: view-direction plane of incidence

The VD-POI is the POI with respect to the view direction toward the facet. It is spanned by $\hat{\mathbf{z}}$ and $\hat{\mathbf{k}}_f$, and is normal to the XY-plane.

F-POI: facet or local plane of incidence

The F-POI is the POI with respect to the tilted facet. It is spanned by $\hat{\mathbf{n}}$ and $\hat{\mathbf{k}}_f$, and is normal to the facet's surface.

A.2 Symbols

$a_1^{pp'}$: coefficient describing the relation between $E_{VD}^{pp'}$ and E_{RM}^p

$a_2^{pp'}$: coefficient describing the relation between $E_F^{pp'}$ and E_{VD}^p

A: surface area of a facet

A^h: projection of A onto a horizontal plane $\left(A^h = A \cdot \cos\alpha = \left(5 \times 5 \right) \mathrm{cm}^2 \right)$

α: tilt angle (slope) of a facet (angle between $\hat{\mathbf{n}}$ and $\hat{\mathbf{z}}$)

d: depth below the soil surface

D: directivity of the antenna

$\Delta T_B^p, \Delta \overline{T}_B^p$: difference between $T_{B,A1}^p$ and $T_{B,A2}^p$, difference between $\overline{T}_{B,A1}^p$ and $\overline{T}_{B,A2}^p$

ε: soil permittivity

$\mathbf{E}_{POI}^{p}, \hat{\mathbf{E}}_{POI}^{p}$: electric field vector, p-polarized relative to the respective POI (POI = RM, VD, F), unit vector of $\mathbf{E}_{POI}^{p}$

$\mathbf{E}_{VD}^{pp'}$: projection of $\mathbf{E}_{RM}^{p}$ onto the direction of p'-polarization relative to the VD-POI

$\mathbf{E}_{VD}^{p\mathbf{k}_{F}}$: component of $\hat{\mathbf{E}}_{RM}^{p}$ parallel to $\hat{\mathbf{k}}_{F}$

$\mathbf{E}_{F}^{pp'}$: projection of $\mathbf{E}_{VD}^{p}$ onto the direction of p'-polarization relative to the F-POI

$\mathbf{E}_{in}$: electric field incident on a facet

$\mathbf{E}_{ref}$: electric field reflected on a facet

f: facet index $\left(f = 1, ..., n \right)$

φ: angle of polarization rotation; defines how the linear polarization of the F-POI is rotated with respect to the linear polarization of the VD-POI

ϕ: azimuth angle between $\mathbf{k}_{RM}$ and $\mathbf{k}_{F}$

k_{sat}: saturated hydraulic conductivity

$\mathbf{k}_{F}, \hat{\mathbf{k}}_{F}, \hat{\mathbf{k}}_{F,xy}$: view direction from the facet toward the antenna, unit vector of $\mathbf{k}_{F}$, projection of $\hat{\mathbf{k}}_{F}$ onto the XY-plane

$\hat{\mathbf{k}}_{F}'$: unit vector in direction from a facet toward radiation T_{in} incident on the facet

$\mathbf{k}_{RM}, \hat{\mathbf{k}}_{RM}, \hat{\mathbf{k}}_{RM,xy}$: direction of the antenna main axis, unit vector of $\mathbf{k}_{RM}$, projection of $\hat{\mathbf{k}}_{RM}$ onto the XY-plane

λ: observation wavelength ($\lambda = 0.21$ m)

λ_{p}: pore size distribution index

n: total number of facets in the respective footprint

$\hat{\mathbf{n}}$: unit vector of the surface normal of a facet

ω: angle between $\mathbf{k}_{RM}$ and $\mathbf{k}_{F}$

Ω: solid angle under which a facet appears as seen from the radiometer antenna

p, p': direction of linear polarization (p = H, V; p' = H, V)

ψ_{a}: air entry pressure

r: distance between the radiometer and a facet

R_{RM}^{p}: global (power) reflectivity of a facet at polarization p with respect to the RM-POI

R_{F}^{p}: local (power) reflectivity of a facet at polarization p with respect to the F-POI

t: time of radiometer measurement

T_{B}^{p}: brightness temperature at polarization p with respect to the RM-POI

$T_{B,f}^{p}$: brightness temperature of facet f at polarization p with respect to the RM-POI

$T_{B,total}^{p}$: total antenna brightness temperature at polarization p with respect to the RM-POI

$T_{B,A1}^{p}, T_{B,A2}^{p}$: brightness temperature of A1, brightness temperature of A2

$\overline{T}_{B,A1}^{p}, \overline{T}_{B,A2}^{p}$: mean brightness temperature of A1, mean brightness temperature of A2

T_{eff}: effective physical temperature

T_{in}: radiation incident on a facet and specularly reflected toward ELBARA

T_s: soil temperature

T_{sky}: sky brightness temperature

θ_F: facet elevation angle, also local observation angle (angle between $\hat{\mathbf{n}}$ and $\hat{\mathbf{k}}_F$)

θ_{VD}: view-direction elevation angle of the facet (angle between $\hat{\mathbf{z}}$ and $\hat{\mathbf{k}}_F$)

θ'_{VD}: polar angle between $\hat{\mathbf{z}}$ and the direction $\hat{\mathbf{k}}'_F$ toward T_{in}

θ_{RM}: radiometer elevation angle (angle between $\hat{\mathbf{z}}$ and $\hat{\mathbf{k}}_{RM}$, $\theta_{RM} = 55°$)

wc: soil-water content

wc_{res}: residual soil-water content

wc_{sat}: saturation soil-water content

(x, y, z): spatial coordinates of a facet

(x_{RM}, y_{RM}, z_{RM}): spatial coordinates of the radiometer

$\hat{\mathbf{z}}$: unit vector in vertical direction $(\hat{\mathbf{z}} = (0,0,1))$

Appendix B: Time Series of Brightness Temperatures

The entire time series (September 2008 to December 2009) of brightness temperatures measured and simulated with additional relevant meteorological data and soil parameters are shown below. Each page covers a time period of two months.
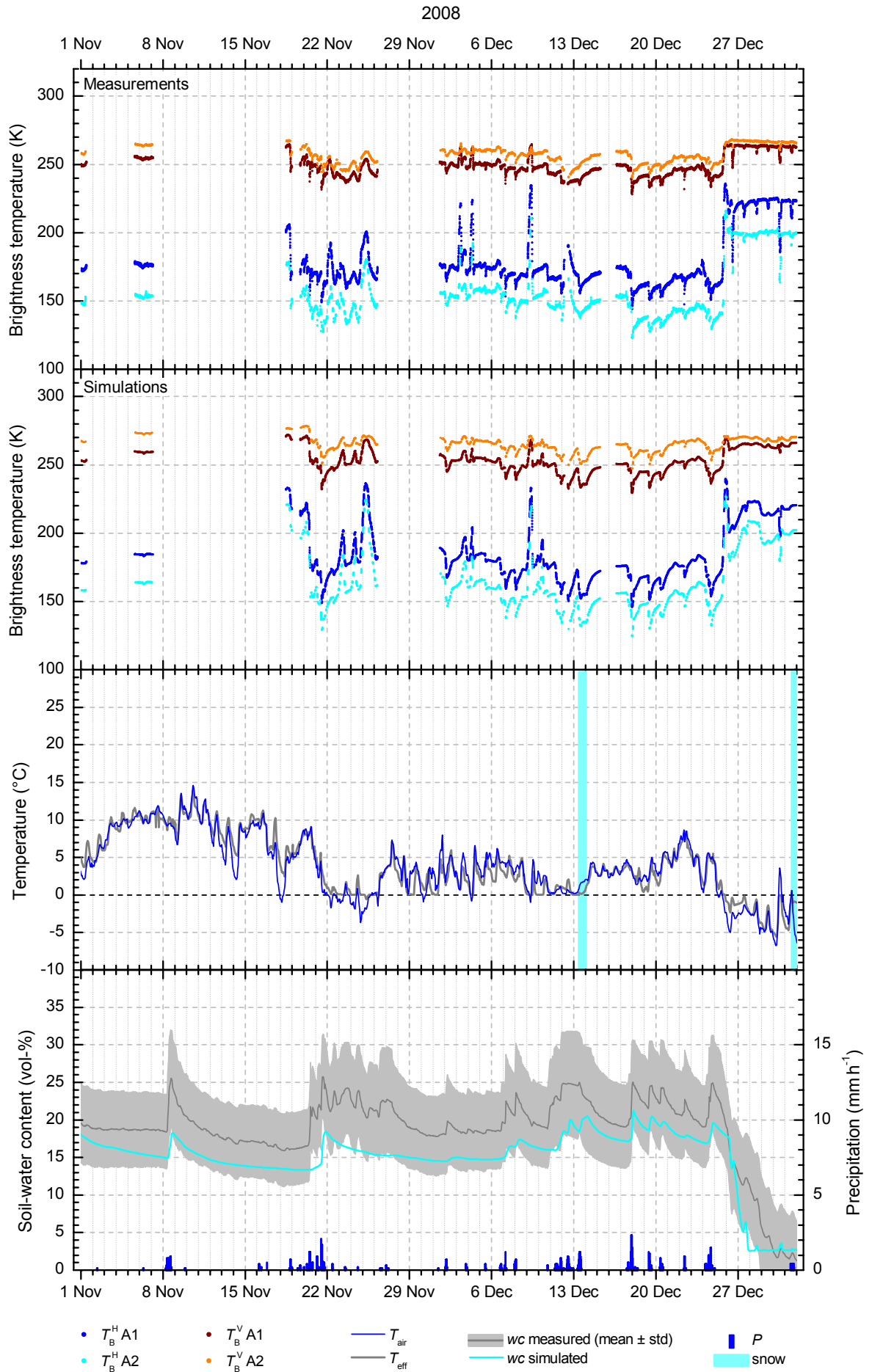
-- The uppermost panel shows the brightness temperatures T_B^p (p = H, V) measured. Blue and light blue dots indicate T_B^H at horizontal polarization of footprints A1 and A2, respectively. Brown and orange dots show the T_B^V of A1 and A2, respectively, at vertical polarization.

-- In the second panel, the corresponding T_B^p simulated for A1 and A2 are displayed.

-- The third panel shows the air temperature measured T_{air} (blue line) and the effective soil temperature T_{eff} (gray line), which was simulated with the COUP model. Additionally, time periods, when there was snow cover, are highlighted in light blue.

-- The lower panel provides information about the soil-water content wc and precipitation P. The light blue line shows the wc simulated with the COUP model for the 10–15 cm soil layer outside the erosion gullies. The gray shaded area illustrates the range mean ± standard deviation of the ten wc sensors placed within A1 and A2 at a depth of 10–15 cm. Blue bars show the precipitation measured.

The numbers in the two uppermost panels on page 87 refer to the discussion of measurement and simulation results during the specific meteorological conditions described in Section 4.5.
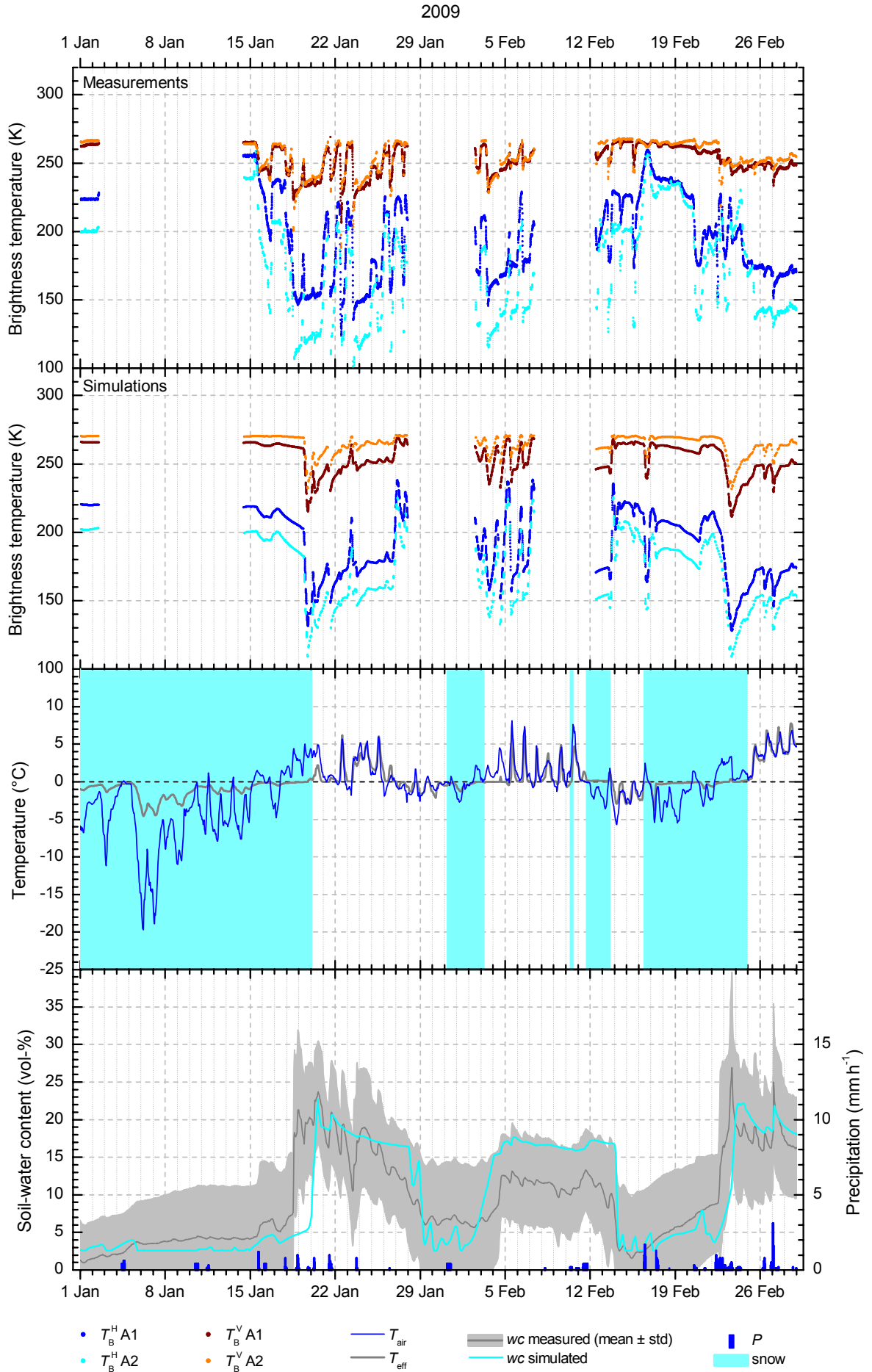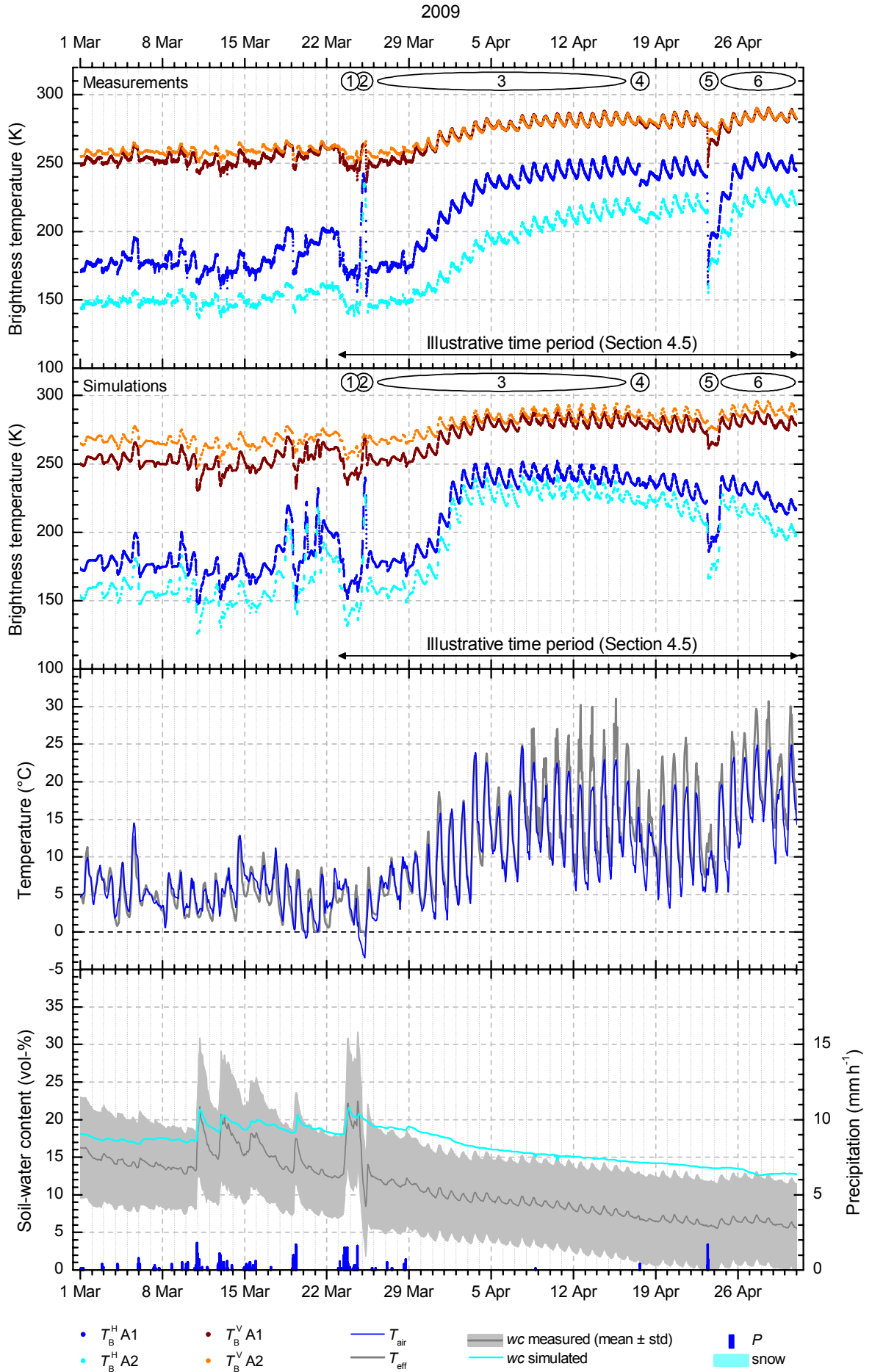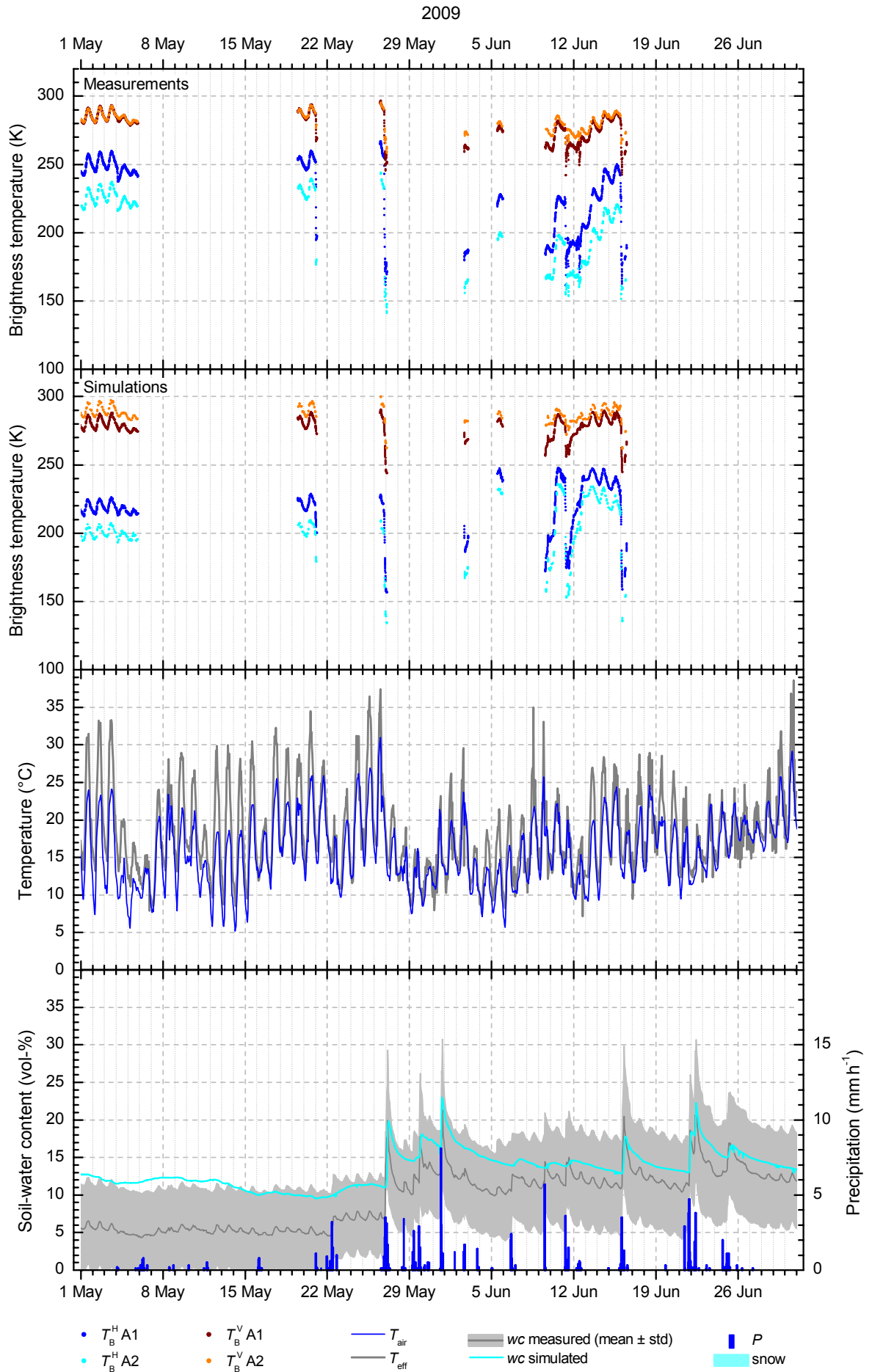
Monitoring the Brightness Temperature at 1.4 GHz of a Recently Renaturated Soil Surface
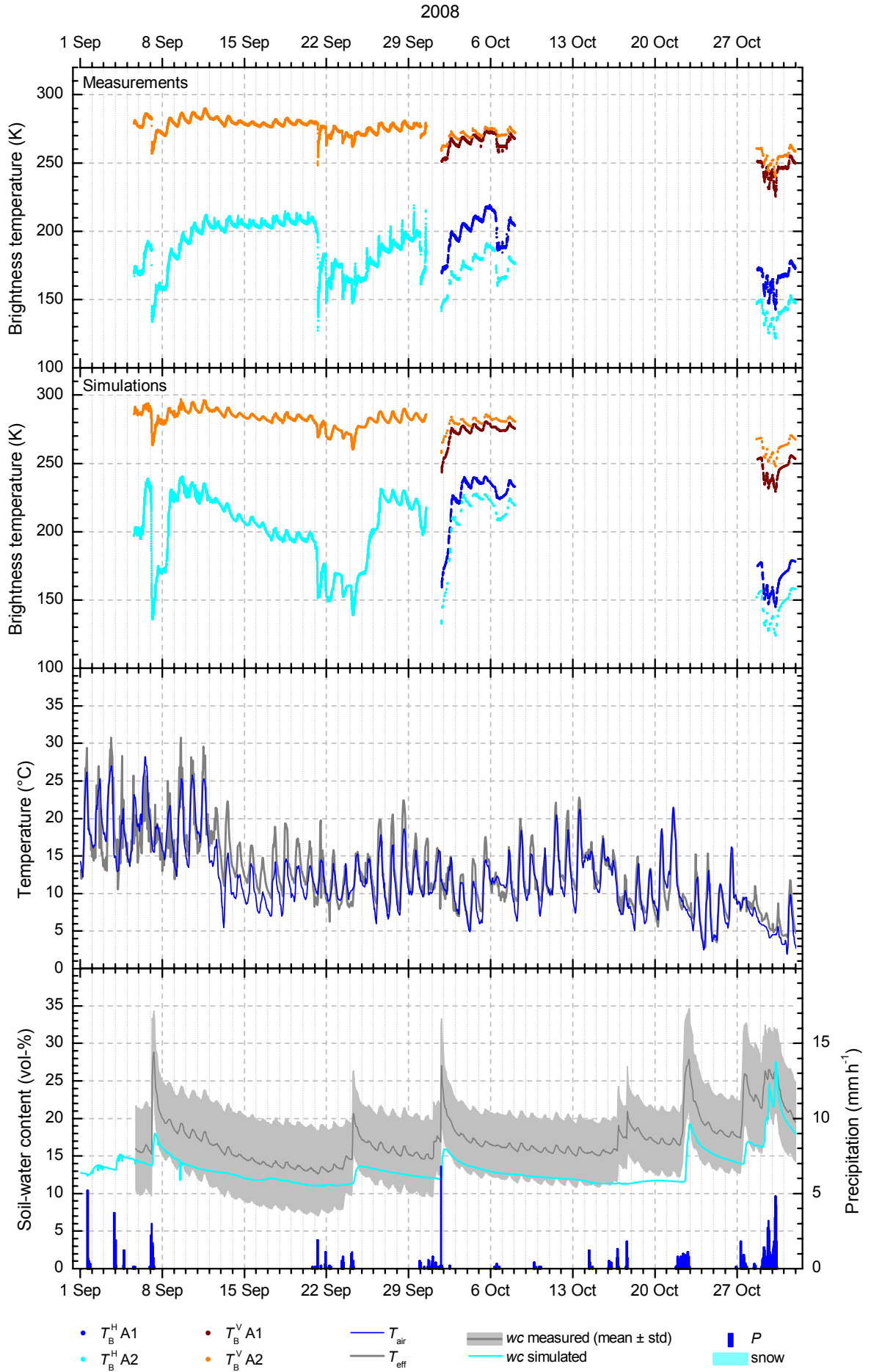
Monitoring the Brightness Temperature at 1.4 GHz of a Recently Renaturated Soil Surface
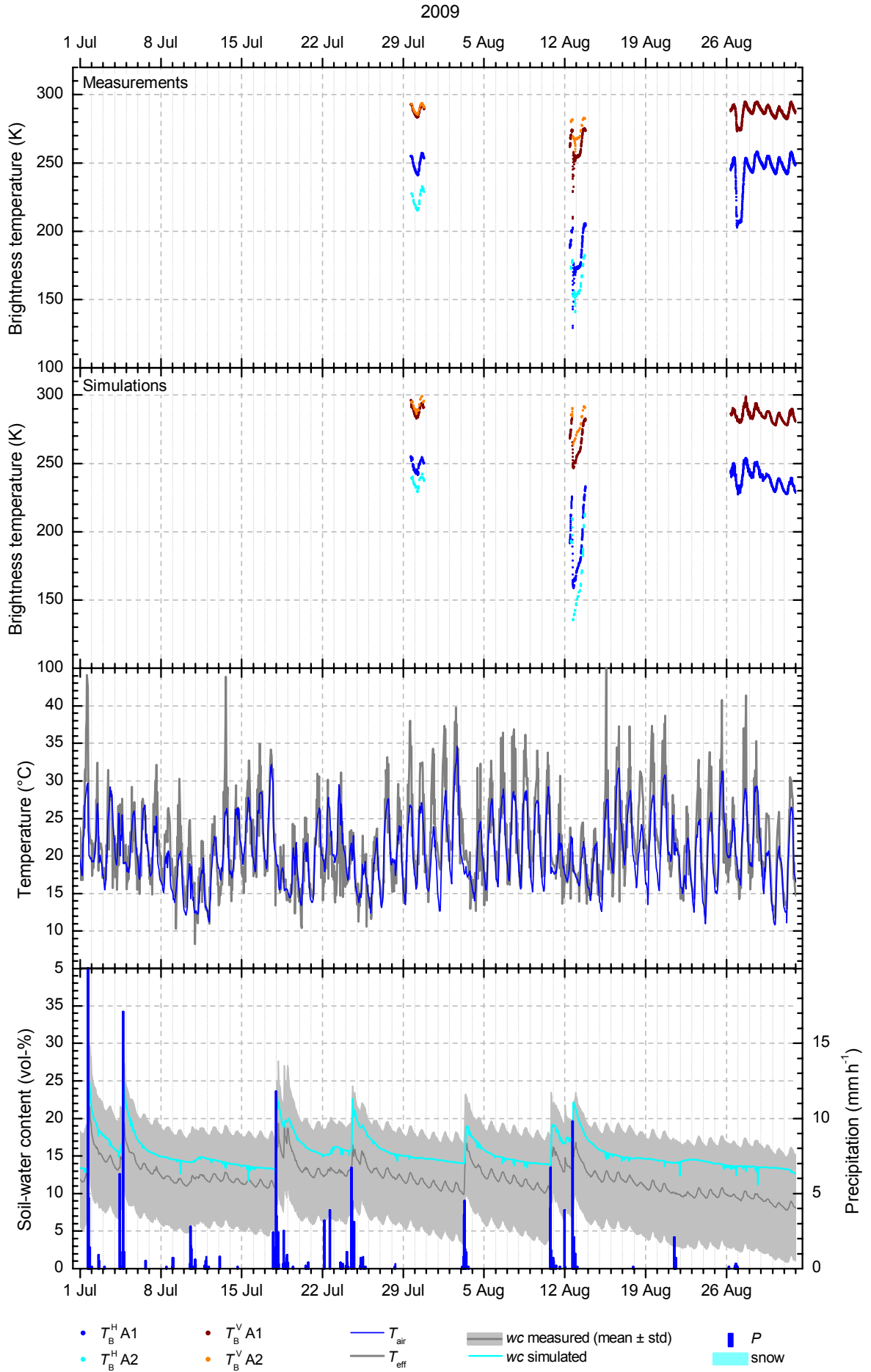
Monitoring the Brightness Temperature at 1.4 GHz of a Recently Renaturated Soil Surface

Monitoring the Brightness Temperature at 1.4 GHz of a Recently Renaturated Soil Surface

Monitoring the Brightness Temperature at 1.4 GHz of a Recently Renaturated Soil Surface
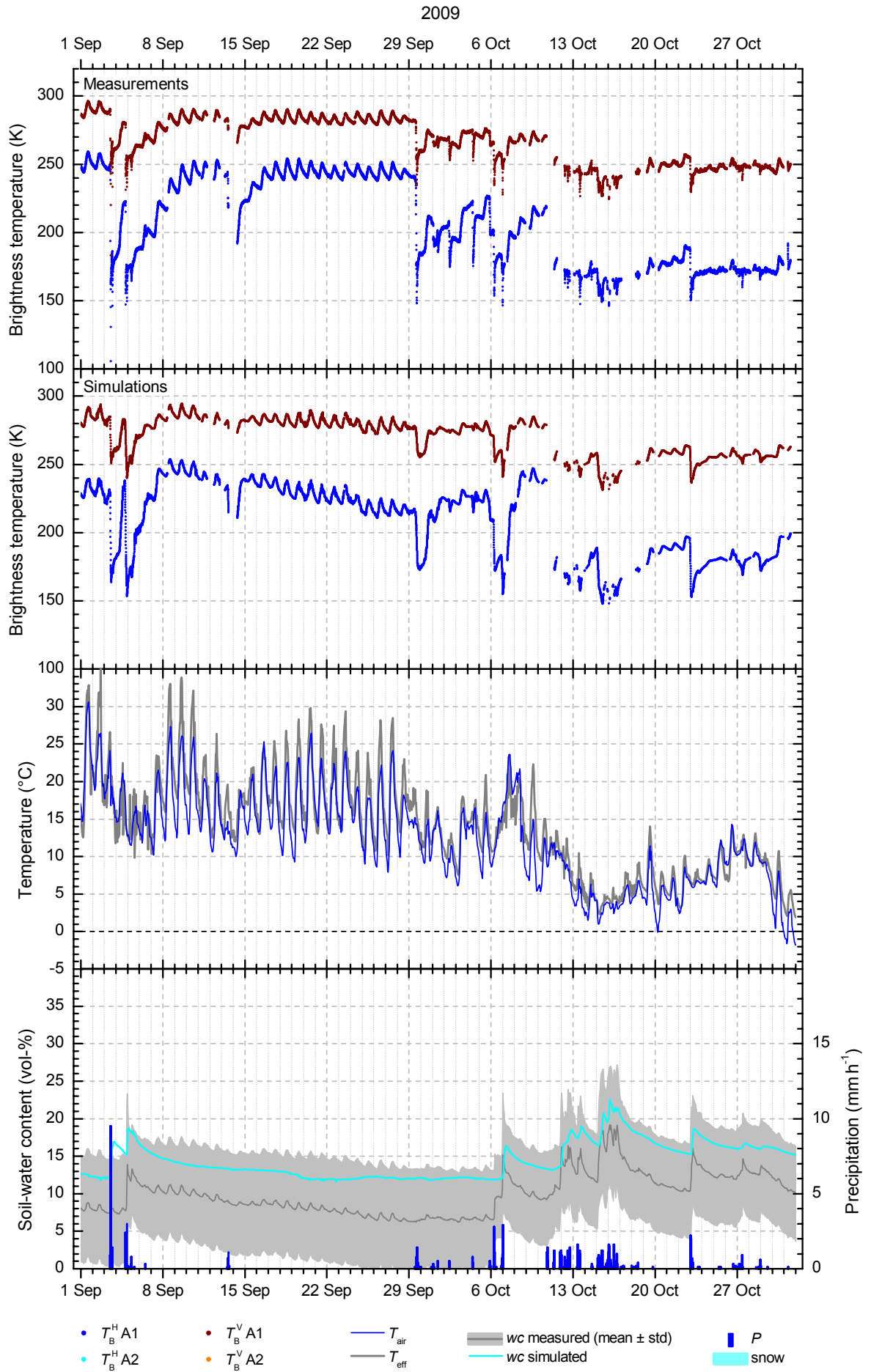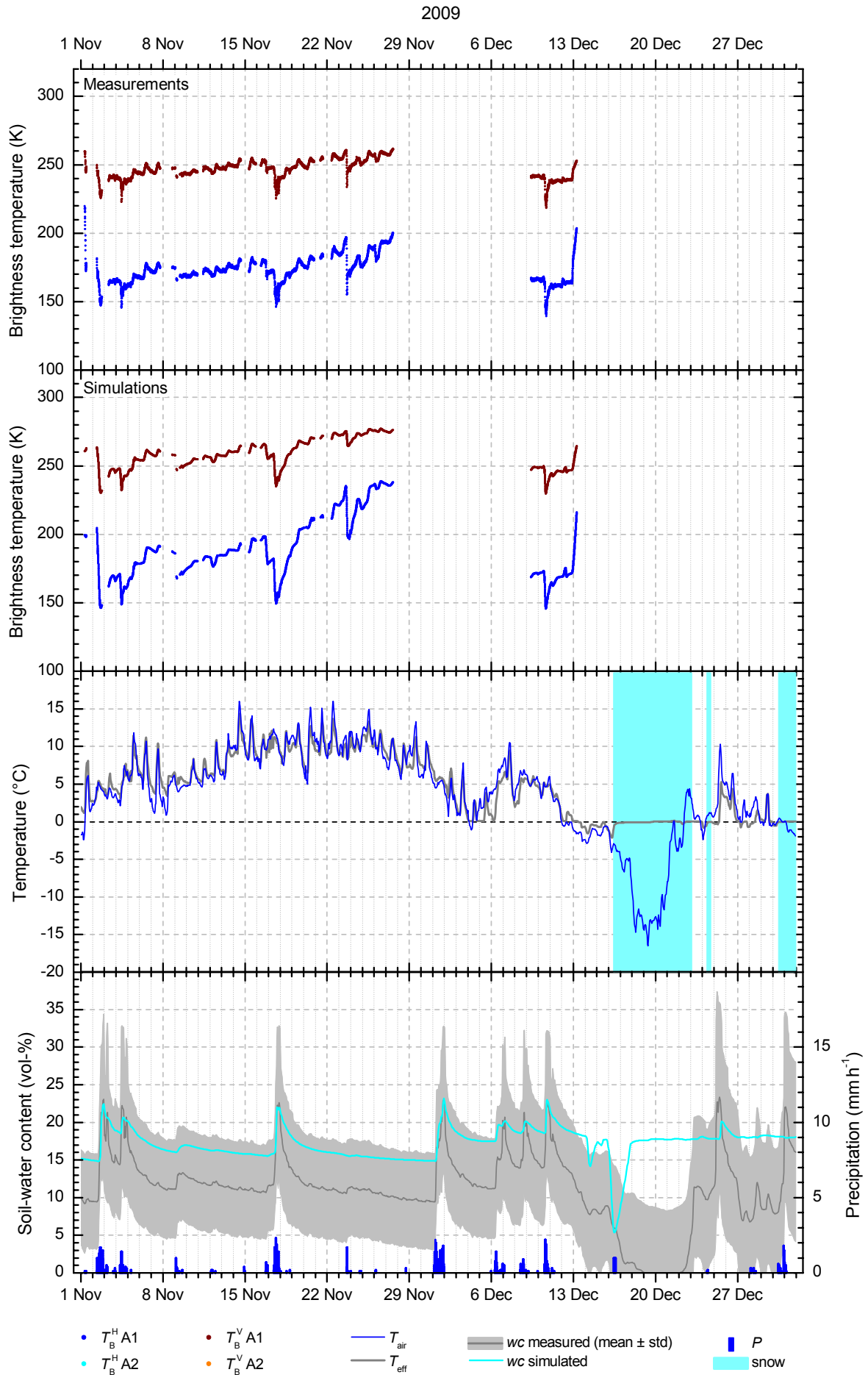
Monitoring the Brightness Temperature at 1.4 GHz of a Recently Renaturated Soil Surface

Monitoring the Brightness Temperature at 1.4 GHz of a Recently Renaturated Soil Surface

Appendix C: Comparison of Dielectric Mixing Models

To evaluate the uncertainties in the brightness temperature simulations introduced through our choice of the dielectric mixing model (C1) of Topp *et al.* [38] used in this work to relate soil permittivity ε with soil-water content *wc*, we compare (C1) with the models of Roth *et al.* [39] and of Wang and Schmugge [40] below. The relation of Topp *et al.* [38] is an experimentally derived relation between the real dielectric constant ε' of the soil and the volumetric soil-water content *wc* $(\mathrm{m}^3 \cdot \mathrm{m}^{-3})$

$$\varepsilon' = 3.03 + 9.3wc + 146.0wc^2 - 76.7wc^3. \tag{C1}$$

The relation proposed by Roth *et al.* [39] describes the soil as a mixture of water, solid soil and air, which are represented by their permittivities ε_w, ε_s and ε_a, and their volumetric contents *wc*, $(1-\eta)$ and $(\eta - wc)$

$$\varepsilon = \left[wc \cdot \varepsilon_w^\alpha + (1-\eta)\varepsilon_s^\alpha + (\eta - wc)\varepsilon_a^\alpha \right]^{1/\alpha}. \tag{C2}$$

Thereby, η is the porosity of the soil, and α is a parameter, which was experimentally determined to be $\alpha = 0.46 \pm 0.007$.

The model of Wang and Schmugge [40] considers also soil texture by introducing a transition point dividing the *wc* range into two domains. The transition soil-water content wc_t is correlated with the wilting point wc_{wp} of the soil, which, in turn, is related to the soil's sand content *S* and clay content *C* given in percent of dry weight. For $wc \leq wc_t$, a linear three-component mixture of air, water and solid soil phase is applied, whereas four components are considered for $wc > wc_t$. The fourth component represents the paracrystalline water, whereas this bound water is assumed to posses the permittivity ε_i of ice

$$\varepsilon = wc \cdot \varepsilon_x + (\eta - wc)\varepsilon_a + (1-\eta)\varepsilon_s \quad \text{for } wc \leq wc_t$$
$$\text{with } \varepsilon_x = \varepsilon_i + (\varepsilon_w - \varepsilon_i)\frac{wc}{wc_t}\gamma \tag{C3}$$

and

$$\varepsilon = wc_t \cdot \varepsilon_x + (wc - wc_t)\varepsilon_w + (\eta - wc)\varepsilon_a + (1-\eta)\varepsilon_s \quad \text{for } wc > wc_t$$
$$\text{with } \varepsilon_x = \varepsilon_i + (\varepsilon_w - \varepsilon_i)\gamma \tag{C4}$$

whereas

$$\gamma = -0.57wc_{wp} + 0.481$$
$$wc_t = 0.49wc_{wp} + 0.165 \tag{C5}$$
$$wc_{wp} = 0.06774 - 0.00064\,S + 0.00478\,C.$$

A more extensive review of the different models can be found, e.g. in [41].

The three models were evaluated for soil-water contents $0 \, \text{m}^3 \cdot \text{m}^{-3} \leq wc \leq 0.38 \, \text{m}^3 \cdot \text{m}^{-3}$ using the model parameters given in the caption of Fig. C1 and, subsequently, we calculated brightness temperatures $T_B^p(wc)$ ($p = $ H, V) based on the three $\varepsilon(wc)$ relations (Fig. C2). To this end, we calculated soil reflectivities R^p from ε using the Fresnel equations and then calculated T_B^p using the zero-order radiative-transfer model $T_B^p = (1 - R^p) T_{\text{eff}} + R^p T_{\text{sky}}$.

The model of Topp *et al.* yields the lowest ε' values compared to the other relations investigated except for very high $wc > 0.31 \, \text{m}^3 \cdot \text{m}^{-3}$ (Fig. C1). Generally it can be said that for $wc \leq 0.20 \, \text{m}^3 \cdot \text{m}^{-3} = wc_t$ the models of Topp *et al.* and Wang and Schmugge *et al.* yield quite similar results, whereas at $wc > 0.20 \, \text{m}^3 \cdot \text{m}^{-3}$ the relations of Topp *et al.* and Roth *et al.* approach each other, while the relation of Wang and Schmugge provides considerably larger ε'. Table C-I shows the differences $\Delta\varepsilon'$ between the differently calculated ε' for $wc = 0 \, \text{m}^3 \cdot \text{m}^{-3}$, $wc = \eta = 0.38 \, \text{m}^3 \cdot \text{m}^{-3}$, and for the wc, where $\Delta\varepsilon'$ are largest.

When the differently calculated T_B^p are compared to each other (Fig. C2), we see the same similarities and discrepancies between the different models as described above. Correspondingly, T_B^p calculated based on the relation of Topp *et al.* are always largest except for $wc > 0.31 \, \text{m}^3 \cdot \text{m}^{-3}$, where they are somewhat smaller but almost identical to the T_B^p calculated based on the relation of Roth *et al.* The deviations between the differently calculated T_B^p are much more pronounced at horizontal than at vertical polarization (Table C-II). The large difference between the T_B^H calculated based on Topp *et al.* and on Wang and Schmugge at $wc \leq 0.02 \, \text{m}^3 \cdot \text{m}^{-3}$ is of no importance for our T_B^p simulations since the simulated wc was always larger than $0.02 \, \text{m}^3 \cdot \text{m}^{-3}$.

Furthermore, we performed additional T_B^p simulations for footprint A1 for the illustrative time period 23 March to 1 May 2009 (discussed in Section 4.5) to show how the choice of the mixing model influences the simulation results. To this end, we assumed the soil to be homogenous with the soil-water content wc, which was simulated with the COUP model for the uppermost soil layer. We then used the three different mixing models to compute soil permittivities ε from which we then derived the local facet reflectivities R_F^p as input to our facet model. The results of these T_B^p simulations are shown in Fig. C3 together with the measurements and the "original" T_B^p simulations (using the simulated wc profile as input to the dielectric layer model and the relation of Topp *et al.* to relate ε to wc, Section 3.4).

At vertical polarization, the simulation based on the model of Topp *et al.* (black line) yields larger T_B^V than the calculations based on Roth *et al.* (red line) and on Wang and Schmugge (blue line) throughout the whole time period. It also agrees best with the measured T_B^V (brown line) and the original simulation (orange line). The simulation based on Roth *et al.* generally yields the lowest values for T_B^V, whereas the results become very similar to those of the simulation based on Wang and Schmugge in times when T_B^V are high (i.e., wc is low and T_{eff} is high, see Fig. 11). The mean differences ΔT_B^V between the T_B^V simulated based on Topp *et al.* and the other two models are 3.4 K for Roth *et al.* and 2.6 K for Wang and Schmugge.
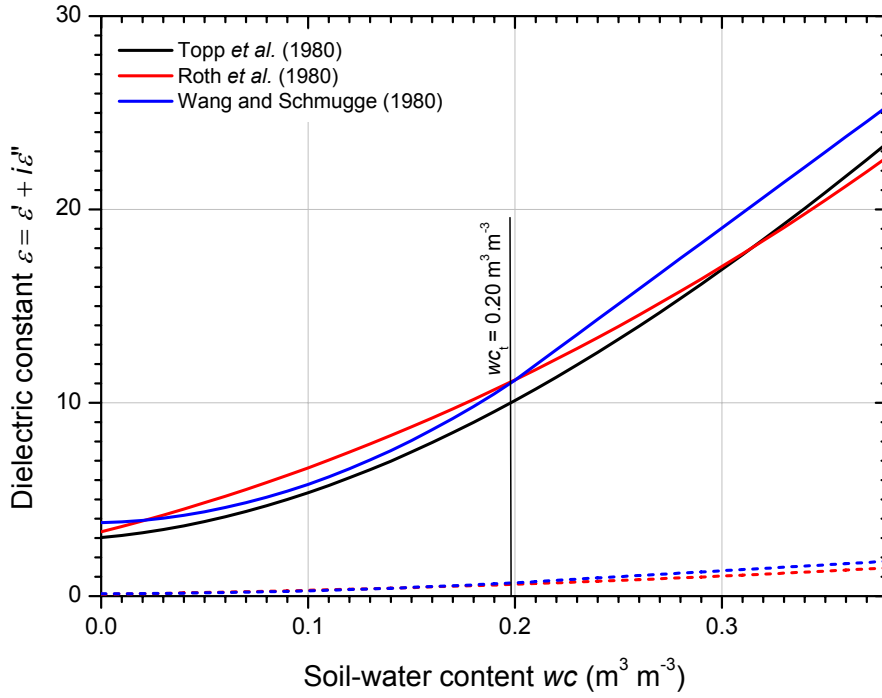
Fig. C1. Comparison of three soil dielectric models ε versus wc for the following parameters: $\varepsilon_a = 1$, $\varepsilon_s = 5.5 + 0.2i$, $\varepsilon_w = 79.7 + 6.18i$, $\varepsilon_i = 4 + 0.1i$, $\eta = 0.38$, $S = 84.8\%$, and $C = 6.1\%$. The values for the permittivities were taken from [41], and the information for soil porosity and texture are from [21].
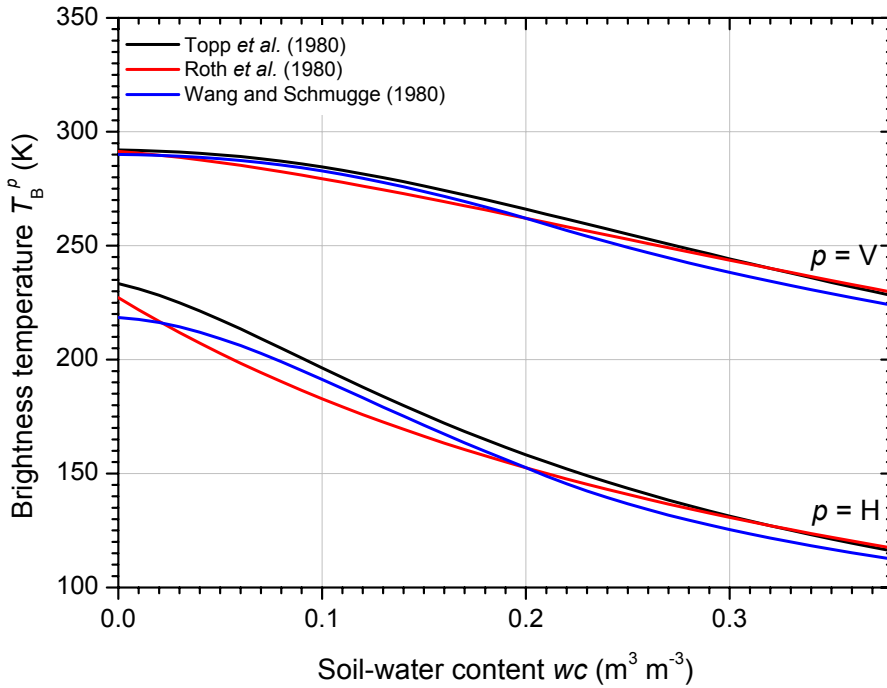

Fig. C2. Brightness temperatures T_B^p (p = H, V) versus wc for a homogeneous soil. The T_B^p were calculated based on the three $\varepsilon(wc)$ relations shown in Fig. C1 for the observation angle $\theta = 55°$, physical effective soil temperature $T_{eff} = 293$ K and sky brightness $T_{sky} = 6$ K.

Table C-I. Differences $\Delta\varepsilon'$ between the different dielectric mixing models at $wc = 0\ \mathrm{m^3 \cdot m^{-3}}$, at wc, where $\Delta\varepsilon'$ are largest, and at $wc = 0.38\ \mathrm{m^3 \cdot m^{-3}} = \eta$.

Roth *et al.* versus Topp *et al.*		Wang&Schmugge versus Topp *et al.*	
wc ($\mathrm{m^3 \cdot m^{-3}}$)	$\Delta\varepsilon'$	wc ($\mathrm{m^3 \cdot m^{-3}}$)	$\Delta\varepsilon'$
0	0.3	0	0.8
0.13	1.3	0.32	2.2
0.38	−0.7	0.38	1.9

Table C-II. Differences $\Delta T_{\mathrm{B}}^{p}$ (p = H, V) between the brightness temperatures T_{B}^{p} calculated based on the three different soil dielectric models at $wc = 0\ \mathrm{m^3 \cdot m^{-3}}$, at wc, where $\Delta T_{\mathrm{B}}^{p}$ are largest, and at $wc = 0.38\ \mathrm{m^3 \cdot m^{-3}}$.

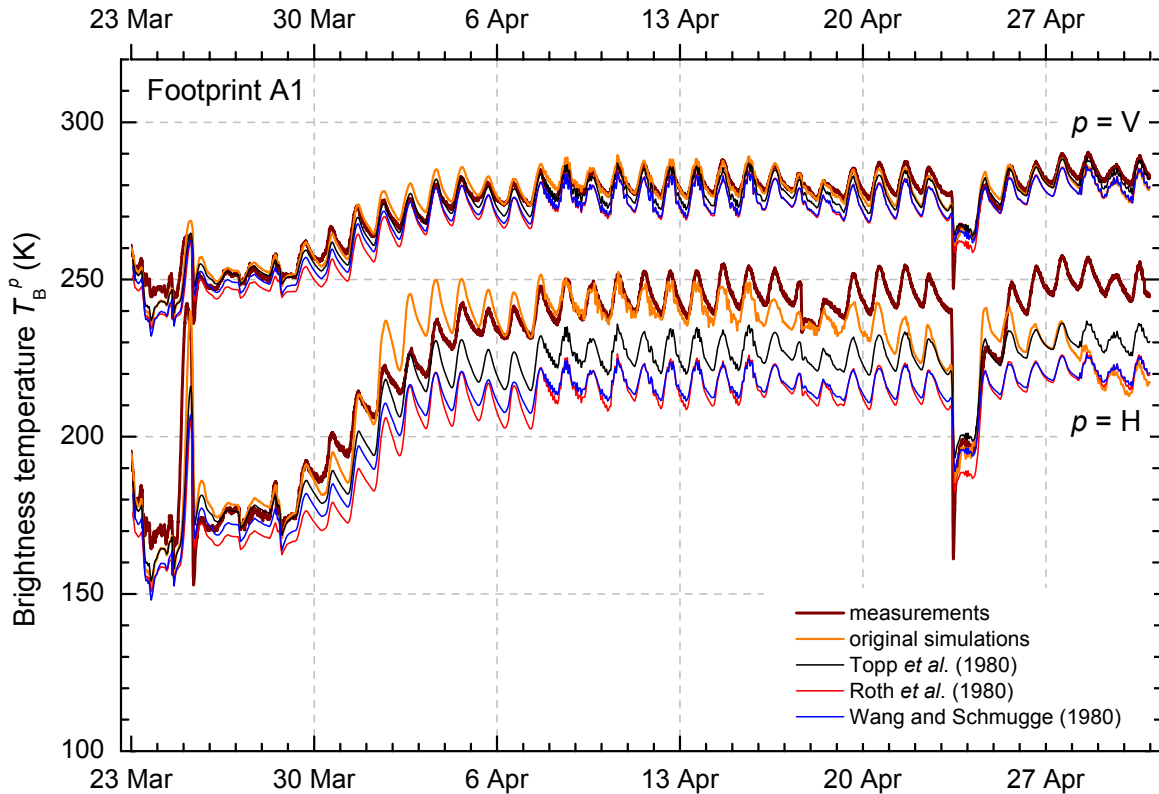| Roth *et al.* versus Topp *et al.*			Wang&Schmugge versus Topp *et al.*		
wc ($\mathrm{m^3 \cdot m^{-3}}$)	$\Delta T_{\mathrm{B}}^{\mathrm{H}}$ (K)	$\Delta T_{\mathrm{B}}^{\mathrm{V}}$ (K)	wc ($\mathrm{m^3 \cdot m^{-3}}$)	$\Delta T_{\mathrm{B}}^{\mathrm{H}}$ (K)	$\Delta T_{\mathrm{B}}^{\mathrm{V}}$ (K)
0	−6.3	−0.7	0	−14.9	−2.0
0.06	−15.0		0	−14.9	
0.12		−5.3	0.28		−6.1
0.38	1.3	1.4	0.38	−3.6	−4.2

Fig. C3. Comparison of the brightness temperature simulations based on the three different dielectric mixing models for the time period from 23 March to 1 May 2009. For comparison also the measured brightness temperatures and the original simulations (the same as in Fig. 11) are shown.

The same general behavior is observed at horizontal polarization, whereas the differences between the simulations are more pronounced than at vertical polarization. Also at p = H, the simulation based on Topp *et al.* yields the highest $T_{\mathrm{B}}^{\mathrm{H}}$, and agrees best with the measurements. This is especially pronounced in times, when $T_{\mathrm{B}}^{\mathrm{H}}$ are generally high (e.g., 1 to 23 April). The simulation based on Roth *et al.* yields the lowest $T_{\mathrm{B}}^{\mathrm{H}}$, whereas it becomes very similar to the simulation based on Wang and Schmugge, when $T_{\mathrm{B}}^{\mathrm{H}}$ are high. The mean differences $\Delta T_{\mathrm{B}}^{\mathrm{H}}$ between the simulations are 10.1 K (Topp *et al.* versus Roth *et al.*) and 8.1 K (Topp *et al.* versus Wang and Schmugge).

The three simulations assuming a homogenous soil with a constant soil moisture profile with depth underestimate the measurements and the original simulation slightly at p = V and distinctly at p = H, which is least pronounced in the simulation based on the model of Topp *et al.* This means, using the real *wc* profile and the coherent dielectric layer model to calculate local facet reflectivities R_{F}^{p} generally enhances the emissivity of the soil compared to the assumption of a constant *wc* with depth.

The comparisons presented above show that the choice of the mixing model used to relate ε to *wc* can influence the simulations results. The corresponding uncertainties in the T_{B}^{p} simulations are comparatively small at p = V, but can become significant at p = H. In the time period from 23 March to 1 May 2009 they are in the range of $\approx$3 K (p = V) and $\approx$10 K (p = H), respectively. The simulations shown in Fig. C3 demonstrate that the calculation based on Topp *et al.* yields reasonable results, thus justifying our choice of the dielectric mixing model of Topp *et al.* Furthermore, it is shown that using the simulated *wc* profile and the dielectric layer model to compute R_{F}^{p} improves the simulation results compared to simulations, where the soil is assumed to be homogeneous with a constant soil moisture profile.

Appendix D: Diurnal Brightness Temperature Oscillations

It is to be expected that the diurnal brightness temperature oscillations of a dry soil are more pronounced at vertical than at horizontal polarization since brightness temperatures T_{B}^{p} (p = H, V) are directly proportional to the soil's physical temperature T_{eff}, and $T_{\mathrm{B}}^{\mathrm{V}}$ is always larger than $T_{\mathrm{B}}^{\mathrm{H}}$. However, on several days during the illustrative time period shown in Fig. 11, we observe that the diurnal T_{B}^{p} oscillations are more pronounced at p = H than at p = V in the measurements as well as in the simulations (Table D-I). This phenomenon is observed for both footprints A1 and A2, and is especially obvious between 1 and 16 April 2009.

This finding implies that the diurnal T_{B}^{p} oscillations are not solely caused by the daily fluctuations of T_{eff}, but seem to be additionally related to the very small *wc* changes observed also when the soil is very dry. To test this hypothesis, we simulated T_{B}^{p} for A1 for the time period between 1 and 6 April 2009 assuming a homogenous soil with a constant soil moisture *wc* with depth. In a first simulation, we used the slightly fluctuating *wc* simulated with the COUP model for the uppermost soil layer. In a second simulation, we kept *wc* constant with time using the mean *wc* of the time period considered. Although this analysis is confined to footprint A1, the results presented below apply also to footprint A2.

Table D-I. Measured and simulated diurnal brightness temperature oscillations (expressed as the difference $T_{B,max}^{p} - T_{B,min}^{p}$ between the largest and lowest T_{B}^{p} observed on the respective day) for some days between 1 and 16 April 2009 (footprint A1).

day	measurements		simulations	
	$T_{B,max}^{V} - T_{B,min}^{V}$ (K)	$T_{B,max}^{H} - T_{B,min}^{H}$ (K)	$T_{B,max}^{V} - T_{B,min}^{V}$ (K)	$T_{B,max}^{H} - T_{B,min}^{H}$ (K)
4 April	10.4	14.7	11.0	17.3
5 April	6.1	8.6	6.1	11.8
14 April	11.3	16.2	11.4	12.8
15 April	9.5	14.1	13.0	15.4

Table D-II. Diurnal brightness temperature oscillations on some days between 1 and 16 April 2009 simulated using a constant soil-water content wc and using a fluctuating wc, respectively.

day	constant wc		fluctuating wc	
	$T_{B,max}^{V} - T_{B,min}^{V}$ (K)	$T_{B,max}^{H} - T_{B,min}^{H}$ (K)	$T_{B,max}^{V} - T_{B,min}^{V}$ (K)	$T_{B,max}^{H} - T_{B,min}^{H}$ (K)
4 April	9.8	7.9	11.6	15.4
5 April	5.0	4.1	6.6	10.3
14 April	11.2	9.0	12.1	12.9
15 April	12.9	10.4	13.9	14.5

The uppermost panel in Fig. D1 shows the results of these T_{B}^{p} simulations. Brown lines show T_{B}^{p} simulated assuming a constant wc (dashed lines in the third panel) and orange lines indicate T_{B}^{p} simulated for the slightly fluctuating wc (solid lines in the third panel). The second and third panel show the effective soil temperature T_{eff} and the soil-water content wc inside and outside the gullies, respectively. Table D-II shows the corresponding diurnal T_{B}^{p} oscillations (expressed as the difference $T_{B,max}^{p} - T_{B,min}^{p}$) for the same days, which are listed in Table D-I. At $p = V$, simulation results are almost identical regardless of the wc used (Fig. D1, top panel). Only on 1 and 2 April, significant differences between the two simulations are observed, which are caused by the strongly decreasing wc outside the gullies. At $p = H$, however, the differences between both simulations are much more pronounced. Above all, simulations for the fluctuating wc show significantly larger diurnal T_{B}^{H} oscillations than the simulations for the constant wc. As a result, daily T_{B}^{p} oscillations are indeed more pronounced at $p = V$ in the simulations for the constant wc (i.e., T_{B}^{p} oscillations are exclusively due to fluctuating T_{eff}), but are more pronounced at $p = H$, when a fluctuating wc is used (i.e., T_{B}^{p} oscillations are a result of fluctuating T_{eff} as well as of fluctuating wc). This is also confirmed, when the $T_{B,max}^{p} - T_{B,min}^{p}$ listed in Table D-II are compared to each other.
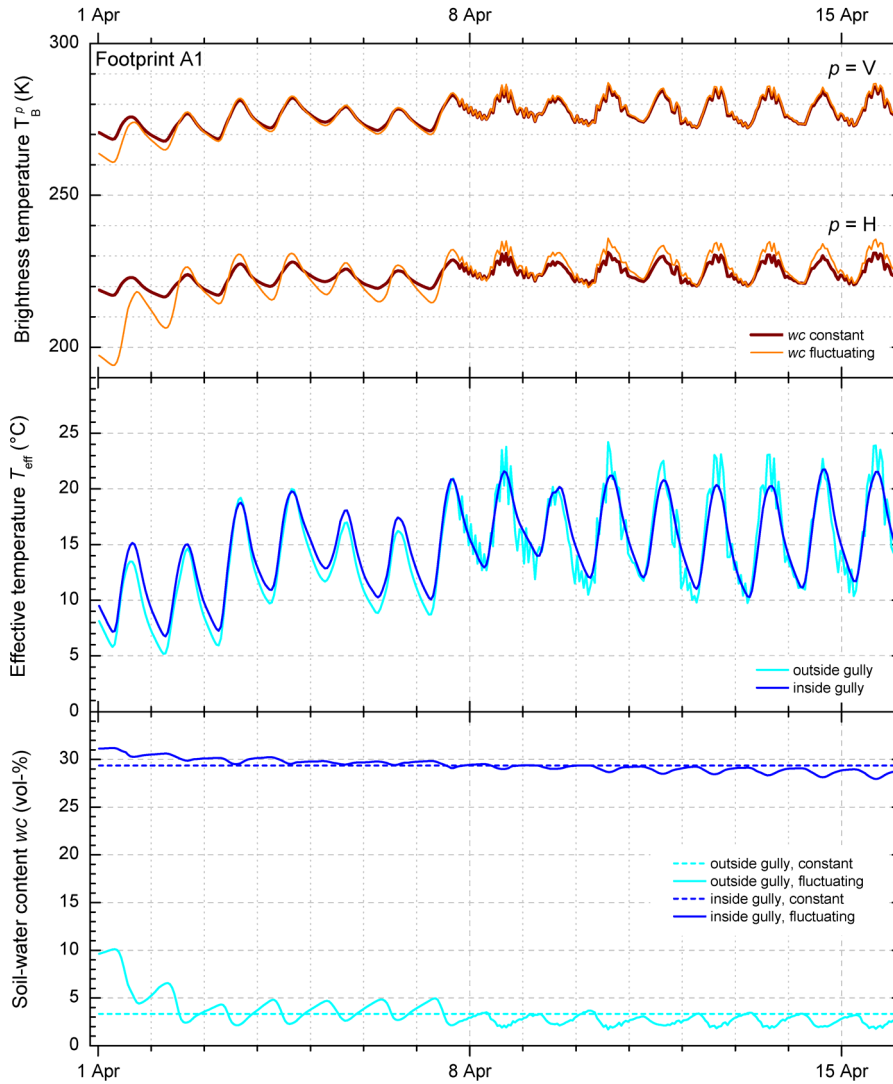
Fig. D1. Simulation results for the time period from 1 to 16 April 2009 (refer to the text for a detailed description of the different symbols).

These results show that the very small wc fluctuations observed also when the soil is very dry can lead to distinctly enhanced diurnal T_B^p oscillations, whereas this effect is much more pronounced at p = H. This effect could perhaps be utilized to infer information about such small daily wc changes from the comparison of the magnitudes of the diurnal T_B^p oscillations at both polarizations.

Acknowledgement

References

[1] W. Wagner, G. Bloschl, P. Pampaloni, J. C. Calvet, B. Bizzarri, J. P. Wigneron, and Y. Kerr, "Operational readiness of microwave remote sensing of soil moisture for hydrologic applications," *Nord. Hydrol.*, vol. 38, no. 1, pp. 1-20, 2007.

[2] T. J. Schmugge, W. P. Kustas, J. C. Ritchie, T. J. Jackson, and A. Rango, "Remote sensing in hydrology," *Adv. Water Res.*, vol. 25, no. 8-12, pp. 1367-1385, 2002.

[3] Y. H. Kerr, P. Waldteufel, J. P. Wigneron, S. Delwart, F. Cabot, J. Boutin, M. J. Escorihuela, J. Font, N. Reul, C. Gruhier, S. E. Juglea, M. R. Drinkwater, A. Hahne, M. Martin-Neira, and S. Mecklenburg, "The SMOS mission: New tool for monitoring key elements of the global water cycle," *Proc. IEEE*, vol. 98, no. 5, pp. 666-687, 2010.

[4] T. Schmugge, "Remote sensing of soil moisture," in *Encyclopedia of Hydrological Forecasting*, M. G. Anderson and T. Burt, Eds. Chichester, U.K.: Wiley, 1985, pp. 101-124.

[5] A. M. Shutko, "Microwave radiometry of lands under natural and artificial moistening," *IEEE Trans. Geosci. Remote Sens.*, vol. GE-20, no. 1, pp. 18-26, 1982.

[6] J.-P. Wigneron, Y. H. Kerr, P. Waldteufel, K. Saleh, M.-J. Escorihuela, P. Richaume, P. Ferrazzoli, P. d. Rosnay, R. Gurney, J.-C. Calvet, J. P. Grant, M. Guglielmetti, B. Hornbuckle, C. Mätzler, T. Pellarin, and M. Schwank, "L-band microwave emission of the biosphere (L-MEB) model: Description and calibration against experimental data sets over crop fields," *Remote Sens. Environ.*, vol. 107, no. 4, pp. 639-655, 2007.

[7] M. Guglielmetti, M. Schwank, C. Mätzler, C. Oberdörster, J. Vanderborght, and H. Flühler, "FOSMEX: Forest soil moisture experiments with microwave radiometry," *IEEE Trans. Geosci. Remote Sens.*, vol. 46, no. 3, pp. 727-735, 2008.

[8] B. J. Choudhury, T. Schmugge, and T. Mo, "A parameterization of effective soil temperature for microwave emission," *J. Geophys. Res.*, vol. 87, no. C2, pp. 1301-1304, 1982.

[9] J.-P. Wigneron, A. Chanzy, P. d. Rosnay, C. Rüdiger, and J.-C. Calvet, "Estimating the effective soil temperature at L-band as a function of soil properties," *IEEE Geosci. Remote Sens. Lett.*, vol. 46, no. 3, pp. 797-807, 2008.

[10] C. Mätzler, "Passive microwave signatures of landscapes in winter," *Meteorol. Atmos. Phys.*, vol. 54, no. 1-4, pp. 241-260, 1994.

[11] M. Schwank, M. Stähli, H. Wydler, L. Jörg, C. Mätzler, and H. Flühler, "Microwave L-band emission of freezing soil," *IEEE Trans. Geosci. Remote Sens.*, vol. 42, no. 6, pp. 1252-1261, 2004.

[12] K. Schneeberger, M. Schwank, C. Stamm, P. d. Rosnay, C. Mätzler, and H. Flühler, "Topsoil structure influencing soil water retrieval by microwave radiometry," *Vadose Zone J.*, vol. 3, no. 4, pp. 1169-1179, 2004.

[13] J.-P. Wigneron, L. Laguerre, and Y. H. Kerr, "A simple parameterization of the L-band microwave emission from rough agricultural soils," *IEEE Trans. Geosci. Remote Sens.*, vol. 39, no. 8, pp. 1697-1707, 2001.

[14] C. Mätzler and A. Standley, "Technical note: Relief effects for passive microwave remote sensing," *Int. J. Remote Sens.*, vol. 21, no. 12, pp. 2403-2412, 2000.

[15] Y. H. Kerr, F. Secherre, J. Lastenet, and J. P. Wigneron, "SMOS: Analysis of perturbing effects over land surfaces," *Proc. IEEE IGARSS*, Toulouse, France, 2003, pp. 908-910.

[16] A. Monerris, P. Benedicto, M. Vall-Ilossera, A. Camps, E. Santanach, M. Piles, and R. Prehn, "Assessment of the topography impact on microwave radiometry at L-band," *J. Geophys. Res.*, vol. 113, no. B12202, 2008.

[17] N. Pierdicca, L. Pulvirenti, and F. S. Marzano, "Simulating topographic effects on spaceborne radiometric observations between L and X frequency bands," *IEEE Trans. Geosci. Remote Sens.*, vol. 48, no. 1, pp. 273-282, 2010.

[18] A. Monerris, P. Benedicto, M. Vall-Hossera, A. Camps, M. Piles, E. Santanach, and R. Prehn, "Topography effects on the L-band emissivity of soils: TuRTLE 2006 field experiment," *Proc. IEEE IGARSS*, Barcelona, Spain, pp. 2244-2247, 2007.

[19] C. Mätzler, D. Weber, M. Wüthrich, K. Schneeberger, C. Stamm, and H. Flühler, "ELBARA, the ETH L-band radiometer for soil moisture research," *Proc. IEEE IGARSS*, Toulouse, France, 2003, pp. 3058-3060.

[20] *SFB/TR 38–Strukturen und Prozesse der initialen Ökosystementwicklung in einem künstlichen Wassereinzugsgebiet*, BTU Cottbus, Cottbus, Germany, 2006.

[21] W. Gerwin, W. Schaaf, D. Biemelt, A. Fischer, S. Winter, and R. F. Hüttl, "The artificial catchment "Chicken Creek" (Lusatia, Germany) - A landscape laboratory for interdisciplinary studies of initial ecosystem development," *Ecol. Eng.*, vol. 35, no. 12, pp. 1786-1796, 2009.

[22] W. Gerwin, W. Schaaf, D. Biemelt, M. Elmer, T. Maurer, and A. Schneider, "The artificial catchment "Hühnerwasser" (Chicken Creek): Construction and initial properties," in *Ecosystem Development*, vol. I, R. F. Hüttl, W. Schaaf, D. Biemelt, and W. Gerwin, Eds. Cottbus, Germany: BTU Cottbus, 2010. [Online]. Available: http://www.tu-cottbus.de/sfb_trr/ecodev.htm

[23] M. Guglielmetti, M. Schwank, C. Mätzler, C. Oberdörster, J. Vanderborght, and H. Flühler, "Measured microwave radiative transfer properties of a deciduous forest canopy," *Remote Sens. Environ.*, vol. 109, no. 4, pp. 523-532, 2007.

[24] R. A. M. de Jeu, T. Holmes, and M. Owe, "Deriving land surface parameters from 3 different vegetated sites with the ELBARA 1.4-GHz passive microwave radiometer," *Proc. of SPIE*, vol. 5232, pp.434-443, 2004.

[25] H. M. Picket, J. C. Hardy, and F. Jam, "Characterization of a dual-mode horn for submillimeter wavelengths," *IEEE Trans. Microw. Theory Tech.*, vol. MTT-32, no. 8, pp. 936-937, 1984.

[26] T. Pellarin, J.-P. Wigneron, J.-C. Calvet, M. Berger, H. Douville, P. Ferrazzoli, Y. H. Kerr, E. Lopez-Baeza, J. Pulliainen, L. P. Simmonds, and P. Waldteufel, "Two-year global simulation of L-band brightness temperatures over land," *IEEE Trans. Geosci. Remote Sens.*, vol. 41, no. 9, pp. 2135-2139, 2003.

[27] M. Schwank, A. Wiesmann, C. Werner, C. Mätzler, D. Weber, A. Murk, I. Völksch, and U. Wegmüller, "ELBARA II, an L-band radiometer system for soil moisture research," *Sensors*, vol. 10, no. 1, pp. 584-612, 2010.

[28] W. Schaaf, D. Biemelt, and R. F. Hüttl, "Initial development of the artificial catchment "Chicken Creek"–Monitoring program and survey 2005-2008," in *Ecosystem Development*, vol. II, R. F. Hüttl, W. Schaaf, D. Biemelt, and W. Gerwin, Eds. Cottbus, Germany: BTU Cottbus, 2010. [Online]. Available: http://www.tu-cottbus.de/sfb_trr/ecodev.htm

[29] Decagon Devices, Inc. (1 Nov. 2010). ECH2O-TE. [Online]. Available: http://www.decagon.com/products/discontinued-products/ech2o-te/

[30] *RIEGL* Laser Measurement Systems GmbH. (10 Nov. 2010). LMS-Z420i. [Online]. Available: http://www.riegl.com/nc/products/terrestrial-scanning/produktdetail/product/scanner/4/

[31] ESRI. (10 Nov. 2010). ArcGIS. [Online]. Available: http://www.esri.com/software/arcgis/index.html

[32] C. Mätzler, "Chapter 4.3: Relief effects for microwave radiometry," in *Thermal Microwave Radiation–Applications for Remote Sensing*, C. Mätzler, Ed. London, U.K.: IET, 2006, pp. 240-249.

[33] E. Schanda, "Chapter 4.3: Backscattering from Rough Surfaces," in *Physical Fundamentals of Remote Sensing*. Berlin: Springer, 1986, pp. 120-135.

[34] P.-E. Jansson and L. Karlberg, "Coupled heat and mass transfer model for soil-plant-atmosphere systems," Dept. of Civil and Environ. Eng., KTH, Stockholm, Sweden, 2010. [Online]. Available:
http://www.lwr.kth.se/Vara%20Datorprogram/CoupModel/index.htm

[35] L. A. Richards, "Capillary conduction of liquids through porous mediums," *Physics*, vol. 1, pp. 318-333, 1931.

[36] R. H. Brooks and A. T. Corey, "Hydraulic properties of porous media," *Hydrology Paper No. 3*, Colo. State Univ., Fort Collins, 1964.

[37] J. A. Dobrowolski, "Chapter 42: Optical Properties of Films and Coatings," in *Handbook of Optics*, vol. I, M. Bass, E. W. v. Stryland, D. R. Wiliams, and W. L. Wolfe, Eds. New York: McGraw-Hill, 1995, pp. 42.1-42.130.

[38] G. C. Topp, J. L. Davis, and A. P. Annan, "Electromagnetic determination of soil water content: Measurements in coaxial transmission lines," *Water Resour. Res.*, vol. 16, no. 3, pp. 574-582, 1980.

[39] K. Roth, R. Schulin, H. Flühler, and W. Attinger, "Calibration of time domain reflectometry for water content measurement using a composite dielectric approach," *Water Resour. Res.*, vol. 26, no. 10, pp. 2267-2273, 1990.

[40] J. R. Wang and T. Schmugge, "An empirical model for the complex dielectric permittivity of soils as a function of water content," *IEEE Trans. Geosci. Remote Sens.*, vol. GE-18, no. 4, pp. 288-295, 1980.

[41] C. Mätzler and M. Schwank, "Chapter 5.7: Dielectric properties of heterogeneous media," in *Thermal Microwave Radiation–Applications for Remote Sensing*, C. Mätzler, Ed. London, U.K.: IET, 2006, pp. 480-505.

Chapter V

Synthesis

The global water cycle and the potential consequences of climate change on this continuous exchange of water between the land, the oceans, and the atmosphere have increasingly become the focus of environmental research in recent years. Since soil moisture is a key variable in the processes controlling the exchange of water and energy between the land and the atmosphere, this has also led to an increased demand for global soil-moisture data needed as input for numerical weather and climate-prediction models as well as for hydrological models. Remote sensing with passive microwave radiometry at 1.4 GHz has become established as the most promising measuring technique to provide this much needed information at adequate spatial and temporal resolution. However, this measuring approach is an indirect method, which derives soil moisture from the thermal radiance emitted by the moist soil. Consequently, the quality of the retrieved soil-moisture data depends largely on the performance of the radiative-transfer and reflectivity models used in the retrieval algorithms applied to the L-band signatures measured. Although a lot of research has been dedicated towards improving the retrieval algorithms, and the quality of the corresponding soil-moisture data has steadily increased over the years, there is still need for further research. The main objective of this thesis was to contribute toward an improved understanding of the L-band emission of land surfaces, with a special focus on the reflectivity models applied to relate soil reflectivity (or emissivity, respectively) to soil permittivity. In particular, we experimentally investigated the impact of pronounced dielectric anisotropy and (periodic) topographic patterns within a scene on soil reflectivity, and implemented and to some extent developed appropriate reflectivity models, which are able to explain the experimental results.

To this end, three passive microwave experiments were carried out between 2007 and 2009. In the first experiment, the influence of pronounced dielectric anisotropy on thermal emission at 1.4 GHz ($\lambda \approx 21$ cm) was investigated. A wire grid was placed above the ground in the footprint of the L-band radiometer ELBARA, and reflectivities of this grid–ground system were derived from dual-polarized brightness temperatures measured for different grid orientations and wire spacings between 2.5 cm and 20 cm. A physical model taking into account the multiple reflections from the grid and the ground, and using a multiple-beam interference approach to compute the overall reflectivity of the grid–ground system, was developed, and the simulations and the experimental results were compared with each other.

The measurements showed that the grid had almost no influence on the emission for wire spacings $\geq \lambda/2$ $(\approx 10\,\mathrm{cm})$, whereas increasingly anisotropic behavior (birefringence) was observed for smaller wire spacings. For wire spacings near $\lambda/10$ $(\approx 2.5\,\mathrm{cm})$, the observed emission behavior approached that of an ideal wire grid. The reflectivity model developed was able to reproduce such effects satisfactorily for the wire grid with 2.5 cm spacing, but results became increasingly ambiguous at wider wire spacings, which was mainly attributed to uncertainties in the exact grid height above the ground reflection.

The experimental results suggest that also natural emitters displaying striped dielectric anisotropy can affect the L-band brightness of a scene considerably depending on the orientation and periodicity of the corresponding dielectric patterns. When the spatial periodicities are $\leq \lambda/4$, such phenomena should be accounted for in soil-moisture retrieval algorithms. The simulation results, on the other hand, demonstrate also the difficulties involved in using (exact) physical models for these purposes, when critical system parameters are not exactly known or exhibit a certain experimental uncertainty. However, we could clearly show that such striped dielectric patterns can be neglected in soil-moisture retrieval algorithms, when corresponding periodicities are $> \lambda/4$. This is one of the main findings of this study in view of the ongoing SMOS-related research activities in Valencia (Spain). It implies that the many parallel wires present at this SMOS core validation site (due to extensive winegrowing in this area) do not distort the validation measurements.

For the second experiment, we replaced the wire grid with a soil box and imprinted parallel periodic furrows with dimensions close to the observation wavelength into the soil surface. The objective of this study was to investigate the thermal L-band signatures of a soil surface with a periodic topography (furrows), which is typical, e.g. for agricultural fields as a result of plowing, sowing, or furrow irrigation. Dual-polarized brightness temperatures of the artificially-prepared furrowed surfaces were measured under dry- and moist-soil conditions with the furrows either aligned with (longitudinal furrows) or perpendicular (transverse furrows) to the plane of incidence. For comparison, also plane soil surfaces were measured under both soil-moisture conditions. From the brightness temperatures measured, the corresponding reflectivities were derived, and then analyzed with respect to the impact of the periodic topography on the soil reflectivity. To explain the topography-related aspects of the signatures measured, a physical reflectivity model for periodic dielectric surfaces was implemented, and reflectivities were modeled for the different furrow orientations and soil moistures. Modeled values were additionally corrected for the small-scale heterogeneity of the top soil layer using a simple empirical approach.

We found that furrows had a distinct impact on the soil reflectivity at both polarizations and for both furrow directions investigated. At horizontal polarization, furrows of both directions significantly reduced the reflectivity compared to the reflectivity of the plane surface. This decrease was more pronounced for longitudinal than for transverse furrows but independent of soil moisture. At vertical polarization, the reflectivity changes caused by the furrows showed a somewhat more diverse pattern. Longitudinal furrows once again reduced the

reflectivity compared to the plane-surface reflectivity with no clear dependence of the relative reflectivity change on soil moisture. Transverse furrows, however, led to a large increase in the soil reflectivity under dry-soil conditions and to a small increase under moist-soil conditions. The physical reflectivity model for periodic dielectric surfaces was able to reproduce the observed dependence of soil reflectivity on furrow orientation and soil moisture. Using this model, which takes the periodic soil topography into account, improved the agreement between the measured and modeled reflectivities considerably compared to the Fresnel reflectivities. By additionally applying the empirical correction to account for the small-scale heterogeneity of the top soil layer, the quantitative agreement with the modeled reflectivities could be improved further.

The experimental results of this study clearly demonstrate the need for considering the adequate soil topography when retrieving soil moisture from L-band measurements over a furrowed soil surface. With the model simulations performed, we were able to show that this can be achieved by choosing an appropriate reflectivity model. However, most soil-moisture retrieval algorithms used to date parameterize surface roughness with simple fit parameters, and thus consider only small-scale random roughness of a surface. This implies, that soil-moisture retrievals, e.g. from SMOS or airborne radiometer measurements over agricultural areas could be substantially improved by implementing physical reflectivity models accounting for periodic soil topography.

The third experiment performed focused again on topography effects on L-band emission. This time, however, L-band signatures of a soil surface with naturally-formed topographic features were investigated. To this end, ELBARA was installed in a recently renaturated mining area in Northeastern Germany and brightness temperatures of two adjacent footprint areas with similar soils but different relief characteristics were measured quasi-simultaneously. The first footprint observed was crossed by several distinct erosion gullies with steep and differently orientated slopes, whereas the surface of the second footprint was plane. In addition to the brightness temperature measurements, auxiliary hydrometeorological and *in situ* soil parameters were monitored, and digital elevation models of the two footprints were derived from terrestrial laser scanning. The measurements were continued for 1.5 years with the aim to analyze the impact of the different footprint topographies on the brightness temperatures observed, and to investigate how these relief effects vary with time and changing ambient conditions. A complex facet model based on geometric optics, and taking into account the relief of the observed footprints as well as different permittivity (soil moisture) inside and outside the gullies, was developed and brightness temperatures of the two scenes were simulated for the entire observation period based on the hydrometeorological and *in situ* soil measurements. This allowed us to analyze and quantify relief effects on the decimeter to meter scale by directly comparing the brightness temperatures measured and simulated for the plane surface with those of the surface with a distinct relief pattern.

The measurement results demonstrated the distinct impact of such relief patterns on the thermal emission at 1.4 GHz. Brightness temperatures of the surface with the distinct relief

were increased at horizontal polarization and decreased at vertical polarization with respect to the brightness temperatures of the plane surface. By analyzing the brightness temperatures simulated, we could clearly show that these phenomena are mainly due to the variations of the local observation angle and to polarization mixing, both of which are a direct consequence of a distinct relief. Comparing the measured brightness temperatures of both areas with each other revealed that both areas respond differently to changing ambient conditions, which was only partly reproduced in the simulations. This indicates differences in the hydrological behavior of both areas, which are only partially accounted for in the facet model used.

One of the major outcomes of this study is the long time series of measured and simulated brightness temperatures and hydrometeorological data, which clearly demonstrate the distinct impact of the relief (caused by the erosion gullies) on soil emission on the one hand, and indicate different hydrological characteristics of both areas, on the other hand. This comprehensive data set has a great potential for future research and should be further analyzed in more detail than it was possible within the framework of this thesis. In particular, investigating the brightness-temperature changes observed during typical weather conditions at different seasons, such as rain- and snowfall, soil frost and snowmelt, or draught periods, might yield further insight into process-driven brightness-temperature variations. Analyzing these findings further with special regard to the hydrological characteristics of the investigation sites could provide valuable knowledge, which can be utilized to infer information about the hydrological behavior of a soil from L-band signatures measured.

Furthermore, we were able to develop an emission model based on geometric optics, which can be used to compute the L-band emission of land surfaces with a distinct relief and locally varying dielectric properties (permittivities). Using this model improved the agreement between measured and simulated brightness temperatures considerably compared to brightness temperatures modeled without taking into account the footprint relief. This implies that using such a model in an inversion scheme to retrieve soil moisture from brightness-temperature measurements can improve the quality of the retrievals significantly for areas with a distinct relief.

The results of this thesis clearly demonstrate the impact of soil topography and locally varying soil permittivity on the thermal emission at 1.4 GHz of land surfaces, and highlight the need to account for such phenomena when retrieving soil moisture from microwave-radiometer measurements over such areas. Reflectivity and emission models, satisfactorily explaining the experimental results, were presented and their performance was analyzed. This showed, that results can be significantly improved, when appropriate reflectivity/emission models are used in forward models, to compute brightness temperatures from *in situ* soil-moisture data. The final goal, however, is not to model L-band emission, but to infer information about the soil-water content of a soil from the brightness temperatures measured over the corresponding land surface. That means, one of the major challenges for the future will be to implement such models in the inversion schemes used, to retrieve soil moisture from passive microwave radiometer measurements.

Dank

An dieser Stelle möchte ich mich bei allen bedanken, die fachlich zu dieser Arbeit beigetragen haben sowie bei meinen Freunden und meiner Familie, die mich in den letzten Jahren unterstützt und aufgemuntert haben und immer für mich da waren, wenn es nötig war. Ganz speziell möchte ich mich bei folgenden Personen bedanken:

- bei Mike, der mir in den letzten Jahren ein manchmal unorthodoxer, aber (gerade deshalb?) immer super Betreuer war und der im Laufe der Zeit auch mehr und mehr zu einem guten Freund geworden ist. Ich hoffe, dass wir auch in Zukunft sowohl beruflich als auch privat in engem Kontakt bleiben werden.

- bei Christian, dafür dass er sein umfangreiches Wissen mit mir geteilt hat und sich auch die Zeit dafür genommen hat, wenn es nötig war. Vielen Dank auch für das sorgfältige Lesen meiner Manuskripte und die darauf folgenden zwar anstrengenden, aber notwendigen und extrem wertvollen Diskussionen über meine Arbeit!

- bei Manfred, dafür dass er dieses Projekt überhaupt erst „an Land gezogen hat" und dann ein guter und unkomplizierter Chef war - auch als die Arbeit in eine doch ziemlich andere Richtung, als ursprünglich geplant war, abgedriftet ist. Ein großes Dankeschön auch dafür, dass Du mir weiterhin „Asyl an der WSL gewährst".

- bei Fabia, der besten Praktikantin, die ich je hatte. ☺ Danke für Dein großes Interesse und Deinen super Einsatz und viel Erfolg beim Abschließen Deiner Doktorarbeit!

- bei Kari, für seine gute Laune und Unterstützung beim Sand schaufeln und ähnlichen Sachen.

- bei Manu und Grit, für ihre tolle Freundschaft - selbst dann, wenn ich mal wieder recht anstrengend war…

- beim ganzen S16-Team, für gutes Zusammenwohnen, die Ablenkung vom Alltag beim Skifahren, Klettern, Biken etc. und dafür, dass ihr es auch dann noch immer wieder versucht habt, als ich fast immer abgesagt habe. Das holen wir jetzt nach!

- bei meinen Eltern, für alles!

Erklärung

gemäß Art. 28 Abs. 2 RSL 05

Name/Vorname: Völksch/Ingo

Matrikelnummer: 00-925-032

Studiengang: Physik

Bachelor ☐   Master ☐   Dissertation ☒

Titel der Arbeit: Ground-Based Remote Sensing of Land Surfaces - The Influence of Periodic Patterns and Relief on Thermal Microwave Emission

Leiter der Arbeit: Prof. Dr. Christian Mätzler

Zürich, den 22.2.2011

Curriculum Vitae

Personal Details

Name:	Ingo Völksch
Date and place of birth:	22.12.1976, Jena (Germany)
E-mail:	ingo.voelksch@alumni.ethz.ch

Education

2007–2010	Ph.D. student at the Institute of Applied Physics (IAP), University of Bern (Switzerland) and the Swiss Federal Institute of Forest, Snow and Landscape Research (WSL), Birmensdorf (Switzerland)
2001–2004	Diploma in Earth Sciences at the Swiss Federal Institute of Technology (ETH), Zürich (Switzerland)
1997–2001	Pre-Degree (Vordiplom) in Geology at the Friedrich-Schiller-Universität (FSU), Jena (Germany)
1994–1996	Abitur with emphasis on Natural Sciences at Carl-Zeiss-Gymnasium (secondary school), Jena (Germany)
1993–1994	High School Diploma at Mt. Vernon High School, Mt. Vernon (USA)